1991-02

Vector Associative Maps: Unsupervised Real-time Error-based Learning and Control of Movement Trajectories

https://hdl.handle.net/2144/2057

VECTOR ASSOCIATIVE MAPS: UNSUPERVISED REAL-TIME ERROR-BASED LEARNING AND CONTROL OF MOVEMENT TRAJECTORIES

Paolo Gaudiano and Stephen Grossberg

February, 1991

Technical Report CAS/CNS–TR–91–002

Boston University Center for Adaptive Systems and
Department of Cognitive and Neural Systems
111 Cummington Street
Boston, MA 02215

VECTOR ASSOCIATIVE MAPS: UNSUPERVISED REAL-TIME ERROR-BASED LEARNING AND CONTROL OF MOVEMENT TRAJECTORIES

Paolo Gaudiano* and Stephen Grossberg†
Center for Adaptive Systems
and
Graduate Program in Cognitive and Neural Systems
Boston University
111 Cummington Street
Boston, MA 02215

November 1989

Requests for reprints should be sent to:
Stephen Grossberg
Center for Adaptive Systems
Boston University
111 Cummington Street
Boston, MA 02215

---

*Supported in part by the National Science Foundation (NSF IRI-87-16960).

†Supported in part by the Air Force Office of Scientific Research (AFOSR 90-0175), DARPA (AFOSR 90-0083), and the National Science Foundation (NSF IRI-87-6960).

Acknowledgements: The authors wish to thank Carol Yanakakis Jefferson for her valuable assistance in the preparation of the manuscript.

Table of Contents

Abstract

This article describes neural network models for adaptive control of arm movement trajectories during visually guided reaching and, more generally, a framework for unsupervised real-time error-based learning. The models clarify how a child, or untrained robot, can learn to reach for objects that it sees. Piaget has provided basic insights with his concept of a *circular reaction*: As an infant makes internally generated movements of its hand, the eyes automatically follow this motion. A transformation is learned between the visual representation of hand position and the motor representation of hand position. Learning of this transformation eventually enables the child to accurately reach for visually detected targets. Grossberg and Kuperstein have shown how the eye movement system can use visual error signals to correct movement parameters via cerebellar learning. Here it is shown how endogenously generated arm movements lead to adaptive tuning of arm control parameters. These movements also activate the target position representations that are used to learn the visuo-motor transformation that controls visually guided reaching. The AVITE model presented here is an adaptive neural circuit based on the Vector Integration to Endpoint (VITE) model for arm and speech trajectory generation of Bullock and Grossberg. In the VITE model, a Target Position Command (TPC) represents the location of the desired target. The Present Position Command (PPC) encodes the present hand-arm configuration. The Difference Vector (DV) population continuously computes the difference between the PPC and the TPC. A speed-controlling GO signal multiplies DV output. The PPC integrates the (DV)·(GO) product and generates an outflow command to the arm. Integration at the PPC continues at a rate dependent on GO signal size until the DV reaches zero, at which time the PPC equals the TPC. The AVITE model explains how self-consistent TPC and PPC coordinates are autonomously generated and learned. Learning of AVITE parameters is regulated by activation of a self-regulating Endogenous Random Generator (ERG) of training vectors. Each vector is integrated at the PPC, giving rise to a movement command. The generation of each vector induces a complementary postural phase during which ERG output stops and learning occurs. Then a new vector is generated and the cycle is repeated. This cyclic, biphasic behavior is controlled by a specialized gated dipole circuit. ERG output autonomously stops in such a way that, across trials, a broad sample of workspace target positions is generated. When the ERG shuts off, a modulator gate opens, copying the PPC into the TPC. Learning of a transformation from TPC to PPC occurs using the DV as an error signal that is zeroed due to learning. This learning scheme is called a Vector Associative Map, or VAM. The VAM model is a general-purpose device for autonomous real-time error-based learning and performance of associative maps. The DV stage serves the dual function of reading out new TPCs during performance and reading in new adaptive weights during learning, without a disruption of real-time operation. VAMs thus provide an on-line unsupervised alternative to the off-line properties of supervised error-correction learning algorithms. VAMs and VAM cascades for learning motor-to-motor and spatial-to-motor

maps are described. VAM models and Adaptive Resonance Theory (ART) models exhibit complementary matching, learning, and performance properties that together provide a foundation for designing a total sensory-cognitive and cognitive-motor autonomous system.

1 Self-Organization of Intermodal and Intramodal Maps for Visually Guided Reaching

This article describes self-organizing neural circuits for the control of planned arm movements during visually guided reaching that were first reported in Gaudiano and Grossberg (1990a, 1990b) and Grossberg (1990a). More generally, it introduces a modelling framework for unsupervised, real-time, error-based learning. The problem that motivates our results concerns the issue of how a child learns to reach for objects that it sees. This problem requires an understanding of the interactions between two distinct modalities: vision (seeing an object) and motor control (moving a limb). In particular, we need to characterize the self-regulating mechanisms whereby an individual can stably learn transformations within and between the different modalities that provide accurate control of goal-oriented movements.

The Swiss psychologist Jean Piaget (1963) has suggested that learning of this type can take place through a *circular reaction.* As a child performs random, spontaneously generated movements of his arm, its eyes follow the arm's motion, thereby enabling learning of a transformation from a visual representation of arm position to a motor representation of the same arm position. As more and more arm positions are sampled through time, the transformation eventually enables the child to reach for objects that it sees.

A similar kind of circular reaction is found in the "babbling phase" of speech acquisition in infants (Fry, 1966). Here interactions take place between the speech perception (hearing) and production (speaking) systems. When the child babbles a sound, an auditory feedback representation of the sound is activated and coexists with the motor representation that gave rise to the sound. As the child learns a transformation from the auditory representation to the motor representation, it can begin to imitate heard sounds that are produced by other speakers.

The above examples introduce the circular reaction as an autonomously controlled behavioral cycle with two components: *production* and *perception*. Learning links the two modalities to enable sensory-guided action to occur. Such a circular reaction is *intermodal*; that is, it consists of the coupling of two systems operating in different modalities.

In order for the intermodal circular reaction to generate stable learning of the parameters that couple the two systems, the control parameters within each system must already be capable of accurate performance. Otherwise, performance may not be consistent across trials and a stable mapping could not be learned between different modalities. Thus it is necessary to self-organize the correct *intramodal* control parameters before a stable *intermodal* mapping can be learned.

Grossberg and Kuperstein (1986, 1989) have modelled how such control parameters can be learned within the eye movement system. During early development, eye movements are made reactively in response to visual inputs. When these eye movements do not lead to foveation of the visual target, the nonfoveated position of the target generates a visual error signal. Their model suggests how such error signals can be used by the cerebellum to learn eye movement control parameters that lead to accurate foveations.

Here we show how the arm movement system can endogenously generate movements during a "motor babbling" phase. These movements create the data needed to learn correct arm movement control parameters. These movements also activate the target position representations that are used to learn the visuo-motor transformation that controls visually guided reaching.

Our results are developed within a model that we call the AVITE model (Figure 1) for variable-speed adaptive control of multi-joint limb trajectories.

Figure 1

2 Trajectory Formation as an Emergent Invariant

Many models for sensory-motor control of arm movement trajectories attempt to learn, or otherwise pre-plan, the entire trajectory for each possible movement. However, the number of trajectories that can be followed even in the act of reaching for a single target in space shows that such a strategy rapidly leads to a combinatorial explosion. Furthermore, this type of model cannot easily account for the ability to rapidly adjust to target position changes or other mid-trajectory corrections, as well as many other known properties of arm movements.

Bullock and Grossberg (1988a) have suggested instead how motor synergies can be dynamically bound and unbound in real-time. Once bound, the multiple muscles within a synergy can move a limb at variable speeds by synchronously contracting variable amounts in equal time. In this view, trajectory formation is an emergent invariant that arises through interactions among two broad types of control mechanisms: planned control and automatic control. Planned control variables include (1) target position, or where we want to move; and (2) speed of movement, or how fast we want to move to the desired position, and the "will" to move at all. Automatic control variables compensate for (3) the present position of the arm; (4) unexpected inertial forces and external loads; and (5) changes in the physiognomy of the motor plant, due for example to growth, injury, exercise, and aging.

The Vector Integration to Endpoint (VITE) model of Bullock and Grossberg implements such a strategy of trajectory control and has been used to explain a large behavioral and neurobiological data base (see Bullock and Grossberg, 1988a, 1988b, 1989, 1990). A prime example of an emergent invariant that is explained by the VITE model is the synchrony with which multiple joints can be moved at variable speeds.

3 The VITE Model

Figure 2 summarizes the main components of the VITE circuit. At the top of the figure, inputs to the Target Position Command (TPC) populations represent the desired final position of the arm. At the bottom of the figure, the Present Position Command (PPC) populations code an internal representation of where the arm presently is. Outflow movement commands to the arm are generated by the PPC. These outflow signals, supplemented by spinal circuitry and cerebellar learning (Bullock and Grossberg, 1989, 1990) move the hand to the location coded by the PPC relative to the body, while compensating for dynamic effects and loading conditions.

Figure 2

The Difference Vector (DV) populations continuously compute the discrepancy between present position signals (PPC) and the desired target position commands (TPC). Output signals from the DV are integrated by the PPC until the latter becomes equal to the TPC, at which time the DV equals zero and PPC integration stops. Hence the VITE circuit embodies an automatic process that moves the PPC continuously to the TPC. The Adaptive VITE (AVITE) model presented herein explains how generation of correct TPC representations is learned through "motor babbling": Endogenously-generated random PPC movement commands move the arm through a full range of positions and activate TPCs whose signals to the DV are adaptively tuned using the DV itself as source of error signals.

4 Coding Movement Speed and Intentionality: The GO Signal

If the PPC were always allowed to integrate the DV, then a movement would begin as soon as the TPC becomes active. Somehow it must be possible to "prime" a target position without moving the arm until another signal indicates the intent to carry out the movement. A related issue concerns how the overall speed of a movement can be varied without changing the desired TPC. "Priming" denotes the limiting case of zero speed.

Trajectory-preserving speed control can be achieved by multiplying the output of the DV with a nonspecific gating signal. This is the GO signal depicted in Figure 2. Because of its location within the VITE model, the GO signal affects the rate at which the PPC is continuously moved toward the TPC. For example, as long as the GO signal is zero, instatement of a TPC generates a non-zero DV, but the PPC remains unaltered. This "primed" DV codes the difference between the arm's present position and desired position. If the arm is passively moved through space by external forces while the GO signal is zero, the PPC is updated through sensory feedback from the muscles via a Passive Update of Position, or PUP, circuit (Figure 3). The DV also changes to reflect the change in arm position, so that onset of the GO signal during a subsequent voluntary movement will still result in formation of a correct trajectory.

When the GO signal is nonzero, any activation in the DV is integrated by the PPC at a rate proportional to the product (DV)·(GO). Integration ceases when the PPC equals the TPC and the DV equals zero, even if the GO signal remains positive. Other things being equal, a larger GO signal causes the PPC to integrate at a faster rate, so the same target is reached in a shorter time.

Figure 3

Bullock and Grossberg (1988a, 1990) and Grossberg and Kuperstein (1989) have summarized experimental evidence suggesting that the TPC is computed in parietal cortex, the DV in motor cortex, and the GO signal in globus pallidus. The VITE model then predicts that the motor cortex and globus pallidus give rise to output pathways that converge upon a processing stage where DV and GO signals are multiplied to compute a measure of movement speed and direction. This processing stage, in turn, is predicted to generate excitatory inputs to a neural (leaky) integrator which computes PPC outflow command signals.

5 Autonomous Learning of AVITE Coordinates

In order for the AVITE model to generate correct arm trajectories, the TPC and PPC must be able to activate dimensionally consistent signals TPC→DV and PPC→DV for comparison at the DV. There is no reason to assume that the gains, or even the coordinates, of these signals are initially correctly matched. Learning of an adaptive coordinate transformation is needed to achieve self-consistent matching of TPC- and PPC-generated signals at the DV.

In order to learn such a transformation, TPCs and PPCs that represent the same target positions must be simultaneously activated. This cannot be accomplished by activating a TPC and then letting the AVITE circuit integrate the corresponding PPC. Such a scheme would beg the problem being posed; namely, to discover how TPC→DV and PPC→DV signals are calibrated so that a TPC *can* generate the corresponding PPC. An analysis of all the possibilities that are consistent with VITE constraints suggests that PPCs are generated by internal, or endogenous, activation sources during a motor babbling phase. After such a babbled PPC is generated and a corresponding action taken, the PPC itself is used to activate a TPC representation which *a fortiori* represents the same target position (Figure 4). Thus motor babbling samples the work space and, in so doing, generates a representative set of pairs (TPC, PPC) for learning the AVITE coordinate transformation.

6 Associative Learning from Parietal Cortex to Motor Cortex During the Motor Babbling Phase

Further analysis suggests that the only site where an adaptive coordinate change can take place is at the synaptic junctions that connect the TPC to the DV. These junctions are represented as semi-circular synapses in Figure 1. Moreover, DV activation can be used as an internal measure of error, in the sense that miscalibrated signals TPC→DV and PPC→DV from TPCs and PPCs corresponding to the same target position will generate a nonzero DV. Learning is designed to change the synaptic weights in the pathways TPC→DV in a way that drives the DV to zero. After learning is complete, the DV can only equal zero if the TPC and PPC represent the same target position. If we accept the neural interpretation of the TPC as being computed in the parietal cortex (Anderson, Essick, and Siegel, 1985; Grossberg and Kuperstein, 1986, 1989) and the PPC as being computed in the precentral motor cortex (Bullock and Grossberg, 1988a; Georgopoulos, *et al.*, 1982, 1984, 1986), then we are led to predict that associative larning during the motor babbling stage takes place on a pathway, possibly multisynaptic (as in Figure 4b), connecting parietal cortex to motor cortex. Specifically, activation of the difference vector cells in motor cortex is predicted to be driven towards zero (or to a tonic resting level) by learning during postural intervals.

7 Vector Associative Map: On-Line DV-Mediated Learning and Performance

When such a learning law is embedded within a complete AVITE circuit, the DV can be used for on-line regulation of both learning and performance. During a performance phase, a new TPC is read into the AVITE circuit from elsewhere in the network, such as when a reaching movement is initiated by the visual representation of a target. The new DV is used to integrate a PPC that represents the same target position as the TPC.

Zeroing the DV here creates a new PPC while the TPC is held constant. In contrast, during the learning phase, the DV is used to drive a coordinate change in the TPC→DV synapses. Zeroing the DV here creates new adaptive weights while both the PPC and TPC are held fixed.

Both the learning and the performance phases use the same AVITE circuitry, notably the same DV, for their respective functions. Thus learning and performance can be carried out on-line in a real-time setting, unlike most traditional off-line supervised error correction schemes. The operation whereby an endogenously generated PPC activates a corresponding TPC, as in Figure 4b, "back propagates" information for use in learning, but does so using local operations without the intervention of an external teacher or a break in on-line processing.

We call the class of models that use this on-line learning and performance scheme a Vector Associative Map (VAM) because it uses a difference vector to both learn and perform an associative mapping between internal representations.

Autonomous control, or gating, of the learning and performance phases is needed to achieve effective on-line dynamics, at least when learning is fast. For example, the network needs to distinguish whether DV≠0 because the TPC and PPC represent different target positions, or because the TPC→DV synapses are improperly calibrated. In the former case, learning should not occur; in the latter case, it should occur. Thus some type of learning gate may be needed to prevent spurious associations from forming between TPCs and PPCs that represent different target positions. The design of the total AVITE network shows how such distinctions are computed and used for real-time control of the learning and performance phases. We now explain how this is accomplished. Section 21 gives an analysis of the required gating signals.

8 The Motor Babbling Cycle

During the motor babbling stage, an Endogenous Random Generator (ERG) of training vectors is activated. These vectors are input to the PPC stage, which integrates them, thereby giving rise to outflow signals that move the arm through the workspace (Figure 4a). After each interval of ERG activation and PPC integration, the ERG *automatically* shuts off, so that the arm stops at a random target position in space.

Figure 4

Offset of the ERG opens a Now Print (NP) gate that copies the PPC into the TPC through some fixed, arbitrary transformation (Figure 4b). The top-down adaptive filter from TPC to DV learns the correct reverse transformation by driving the DV toward zero while the NP gate is open (Figure 4c-d). Then the cycle is automatically repeated. When the ERG becomes active again, it shuts off the NP gate and thus inhibits learning. A new PPC command is integrated and another arm movement is elicited.

The ERG is designed so that, across the set of all movement trials, its output vectors generate a set of PPCs that form an unbiased sample of the workspace. This sample of PPCs generates the set of (TPC, PPC) pairs that is used to learn the adaptive coordinate change TPC→DV via the VAM.

9 Opponent Interactions in the VITE Model

Opponent processing permeates the neural functions of all species. This design principle expresses itself in sensory-motor control through the organization of muscles into agonist-antagonist pairs that work together to control flexion and extension of joints. Similarly, agonist-antagonist muscle pairs are controlled by neural networks that are themselves coupled in an opponent fashion (e.g., Ryall, 1970; Kandel and Schwartz, 1985, Chapters 25, 35; Bullock and Grossberg, 1989, 1990).

Opponent processing is needed to realize many AVITE model properties. The primary need for opponency arises from the fact that each PPC component integrates the net positive, or excitatory, output of the corresponding DV component. Once the PPC has grown to a positive value, it cannot decrease without receiving some form of inhibition. In the Bullock and Grossberg (1988a) VITE model, two controlling channels for each agonist-antagonist muscle pair are coupled in a push-pull fashion at the appropriate processing stages.

Figure 5

Figure 5 illustrates the AVITE circuit with agonist and antagonist channels coupled in an opponent fashion. These push-pull interactions allow, for example, reduction of the antagonist PPC as the agonist PPC is increased. Throughout the remainder of the paper, we will sometimes use diagrams such as the one shown in Figure 1 for simplicity, even though each module is intended to control a muscle pair.

10 The Endogenous Random Generator of Workspace Sampling Bursts

The ERG design embodies another example of the need for opponent interactions. The motor babbling cycle is controlled by two complementary phases in the ERG mechanism: an *active* and a *quiet* phase. The active phase generates random vectors to the PPC. During the quiet phase, input to the PPC from the ERG is zero, thereby providing the opportunity to learn a stable (TPC, PPC) relationship. In addition, there must be a way for the ERG to signal onset of the quiet phase, so that the NP gate can open and copy the PPC into the TPC. The NP gate must not be open at other times: If it were always open, any incoming commands to the TPC could be distorted by contradictory inputs from the PPC. Therefore, offset of the active ERG phase must be accompanied by onset of a complementary mechanism whose output energizes opening of the NP gate.

The signal that opens the NP gate can also be used to modulate learning in the adaptive filter. In general, no learning should occur except when the PPC and TPC encode the same position. See Section 21 for details

Figure 6

Figure 6 provides a schematic diagram of the ERG circuit. The design is a specialized gated dipole (Grossberg, 1972a, 1982, 1984). A gated dipole is a neural network model for the type of opponent processing during which a sudden input offset within one channel can trigger activation, or antagonistic rebound, within the opponent channel. Habituating transmitter gates in each opponent channel regulate the rebound property by modulating the signal in their respective channel. In applications to biological rhythms, each channel's offset can trigger an antagonistic rebound in the other channel, leading to a rhythmic temporal succession of rebound events. An example of such an endogenously active rhythm generator was developed by Carpenter and Grossberg (1983, 1984, 1985; reprinted in Grossberg, 1987a) to explain parametric data about control of circadian rhythms by the suprachiasmatic nuclei of the hypothalamus.

In the present application, note the complementary time intervals during which the ON and OFF channels of the ERG are active: The ON channel output must be different during each active phase so that integrated PPCs result in random movements that sample the workspace. In contrast, OFF channel activation must be fairly uniform across trials, thereby providing intervals during which learning can stably occur.

Figure 7 illustrates the main characteristic of the simplest type of feedforward gated dipole: When a phasic input J^+ is applied to the ON channel, the corresponding ON channel output O^+ exhibits a transient overshoot that decays, or habituates, to a new, lower resting level. Offset of the phasic input causes the ON output to quickly drop to zero, while the OFF channel output O^- exhibits a transient antagonistic rebound followed by a decay to zero. Hence the gated dipole embodies a mechanism for generating a transient antagonistic rebound to offset of a phasic cue.

Figure 7

The OFF rebound is due to opponent interactions between two channels whose signals are multiplicatively gated by chemical transmitters. The chemical gates (rectangular synapses in Figures 6 and 7) are presumed to act on a time scale slower than the time scale of neuronal activation, so that sudden shifts in input are followed by slower changes in the amount of available transmitter substance.

The basic gated dipole circuit needs to be specialized to design an effective ERG circuit. Such an ERG circuit needs to convert a continuous stream of random inputs to the ON channel (J^+ in Figure 6) into cyclic output bursts from the ON channel, interspersed with OFF intervals whose duration is relatively stable across trials.

In order to convert a stream of random inputs into a series of output bursts, activation of the ON channel must initiate a process that spontaneously terminates ON channel output even while the random inputs remain on. This can be achieved if the net signal through the transmitter gate is an inverted-U function of input size. Then the gated ON output can "crash" on the time scale of transmitter habituation. The usual transmitter law of a gated dipole needs to be modified to achieve this property, because the net signal through the transmitter gate in the simplest gated dipole is an increasing function, not an inverted-U function, of input size.

In order to achieve cyclic output bursts from the ON channel, the ON chemical transmitter gate must be allowed to recover from habituation after crashing. To this end, the random input stream to the ON channel must be blocked after the ON gate crashes. Our solution is to let OFF channel activation (which becomes positive when the ON channel crashes) shut off the source of phasic input J^+, which will cause a transient increase of activity in the OFF channel while the ON transmitter gate recovers from habituation. This process is represented in Figure 6 as a feedback pathway from the

OFF channel of the ERG to the input source (J^+) through a Pauser Gate (PG) whose output is constant above its firing threshold.

Figure 8 illustrates the dynamics of the ERG as it goes through one complete cycle. The Appendix provides a mathematical analysis of the ERG transmitter gate dynamics.

Figure 8

11 Some Results: Correct Parameter Learning and Trajectory Formation Through Motor Babbling

This section provides a qualitative overview of the major results obtained through simulation of the ERG-AVITE system during the babbling phase of adaptive tuning. More detailed simulation results will be given in later sections.

Figure 9 is a schematic diagram of the complete system used in the simulations described below to control a two-jointed arm. Each AVITE module consists of one agonist channel and one antagonist channel, coupled in a push-pull fashion. Each channel receives inputs from its own ERG circuit. As shown in Figure 9, all ERG OFF channels cooperate to activate a single PG, and output from all DV channels is gated by a single GO signal, to insure synchronous learning and performance for all muscle pairs.

Figure 9

Figure 10 shows the graphical output of the simulation program during babbling. Each grid shows a different configuration of the two-joint arm, with each joint regulated by one AVITE module. The figure illustrates some of the positions attained during the quiet phases of motor babbling. A more quantitative demonstration of the relatively uniform distribution of endogenously-generated arm positions is given in Figures 11-18 (Section 14).

Figure 10

Figure 19 (Section 15) illustrates the convergence of the learning process as motor babbling progresses. The plot shows the DV at the onset of successive quiet phases, when the PPC equals the TPC. Learning successfully drives the DV to zero at an approximately exponential rate.

Figure 20 (Section 15) shows the graphical display during simulation of movement performance at various stages of AVITE training. Each grid shows the terminal position reached by the two-joint arm after a target joint configuration has been instated (shown as a black triangle on each grid) and the GO signal has been turned on. Performance was tested at increasing levels of AVITE training, resulting in increasingly accurate reaching behavior.

We now turn to the mathematical description of the AVITE and ERG models. Simulation results will be more precisely described in Sections 14-23, to which the reader may directly turn on a first reading.

12 AVITE Equations

Figures 5 and 6, respectively, show the AVITE and ERG models with all system variables labelled at their acting locus. In the AVITE equations, the subscript i refers to the ith module in the simulation. Each module consists of an agonist-antagonist pair of channels, and a single module controls a single joint. Unless otherwise indicated, each equation below describes the behavior of variables for the agonist channel, labelled by the $(+)$ superscript in Figures 5 and 6. The corresponding equations for the antagonist variables in the same module—omitted for clarity—can be obtained by exchanging every $(+)$ superscript with a $(-)$ superscript, and vice versa. With few exceptions, uppercase roman letters are used to symbolize independent variables; lower case roman letters symbolize functions or indices; and greek letters symbolize parameters that remain fixed over the course of a simulation.

Each AVITE module requires the input of *two* ERG ON channels coupled in a push-pull fashion to insure that contraction of the agonist muscle is accompanied by relaxation of the antagonist. Because ON and OFF channel variables for each ERG circuit are also distinguished with (+) and (−) superscripts, we will use the following notation: Variable O_{2i-1}^{+} indicates the output of an ERG ON channel to the ith *agonist* PPC, whose activity is denoted by P_i^+. Variable O_{2i}^{+} indicates the output of a different ERG ON channel to the ith *antagonist* PPC, whose activity is denoted by P_i^- (see bottom of Figure 5).

Present Position Command

Let PPC variable P_i^+ obey the equation

$$\frac{dP_i^+}{dt} = (1 - P_i^+)\left(G\left[V_i^+\right]^R + O_{2i-1}^{+}\right) - P_i^+\left(G\left[V_i^-\right]^R + O_{2i}^{+}\right), \qquad (1)$$

where $[w]^R = \max(w, 0)$ represents rectification. This is the rate-determining equation for the entire system: We assume an integration rate of 1 and adjust the time constant of all other equations relative to this one.

In equation (1), the PPC acts to integrate its inputs via a shunting on-center off-surround network. Adding a small leaky integrator term $-\epsilon P_i^+$ to the right hand side of (1) does not qualitatively change the results. Terms $G\left[V_i^+\right]^R$ and $G\left[V_i^-\right]^R$ are agonist and antagonist components, respectively, gated by the nonspecific GO signal G. Terms O_{2i-1}^{+} and O_{2i}^{+} are ERG ON channel outputs, respectively, to the agonist and antagonist PPC. Excitatory inputs coming from the agonist DV and ERG channels (V_i^+, O_{2i-1}^{+}) are counteracted by inputs from the antagonist DV and ERG channels (V_i^-, O_{2i}^{+}). This creates a push-pull mechanism that insures proper antisymmetrical activation in the agonist and antagonist muscles.

The multiplicative factors $(1 - P_i^+)$ and P_i^+ in the excitatory and inhibitory terms of (1) are shunting terms (Grossberg, 1973, 1982) that interact with the opponent inputs to normalize the PPC activations within the range $[0, 1]$, and to make P_i^+ compute the ratio of opponent inputs. To see this, solve equation (1) at equilibrium ($\frac{dP}{dt} = 0$). Then

$$P_i^+ = \frac{\left(G\left[V_i^+\right]^R + O_{2i-1}^+\right)}{\left(G\left[V_i^+\right]^R + O_{2i-1}^+\right) + \left(G\left[V_i^-\right]^R + O_{2i}^+\right)}. \tag{2}$$

Activation in the antagonist channel appears in the denominator, thus reducing agonist activation, and vice versa. Furthermore, activation in either channel is bounded in the interval $[0, 1]$, and total activation is normalized to 1; that is, $P_i^+ + P_i^- = 1$.

Difference Vector

The DV variable V_i^+ obeys the additive equation

$$\frac{dV_i^+}{dt} = \alpha\left(-V_i^+ + T_i^+ Z_i^+ - P_i^+\right) \tag{3}$$

The DV tracks the difference between a filtered copy of the TPC, namely $T_i^+ Z_i^+$, and the PPC variable P_i^+ at rate α.

Adaptive Filter LTM Traces

The LTM trace, or adaptive weight, Z_i^+ from the TPC component T_i^+ to the DV component V_i^+ obeys the learning equation

$$\frac{dZ_i^+}{dt} = g_n f(T_i^+)(-\beta Z_i^+ - \gamma V_i^+), \tag{4}$$

where

$$f(T_i) = \begin{cases} 1 & \text{if } T_i > 0 \\ 0 & \text{if } T_i = 0. \end{cases} \tag{5}$$

Equations (4) and (5) define a *gated vector learning law* whereby changes in adaptive weights are driven by deviations of the DV from zero when the learning gate g_n is opened and the presynaptic node T_i is active. Other types of $f(T_i)$ would work as long as learning is prevented when $T_i = 0$.

As the correct scaling factors from PPC to TPC channels are learned, the DV values converge to zero. Term g_n in (4) represents the Now Print Gate. As described in Section 8, the Now Print gate enables the PPC to activate a TPC that represents the same target position of the arm. This gate can be coupled to the Pauser Gate g_p of equation (18), or to activation of the GO signal. See Section 21 for details.

Target Position Command

The TPC variable T_i^+ obeys the equation

$$\frac{dT_i^+}{dt} = \delta\left[-\epsilon T_i^+ + (1 - T_i^+)(E_i^+ + F_i^+ + T_i^+) - T_i^+(E_i^- + F_i^- + T_i^-)\right]. \tag{6}$$

Equation (6) is a shunting competitive equation that normalizes TPC activities for dimensionally consistent matching against PPC activities at the DV; see equation (1). A small leaky integrator term $-\epsilon T_i^+$ was also included to illustrate that either a leaky integrator or a perfect integrator, as in (1), can be used. The input terms to each TPC are of three types:

(i) Intermodal Target Commands: These are feedforward external inputs (E_i^+, E_i^-) that instate new TPCs from other modalities, say from visual inspection of a moving target;

(ii) PPC-to-TPC Conversions: These are feedback inputs (F_i^+, F_i^-) from the PPC to the TPC. These inputs instate the TPC corresponding to the PPC attained during an active phase of ERG input integration. Terms F_i^+ and F_i^- turn on when the Now Print gate g_n turns on; that is,

$$F_i^+ = l(P_i^+, g_n) \tag{7}$$

and

$$F_i^- = l(P_i^-, g_n), \tag{8}$$

where function l represents a fixed mapping (see Sections 15 and later).

(iii) Short-Term Memory Storage: These are feedback signals (T_i^+, T_i^-) from TPCs to themselves such that each agonist excites itself and inhibits its antagonist via a linear function of its activity. Such on-center off-surround linear shunting feedback signals store the normalized TPCs in short-term memory until they are updated by new intermodal inputs or PPC feedback (Grossberg, 1973, 1982). The ratio scale established by these shunting terms also allows PPC feedback to occur after the PPC integrates the TPC, without changing the TPC. In other words, if F_i^+ and F_i^- turn on with values $F_i^+ = \theta T_i^+$ and $F_i^- = \theta T_i^-$, for some scaling parameter $\theta > 0$, then T_i^+ and T_i^- are essentially unchanged. Similarly, instatement of an intermodal target command ($E_i^+ = \theta T_i^+, E_i^- = \theta T_i^-$) will not change the TPC activation. Any changes that do occur are due to the finite integration rate and the small passive decay term, but will typically be small and transient in nature.

13 ERG Equations

Tonic Input to the ERG

Let the tonic inputs I_k^+ and I_k^- to the k^{th} ERG ON channel and ERG OFF channel obey the equations

$$I_k^+ = I_k^- = I \text{ (constant)}. \tag{9}$$

The tonic input I provides a constant baseline of activation in both ERG channels (Figure 6). This provides the energy for the transient rebound in the k^{th} OFF channel after the random input J_k^+ to the k^{th} ON channel is gated off by the Pauser Gate g_p. Without tonic input, OFF channel activation could never exceed zero.

Random Input to the ERG

Let input J_k^+ to the k^{th} ON channel of the ERG obey the equation

$$J_k^+ = \begin{cases} \max\left(0, J \in [\mu_J - \frac{\sigma_J}{2}, \mu_J + \frac{\sigma_J}{2}]\right) & \text{with probability } 1/\pi_J \\ \mu_J & \text{with probability } (1 - 1/\pi_J) \end{cases} \tag{10}$$

Random noise values J_k^+ are chosen from an interval of size σ_J centered around the average level μ_J. The term π_J represent the average time that elapses between activation "spikes." Equation (10) represents one type of internal noise; namely, randomly distributed activation within a fixed interval. Other types of noise have also been shown to work. See Section 14 for details. The OFF channels receive no random input ($J_k^- \equiv 0$).

ON and OFF Channel Input Layer Activations

The k^{th} ERG ON channel input layer activity X_k^+ obeys the equation

$$\frac{dX_k^+}{dt} = -\zeta X_k^+ + (\eta - X_k^+)[I + J_k^+(1 - g_p)]. \tag{11}$$

This equation describes leaky-integrator shunting dynamics. The X_k^+ populations receive a tonic input I and a random input J_k^+. The input J_k^+ is gated shut by term $(1-g_p)$ when the Pauser Gate g_p turns on, since g_p switches from 0 to 1 at that time (Equation (18)). The relative values of the leakage rate ζ and saturation limit η compared to the magnitude of the inputs determine how sensitive the cell will be to fluctuations in the input noise. Section 14 provides details.

Habituating Transmitter Gates

Let the transmitter gate Y_k^+ in the k^{th} ON channel obey the equation

$$\frac{dY_k^+}{dt} = \kappa(\lambda - Y_k^+) - h(X_k^+)Y_k^+. \tag{12}$$

In (12), transmitter Y_k^+ accumulates to a maximal level λ at the constant rate κ and is inactivated, or habituates, at the activity-dependent rate $h(X_k^+)$, where

$$h(X) = \nu X^2 + \xi X. \tag{13}$$

The net ON channel signal through the gate is

$$X_k^+ Y_k^+, \tag{14}$$

which is proportional to the rate of transmitter release. When solved at equilibrium, the system (12), (13) and (14) give rise to an inverted-U function of X_k^+; namely,

$$X_k^+ Y_k^+ = \frac{\kappa\lambda X_k^+}{\kappa + \nu(X_k^+)^2 + \xi X_k^+}. \tag{15}$$

Opponent Output Signals

The net output O_k^+ of the k^{th} ERG ON channel, after opponent processing, obeys the equation

$$O_k^+ = \left[X_k^+ Y_k^+ - X_k^- Y_k^-\right]^R. \tag{16}$$

The outputs O_k^+ are the inputs to the PPC populations of the AVITE model, as in equation (1). The ERG OFF outputs O_k^- obey the analogous equation

$$O_k^- = \left[X_k^- Y_k^- - X_k^+ Y_k^+\right]^R. \tag{17}$$

These signals activate the Pauser Gate in the manner described below.

Pauser Gate

The Pauser Gate g_p obeys the equation

$$g_p = \begin{cases} 1 & \text{if } \sum_k O_k^- > \theta_P \\ 0 & \text{otherwise} \end{cases} \tag{18}$$

where θ_P is a fixed threshold. When multiple ERG modules are simulated, all of the OFF channel outputs O_k^- are summed at the Pauser Gate via term $\sum_k O_k^-$ in (18). This insures that all AVITE modules are in their quiet phase at the same time, and that learning is synchronous across all movement-controlling joints.

14 ERG Simulations

In the system represented by equations (9)-(18), it is possible to modify the spatial, temporal, and statistical characteristics of the ERG ON outputs O_k^+ in a number of ways. In our case, we wanted to design a mechanism capable of generating a uniform distribution of random vectors that could be integrated by the PPC to generate a full sample of arm movements during AVITE training.

All simulation results reported in this article were generated on Sun and Silicon Graphics workstations. The code was written in C, using double-precision floating point accuracy. We used a fourth-order Runge-Kutta ODE solver for numerical integration. Step size was fixed at $h = 0.2$, and was varied occasionally to insure accuracy of the numerical integration. We also ran a standard simulation with the LSODA integration package of the Livermore Laboratories (Petzold, 1983; Hindmarsh, 1983) to confirm accuracy. The LSODA package uses adaptive step size and can automatically switch between stiff and non-stiff methods. The discontinuous nature of the input actually made the simple Runge-Kutta integrator significantly faster.

In this section we show results based on simulations of a two-joint AVITE model (Figure 9). All simulations are based on the standard parameters given in Figure 11. Only those parameters that differ from standard will be reported where needed.

Each simulation consisted of two phases: During the first phase, the ERG was activated for 2,000 steps, the time needed to generate 5-10 ERG ON bursts. During this phase, data from all ERG state variables were collected and plotted for a qualitative analysis of ERG dynamics. During the second phase, the system was allowed to run for 100,000 steps, generating several hundred random ERG ON bursts. The resulting PPC activations (P_i^+, P_i^-) were mapped through a linear transformation into a set of joint angles: For each AVITE agonist-antagonist pair, the extreme activation pairs $(0, 1)$ and $(1, 0)$ were respectively mapped to joint angles of $-\pi$ (maximal extension) and π (maximal flexion) radians, with linear interpolation for intermediate activation pairs. This transformation, though arbitrary and non-anthropomorphic (the "elbow" could rotate through a full 2π radians), was useful in determining the distribution of PPC movement commands generated during the babbling phase.

Figure 11

Figure 11 shows the cumulative results of a complete simulation with the standard parameters (see caption). All figures in this section (Figures 12-18) depict results from simulations in which a single parameter or pair of coupled parameters was varied, and should thus be compared to Figure 11. All figures in this section include at least two parts: Part (a) shows the dynamics of eight different state variables from a single ERG module during the first 2,000 steps of the simulation. The relative position of each plot is meant to indicate its counterpart in the ERG schematic of Figure 6: The left column represents ON variables, and vice versa. Starting at the bottom, the first plot depicts the total input $(I + J)$, the second represents input layer activation X, the third represents available transmitter Y, and the top represents ERG output O.

Part (b) shows the cumulative distribution of PPC movement commands obtained by integrating ERG ON outputs over 100,000 steps (about 400 babbled movements). The angle attained by the two joints during each quiet phase is represented as a dot on the left-hand scatterplot. The boxes on the right are histograms of the density of dots around the center of the scatterplot at each of sixteen phases and magnitudes. Hence the "magnitude" plot represents how far from rest (center of the scatterplot) the joints were bent, and the "phase" plot shows if any particular combination of joint angles is preferred.

In general, all scatterplots showed a flat phase distribution, meaning that all quadrants of the workspace were sampled equally. Peaks in the magnitude plots reflect tendencies toward more or less extreme joint angles: Parameter choices that lead to heavily clustered dots around the scatterplot center represent small arm movements (peak on the left side of magnitude plot), and vice versa.

Random Phasic Input

In order for the ERG ON channel output to exhibit the kind of variation seen here, we assumed that the phasic input J_k^+ is stochastic in nature, as would be the case for typical cellular noise. The particular form of noise represented by equation (9) is one possible representation of random cellular activity. The resulting distribution is uniform within a closed interval of size σ_J with mean value μ_J. The actual interval size was sometimes less than σ_J, because negative values were truncated to zero. Thus if $\mu_J < \frac{\sigma_J}{2}$, the effective interval was $[0, \mu_J + \frac{\sigma_J}{2}]$ instead of $[\mu_J - \frac{\sigma_J}{2}, \mu_J + \frac{\sigma_J}{2}]$.

The parameter π_J determines the average time that elapses between input fluctuations: At each simulation step, a random integer is divided by π_J; if the remainder is zero, a random J_k^+ is chosen in the appropriate interval, otherwise $J_k^+ = \mu_J$. Hence larger values of π_J will on average lead to longer intervals between signal fluctuations. The standard choice of $\pi_J = 1$ forces a random number to be chosen at every simulation step.

Figure 11c shows a representative sample of the uninterrupted total input $I + J_k^+$ to an ERG ON channel, for a duration of 500 steps. The Pauser Gate (PG) of Figure 6 is disabled to illustrate the quality of continuous input. All other parameters are as given in Figure 11. A similar plot is added to Figures 12-15 (labelled as (c)) to compare the qualitative aspect of the total input as the various noise parameters are changed.

Figures 12-14 illustrate the effect of changes in the noise parameters μ_J, σ_J, π_J. The most important feature of these figures is the fact that the overall distribution of PPC movement commands is nearly unchanged by changes in the temporal and stochastic quality of the noise. This result shows that the distribution of PPC movement commands does not rely heavily on the distribution of the underlying noise. We now show that manipulation of other ERG parameters can be used to substantially alter the PPC distribution for a fixed choice of noise parameters.

Figures 12,13,14

Tonic Arousal

The tonic arousal I provides a baseline of activation that can energize spontaneous rebounds in the ERG OFF channel. Furthermore, opponent ERG dynamics depend on *differences* in input between the two channels, so that an increase in tonic input I, all other things equal, will diminish the effect of the differential input J_k^+. This is shown in Figure 15, where an increase in I from 0.05 to 0.15 results in a large decrease in ERG

ON output (O^+) amplitude and a corresponding decrease in the furthest extent of the workspace. Compare this to the effect in Figure 12 of changing the average noise level μ_J from 0.05 to 0.15, where large ERG ON outputs and a broad range of reaching distances are generated. Finally, if either I is much larger than J_k^+ or I equals zero, the ERG will become inactive. Hence the tonic arousal level can be used as a one-dimensional parameter to modulate ERG ON output amplitude.

Figure 15

Input Layer Parameters

The inverted-U transfer function (15) through the chemical gate depends upon the activations X_k^+. The activations X_k^+ in (11) obey a shunting equation which ensures that each cell's output will be bounded between 0 and η. The passive decay term $-\zeta X_k$ allows activation to decay to zero when no inputs are present. Solution of equation (10) at steady state yields:

$$X_k^+ = \frac{\eta[I + J_k^+(1-g_p)]}{\zeta + I + J_k^+(1-g_p)}. \tag{19}$$

Through modification of the cell parameters ζ and η, inputs I and J_k^+ are rescaled to vary the maximum size of X_k^+. As shown in the Appendix, these parameters provide a simple way to guarantee that the ON channel crashes in response to a sufficiently large differential activation in the ON channel.

The dynamic behavior of the population can also be influenced without altering the steady-state solution. For the simulations shown in Figure 16, parameters ζ and η were chosen so as to yield a similar steady-state value of X_k^+ under the standard input conditions. However, a proportional increase in both ζ and η causes the activation X_k^+ to fluctuate more rapidly in response to the noisy input J_k^+, giving rise to more diverse ERG ON output bursts. As a result, the integrated PPC movement commands exhibit a broader distribution. If, on the other hand, both ζ and η were decreased, the input layer activation X_k^+ would be less sensitive to rapid phasic input fluctuations, and more uniform ERG ON bursts would obtain.

Figure 16

Chemical Transmitter Gate

The chemical gate Y_k is a key feature of ERG design, since the transmitter habituation law (12) and release law (14) together give rise to an inverted-U synaptic transfer function in equation (15). The quadratic term in equation (13) insures that a large enough phasic input will cause the gate to transiently rise above zero, and then spontaneously crash. Cells with this type of transfer function have been reported to exist in a number of preparations (e.g., Wachtel and Kandel, 1971), including preparations involving rhythmic pattern generators (e.g., Sigvardt and Mulloney, 1982).

As shown in Figure 17, changes in the maximum amount of stored transmitter λ in equation (12) affect the amplitude of each ON burst, without significantly altering the size or duration of each burst, or the duration of the quiescent (OFF) phase following each burst. The effects of modulation of the remaining parameters in equations (11)-(13) are discussed in the Appendix.

Figure 17

Pauser Gate

The Pauser Gate g_p in (18) determines when the phasic input $J_k^+(1-g_p)$ in (11) will affect the input layer based on how much activity occurs in the OFF channels. As in (18), the output of all OFF channels is summed at the PG. If the threshold θ_P is exceeded, the PG becomes active and shuts off the phasic input, causing a transient OFF rebound. A smaller θ_P tends to cause longer quiescent phases between ON bursts, without altering the general shape or duration of the ON bursts themselves, as shown in Figure 18. This is due to the fact that the declining phase of the ON burst is quite rapid, and thus insensitive to small changes in θ_P, whereas the last portion of the OFF phase is driven by the slow accumulation of transmitter in the ON channel. The PG threshold can thus be used to control the temporal characteristics of the ERG output without noticeably affecting the output ON vector distribution. Setting θ_P to zero or to a large enough value will eliminate the cyclic behavior of the ERG, thus providing an additional nonspecific parameter for overall control of ERG activation. This dependency is illustrated in Figure 18c, which shows the number of ERG ON bursts generated during 10,000 simulation steps for various values of θ_P.

Figure 18

15 AVITE Simulations: Linear PPC→TPC Map

Sections 15-21 present results of AVITE simulations. The standard AVITE parameters for all simulations, unless noted, are: $\alpha = 5.0$, $\beta = 0.0001$, $\gamma = 0.05$, $\delta = 5.0$, $\epsilon = 0.01$. The AVITE training cycle consists of generation of random PPC movement commands, followed by quiet phases during which the PPC is copied to the TPC through the NP gate. During the quiet phase, learning in TPC→DV synapses is driven by an internal measure of mismatch, namely by nonzero activation in the DV population.

In this section we assume that a one-to-one linear mapping takes place when copying the PPC to the TPC at the end of an ERG ON burst, so that the TPC→DV synapses are simply learning a linear gain factor. Then equations (7) and (8) become:

$$F_i^+ = \rho g_n P^+ \tag{20}$$

and

$$F_i^- = \rho g_n P^-, \tag{21}$$

where ρ represents a linear gain factor. The simulations in this section assume $\rho = 1$, although other choices, including a different choice for each channel, have been shown to work. This is a natural starting point for tests of the learning laws. More complicated mappings are considered in later sections.

We begin all training simulations with the LTM weights Z_i^+ in (4) set to zero, although the results hold for other initial choices of LTM values. At first, the DV during each quiet phase is large and negative due to the negligible positive input from the TPC. As motor babbling proceeds, the DV gradually approaches zero. Figure 19 shows the error in the agonist (V^+) and antagonist (V^-) channels of a single AVITE module, as well as the total error ($|V^+| + |V^-|$).

Figure 19

A more graphical demonstration of correct adaptive control by the AVITE model is given in Figure 20. Each small grid illustrates the graphical display of the program, with the arm in a position determined by two joint angles as indicated in Section 14. The target joint configuration appears as a triangle on each grid. For each grid, the arm is started from its resting configuration ($P_1^+ = P_1^- = P_2^+ = P_2^- = 0.5$), the target command is selected ($T_1^+ = 0.3$, $T_1^- = 0.7$, $T_2^+ = 0.4$, $T_2^- = 0.6$), and the GO signal is turned on ($G = 1.0$). Figures 20a-e show that terminal reaching behavior improves at increasing levels of AVITE training. The learning rate and gating are the same as in Figure 27. Figure 20f shows reaching behavior at the same training level as in Figure 20e, but for a different target command ($T_1^+ = 0.75$, $T_1^- = 0.25$, $T_2^+ = 0.65$, $T_2^- = 0.35$). Note that the same terminal reaching behavior can be achieved with a much higher learning rate, and requires only few hundred steps (a couple of babbled movements). Because of the one-to-one, linear mapping, the LTM traces Z_i are simply learning a linear gain factor, so that performance will be accurate throughout the workspace even if only one or two positions have been sampled.

Figure 20

16 Motor-to-Spatial PPC→TPC Maps

In the previous section, the TPC is isomorphic to the PPC, so that activation of a single TPC unit codes a desired amount of contraction of a prescribed muscle group. During visually guided reaching, a target location represented in spatial coordinates is transformed from spatial to motor coordinates. This suggests that either (a) the TPC itself must represent targets in spatial coordinates, or (b) there exists a spatially coded processing stage whose output is transformed into motor coordinate targets prior to reaching the TPC processing stage. We now analyze the first possibility, and defer the second to Section 22.

If the TPC codes targets in spatial coordinates, then the location and not the amplitude of TPC activations determines target position. In the simplest realization of this case, the PPC→TPC pathway performs a hard-wired transformation from motor to spatial coordinates, and the TPC→DV synapses learn the reverse transformation to insure proper matching at the DV (Figure 21). A similar adaptive problem was solved with the Head-Muscle Interface model of Grossberg and Kuperstein (1986,1989, Chapter 4). We now show how a Vector Associative Map, specialized as an AVITE circuit, can learn the appropriate transformation.

Figure 21

Let the TPC consist of a one-dimensional layer of spatially-organized units, i.e., different targets are encoded by activation of different units. Furthermore, let the TPC consist of recurrently connected cells or cell populations obeying a shunting law, as in (6), of the form:

$$\frac{dT_j}{dt} = \delta \left[-\epsilon T_j + (1 - T_j)(E_j + F_j + m(T_j)) - T_j \left(\sum_{k \neq i} m(T_k) \right) \right], \tag{22}$$

where term $m(T_j)$ represents self-excitation, and term $\sum_{k \neq j} m(T_k)$ represents recurrent inhibition. Grossberg (1973) has shown that total activation across the field is approximately normalized, and that appropriate choices of feedback signal function $m(T_j)$ lead to contrast enhancement of the total input pattern $\{E_j^+ + F_j^+\}$, including winner-take-all, or maximal compression, of the input pattern. We will first consider the simplest case of maximal compression before analyzing distributed spatial TPC maps. In this case, when the ERG OFF opens the Pauser Gate (PG), the current (P^+, P^-) pair is transformed into a unimodal spatial distribution of inputs $\{F_j\}$ from which the recurrent shunting dynamics choose the maximally activated node and inhibit all other nodes.

The selected T_j drives both V^+ and V^- toward zero according to the learning law (4), and the DV activation law (3) is changed to reflect the multiple signals from the TPC:

$$\frac{dV^+}{dt} = \alpha \left(-V^+ + \sum_j T_j^+ Z_j^+ - P^+ \right) \tag{23}$$

In the winner-take-all case, at most one summand in $\sum_j T_j^+ Z_j^+$ is positive at any time.

After learning, each TPC unit can read-out the (P^+, P^-) pair that activated it. Grossberg and Kuperstein (1986, 1989, chapter 6) have described several neural circuits that can perform such a motor-to-spatial transform. We introduce here a related model that transforms PPC amplitude changes into a shifting TPC activation peak of nearly constant amplitude.

17 The Difference-of-DOGs Spatial Map

Consider a rest interval when $g_n = 1$. Suppose that the activation pair (P^+, P^-) is filtered through a pair of Difference-Of-Gaussian (DOG) kernels D^+ and D^-, respectively. Suppose that the kernels D^+ and D^- are spatially out of phase. For definiteness, let D^- be centered at the leftmost TPC unit ($j = 0$) and let D^+ be centered at a position $j = j_0$ to the right of $j = 0$. Thus

$$D_j^- = \phi \exp\left[-\frac{j^2}{2\chi^2}\right] - \psi \exp\left[-\frac{j^2}{2\omega^2}\right] \tag{24}$$

and

$$D_j^+ = \phi \exp\left[-\frac{(j-j_0)^2}{2\chi^2}\right] - \psi \exp\left[-\frac{(j-j_0)^2}{2\omega^2}\right]. \tag{25}$$

Also suppose that the signal $P^- D_j^-$ is inhibitory whereas the signal $P^+ D_j^+$ is excitatory at the spatial TPC field; that is, a Difference-Of-Difference-Of-Gaussians (DODOG) is registered:

$$F_j(P^+, P^-) = P^+ D_j^+ - P^- D_j^-. \tag{26}$$

Function $F_j(P^+, P^-)$ is unimodal in shape, with a maximal value that shifts in position as P^+ and P^- vary in a push-pull fashion ($P^+ + P^- = 1$). Figure 22 illustrates results for two choices of DODOG parameters, one leading to a sigmoidal shift (solid lines), and the other leading to a more linear shift (dashed lines). Part (a) plots $F_j(P^+, P^-)$ as a family of functions of j as P^+ increases from 0 to 1, and P^- correspondingly decreases from 1 to 0. Part (b) plots the location receiving maximal activation as a function of P^+, while part (c) shows the corresponding value of F_j at the location of maximal activation. The approximately linear shift indicates that equal changes in muscle contractions correspond to approximately equal shifts in the location of peak activation over the spatial map. The sigmoidal shift in location indicates that more extreme (P^+, P^-) pairs, corresponding to more extreme joint angles, will be sampled less densely than activation pairs near the resting configuration ($P^+ = P^- = 0.5$). In both cases, the maximal amplitude varies only gradually with peak location (less than one order of magnitude between minimum and maximum), and recurrent shunting dynamics at the spatial TPC can easily sharpen and normalize these distributions.

Figure 22

18 AVITE Simulations: Winner-Take-All Linear Spatial Map

Figure 23 illustrates learning using a winner-take-all, or maximal compression, spatial PPC→TPC map. For these simulations, the spatial map and ensuing TPC recurrent competition were replaced by a spatially linear algorithm for computational simplicity. Thus, when the NP gate opens, the PPC activation (P^+, P^-) activates the TPC spatial position j (i.e., $T_j = 1.0$) according to the equation

$$j = N \cdot P^+, \tag{27}$$

where N represents the total number of TPC nodes ($N = 40$ in the figure). Equation (27) maps (0,1) to the leftmost node and (1,0) to the rightmost TPC node, with a linear interpolation for intermediate (P^+, P^-) pairs.

The plot shows the LTM values Z_j^+ (synapse from T_j to V^+, plotted as a solid line marked by '*'), and Z_j^- (synapse from T_j to V^-, plotted as a dashed line marked by 'x') after 100,000 steps (about 400 movements). Since $T_j^+ = 1$, the input to (V^+, V^-) equals (Z_j^+, Z_j^-). The plot confirms that the LTM traces have learned the correct linear transformation. The LTM traces near the extremities of the TPC field are zero because these positions have not been sampled during babbling.

Figure 23

19 AVITE Simulations: Winner-Take-All Nonlinear Spatial Map

Figure 24 illustrates learning when the PPC activation range is transformed through a nonlinear spatial map. The TPC node that becomes active when the NP gate is open is determined by:

$$S = \begin{cases} N\frac{(P^+)^4}{(0.5)^4+(P^+)^4} & \text{for } 0 \le P^+ \le 0.5 \\ N\frac{(0.5)^4}{(0.5)^4+(1.0-P^+)^4} & \text{for } 0.5 < P^+ \le 1 \end{cases} \tag{28}$$

Equation (28) describes a sigmoidal shift function similar to the one shown in Figure 22b (solid line). This nonlinear shift causes central TPCs to be more densely sampled than extreme TPCs. Figure 24a shows the transformation generated by equation (28), and Figure 24b shows that the VAM is able to learn the reverse transformation.

Figure 24

20 AVITE Simulations: Distributed Spatial Map

We now consider map learning when the shunting competition (22) at the TPC allows more than a single TPC node to be active during learning. Equations (4) and (5) imply that the synapses from all active TPCs grow at the same rate to cancel the (V^+, V^-) activation. For the present simulations, we allowed the amplitude of TPC activation to determine the rate of learning; namely, we replaced (5) by $f(T_j) = T_j$, so that (4) becomes

$$\frac{dZ_j^+}{dt} = g_n T_j(-\beta Z_j^+ - \gamma V^+). \tag{29}$$

In this case, the synapses from all active TPC nodes will be driven to the same pattern (P^+, P^-), but at different rates. If for example the feedback signal function $m(T_j)$ in equation (22) is sigmoidal, the TPC recurrent dynamics sharpen the input pattern (Grossberg, 1973, 1976), leading to faster learning rates by the most active node, with progressively slower learning by neighboring nodes. Using a distributed map allows nodes to learn approximately correct synaptic gains even if their exact spatial locations have never been sampled through motor babbling. If a node has never been directly sampled, but its neighbors on both sides have, then that node learns a pattern that is an average of its neighbor's patterns, with a bias for the more frequently sampled pattern (Grossberg, 1976, 1978, 1982; Kohonen, 1983, 1984). If sampling only happened for neighbors to one side, that node will learn the same pattern as its neighbor.

Figure 25

Figure 25 shows the results using the same sigmoidal mapping as in Figure 24a. When the NP gate opened, we let several TPC nodes become active, with activity decaying inversely with distance from the central peak. The reverse transformation was learned correctly, and the distributed spatial map led to faster learning, as illustrated in Figure 26: Figure 26a shows the LTM traces for the maximal compression sigmoidal map after 20,000 simulation steps (about 80 movements). Many of the LTM traces are still near zero. Figure 26b shows results when the spatial map activates two nodes on each side of the central peak, and Figure 26c when the activation includes five nodes on either side. For each of these examples, we calculated the standard deviation between the LTM traces for a single channel and the calculated inverse sigmoid from equation (28). The standard deviation is greatest for the maximal compression simulation ($\sigma = 0.145$), and decreases as the activation spreads to two ($\sigma = 0.093$) and five ($\sigma = 0.079$) neighboring nodes to either side of the peak. Similar results hold for other types of distributed spatial maps.

Figure 26

21 Gating of AVITE Learning During Endogenous, Reactive, and Planned Movements

As noted in Section 7, the AVITE must be able to distinguish between learning and performance trials without losing its ability to remain on-line at all times. The ability to copy a stationary PPC into the TPC for learning could potentially lead to destabilizing effects: If the NP gate were open at all times, the PPC would be continuously copied into the TPC, even when it does not represent the same position in space as the TPC. To prevent this, the NP gate and the ERG are inhibited whenever a voluntary movement occurs.

In order to autonomously carry out these control functions, there must exist internal states capable of discriminating between endogenous babbling, learning, and planned performance phases. The babbling and learning phases are demarcated by specific events in the ERG: The Pauser Gate, or PG, becomes active at the onset of the quiet phase, and enables babbling to resume by becoming inactive. Hence the NP gate can be coupled to the PG, so that PPCs will only be copied into the TPC stage during the quiet phase (Figure 9). In addition, a nonspecific arousal signal from the PG can be used to modulate learning, so that the TPC→DV synapses are only plastic while the NP gate is open, as in equations (4) and (29). This type of nonspecific modulatory signal has been demonstrated in a number of biological preparations (e.g., Singer, 1985).

Gating of the learning signal is not required under some circumstances. If the learning rate is slower than the integration rate of PPC and TPC, then the amount of learning that takes place during the quiet phases will be statistically significant, whereas learning of incorrect (PPC,TPC) pairings will be statistically insignificant. This is due primarily to the symmetry of the learning law (4). Because the LTM traces can increase and decrease at equal rates in response to negative or positive DV fluctuations, and because the movements during babbling tend to be random, errors due to learning during active babbling tend to zero. Figure 27 illustrates the absolute value of the error summed for both agonist and antagonist DV at the onset of each quiet phase during training with ungated learning. The error approaches zero more rapidly than in the gated learning paradigm of Figure 19.

Figure 27

In addition to gating learning off during endogenous movements, it is equally important to gate learning during reactive or planned movements. The ERG must also be shut off when an external target command (E^+, E^-) is instated at the TPC, as in equation (6). This can be accomplished in two ways:

TPC-Mediated Gate

The populations that input a target command to the TPC can simultaneously send a non-specific gating signal to shut off the NP and ERG gates. For example, a non-specific signal that drives the tonic input I to zero in (11) will shut off the ERG, and thus also shut off the NP gate. Alternatively, a nonspecific signal could raise the PG threshold θ_P in (18) to a high enough level to inactivate the PG and thereby shut off the ERG.

GO-Mediated Gate

Here, the GO signal shuts off the ERG and prevents the current PPC from degrading the desired TPC. In this scheme, if the TPC becomes active before the GO signal turns on, as in motor priming (Section 4), then the TPC can be altered by PPC feedback through the NP gate if passive or endogenous movements occur before activation of the GO signal. Notwithstanding this difficulty, a GO-activated gate is conceptually attractive, because the GO signal seems to be the counterpart, for reactive and planned movements, of the activity source which energizes the ERG during endogenous movements. Inhibition of the ERG by the GO signal thus describes a competition between two complementary sources of motor arousal, much as complementary arousal sources for consummatory behavior and orienting behavior compete in models of reinforcement learning (Grossberg, 1982; Grossberg and Schmajuk, 1989).

Simulations have shown that either alternative is workable. The following section shows how a GO-mediated gate can be used without causing a problem of spurious AVITE learning during motor priming.

22 A Cascade of Intermodal and Intramodal VAMs

We now analyze the second hypothesis suggested in Section 16 that the AVITE TPC encodes muscle coordinates, and that there exists a processing level prior to the TPC that transforms spatially-encoded targets into muscle coordinates. In particular, we show that an intermodal VAM can be used to learn this spatial-to-motor transformation

(Figure 28).

In order to unambiguously describe such a VAM cascade, in which spatial-to-motor and motor-to-motor transformations occur among TPCs, DVs and PPCs, we introduce the following notation. Let TPC_s denote a TPC coded in spatial coordinates, and TPC_m denote a TPC coded in motor coordinates. Correspondingly, let DV_{sm} denote a DV that transforms TPC_s into TPC_m. For notational simplicity, let DV_m (rather than DV_{mm}) denote a DV that transforms TPC_m into PPC within an AVITE module. Thus the subsequent discussion considers the sequence of VAM transformations $\mathrm{TPC}_s \rightarrow \mathrm{DV}_{sm} \rightarrow \mathrm{TPC}_m \rightarrow \mathrm{DV}_m \rightarrow \mathrm{PPC}$, as shown in Figure 28.

We assume that movements of the arm during babbling are tracked by the visual system. For simplicity, we first assume that a single population encodes the arm's position in spatial coordinates, as discussed in Sections 18 and 19.

Figure 28

During the quiet phase of each babbled movement, the PPC is directly copied into TPC_m (motor TPC), so that the latter accurately reflects the current outflow movement command signals for tuning the intramodal LTM traces of the $\mathrm{TPC}_m \rightarrow \mathrm{DV}_m$ pathways. The intermodal VAM at the top of Figure 28 transforms TPC_s (spatial TPC) into TPC_m via the intermodal DV_{sm}. If the visual system accurately tracks the moving hand, this DV_{sm} approaches zero as the $\mathrm{TPC}_s \rightarrow \mathrm{DV}_{sm}$ LTM traces learn the correct spatial-to-motor transformation, as in the intramodal examples of Sections 15 and 16. Figure 29 shows learning by the intermodal LTM traces of the correct linear transformation from spatial position to motor coordinates. In this example, activation of the TPC_s was distributed to five nodes on either side of the activation peak, using a linear mapping such as the one described in Section 18. Nonlinear transformations, such as those presented in earlier sections, have also been shown to work. In all cases, learning was driven by a DV equation such as equation (3), with activity-dependent gating as in equation (29).

Figure 29

The intermodal VAM circuit performs the same function as a standard AVITE module, meaning that instatement of a spatial target at the TPC_s with a non-zero GO signal leads to integration of the correct muscle-coordinate target by the TPC_m, which in turn gives rise to a synchronous arm movement trajectory by the intramodal VAM, or AVITE, module. Instatement of a TPC_s command when the GO signal is zero primes a DV_{sm} without disrupting the previously stored TPC_m.

In addition to showing the versatility of the VAM, this scheme segregates intermodal and intramodal learning, and illustrates the principle of supercession of control in sensory-motor systems. The intramodal AVITE is the first to become trained, and it relies entirely on a measure of error based on internal feedback. Learning enables target commands in muscle coordinates to generate correct feed-forward arm trajectory commands. At a higher level, the intermodal VAM requires feedback through the environment for learning, but is eventually able to generate feed-forward commands from TPC_s to TPC_m which are capable, in turn, of controlling arm movements through the calibrated AVITE.

This segregation of intermodal and intramodal control simplifies gating in the AVITE. Because primed targets at the TPC_s are unable to perturb the AVITE TPC_m unless the GO signal is active, the NP gate can be left open whenever the GO signal is zero. The TPC_m can thus continuously be updated to reflect the PPC at all times, except when the GO signal is active, at which time the NP gate closes to avoid conflicts between intermodal target commands and intramodal training signals. Similarly, because the fast integration at the TPC_m keeps it always similar to the PPC even during movement, the intramodal learning rate can be kept high and requires no gating. In fact, because TPC_m and PPC are almost always equal—instead of only being equal during the quiet phase—error convergence in the DV_m is significantly faster than in the examples of the previous sections even with the same learning rate. Furthermore, segregation of intermodal and intramodal target commands allows priming of target commands in spatial coordinates even during active AVITE babbling.

The idea that learning of intramodal calibration parameters through motor babbling can take place prior to any form of visually-guided movements is supported by developmental data (e.g., Bushnell, 1985). In fact, rhythmic endogenous movements have been monitored in the human fetus from as early as midgestation (Robertson, 1985). The ability to learn intramodal parameters before birth may be important for movements that do not require visual feedback for their calibration, and may be needed for infants of species that must be able to perform motor tasks from birth.

The GO-mediated gate also allows the AVITE circuit to continue its calibration of $\text{TPC}_m \rightarrow \text{DV}_m$ LTM traces during adulthood, long after the ERG is no longer spontaneously active. Moreover, the learning rate can be chosen large, because the probability of spurious (TPC_m, PPC) correlations is small.

This scheme still leaves open the question of how best to gate intermodal learning. Bullock and Grossberg (1988a) suggested that intermodal learning between TPCs should be gated shut except when the DV of the intramodal VITE model is small. In the VAM cascade of Figure 28, this suggestion gains a fuller realization. The DV_m of the AVITE model is large if either the PPC differs significantly from the TPC_m, or if the pathways $\text{TPC}_m \rightarrow \text{DV}_m$ are incorrectly calibrated. In the former case, the arm has not yet approached its desired target. In the latter case, the target representation is unreliable. If the DV_m stage gates learning at the next, intermodal DV_{sm} stage, and the eye-head system can accurately track the hand-arm system, then significant spurious learning can occur only if actively primed movements are not released for long time intervals relative to the intermodal learning rate. A further analysis of this possibility is a topic for future research.

23 Learning of an Invariant Multimodal VAM

The results of Sections 15-22 illustrate the ability of the VAM to provide on-line learning and performance for a variety of intra- and inter-modal control schemes. We conclude the simulations for this article with an example of a VAM Cascade learning an invariant, multimodal, spatial-to-motor associative map. This example will serve as the basis for future research.

Figure 30

The act of reaching for visually-detected targets in space is known to involve a number of different modalities: For instance, the position of the target on the retina and the position of the eyes in the head are needed to calibrate an eye movement. In addition, the position of the head in the body, and the position of the arm with respect to the body are needed for correct execution of an arm movement. In particular, the position of a target with respect to the body can be represented by many combinations of eye positions in the head and target positions on the retina. We now show that a VAM is able to learn an invariant multimodal mapping; that is, it can learn to generate a correct movement command for all combinations of retinal and eye positions corresponding to a single target position. We illustrate this competence with perhaps the simplest class of examples. In one example, the retinal position of the target and the initial position of the eye in the head combine to generate a desired position of the eye in the head. In the other example, head and eye size are ignored, and a single "cyclopean" eye rotates around the same axis as a one-joint arm of fixed length. Due to these simplifications, a one-to-one correspondence exists between a head-centered representation of space, built up from combinations of retinal and eye position signals, and the endpoint of the arm. These examples merely illustrate VAM capabilities. VAMs have also been used to self-organize a body-centered representation of 3-D space that is capable of controlling a multi-joint arm to perform sequential planned actions at any realizable locations and size scales within the workspace, with or without a tool of variable length (Bullock, Greve, Grossberg, and Guenther, 1990).

Both of the examples described herein can be handled by the same formal apparatus. For definiteness, we interpret the analysis in terms of arm movements. In Figure 30, the two top spatial maps represent the horizontal position of the target on the retina, and the horizontal position of the eyes within the head. For simplicity, we consider one-dimensional spatial maps, and we assume a linear relationship between the change in arm position and the total change in retinal position and eye position. That is,

$$i_E + j_R = H, \tag{30}$$

where i_E represents activation of the i^{th} node of the eye position map; j_R represents activation of the j^{th} node in the retinal map; and H is linearly related to arm position. In particular, if there are N nodes in the eye-position map and M nodes in the retinal map, we let

$$H = (N + M)P^{+}. \tag{31}$$

By (30), each fixed target position H can be represented by many combinations of eye position and retinal position. In particular, equations (30) and (31) indicate that for a fixed AVITE outflow command (P^{+}, P^{-}), a rightward shift in eye position (i_E increases) is cancelled by a leftward shift in retinal position (j_R decreases), and vice versa. This set-up is similar to that used to learn the Invariant Target Position Map of Grossberg and Kuperstein (1986, 1989, Chapter 10). Our results herein show how to learn such a map using a VAM cascade.

For the simulations, the arm position H during each quiet phase of babbling is mapped into one or more random (i_E, j_R) pairs that satisfy equations (30) and (31). These equations embody the assumption that intramodal learning has already taken place in the eye movement system, so that the eyes can reliably track the moving arm. Then the active node i_E in the eye position map and j_R in the retinal position map can sample the current arm position registered at the AVITE TPC$_m$. However, the VAM activation is affected by activity in both populations, so that the filtered signal from each population only needs to be half as strong as it would be if only one population were present (as in Section 22). This is reflected in Figure 31. Here the LTM traces have learned the correct linear map, but their values are half those achieved with a single map (Figure 29). After training, instatement of a target (i_E, j_R) when the GO signal is positive, moves the arm to the correct location according to equations (30) and (31). Changes in i_E and j_R such that $i_E + j_R$ remains unchanged do not change the position of the arm.

Figure 31

Similar results hold if the two intermodal populations are not in the same coordinate system. For example, the horizontal eye position could be coded by a pair of nodes that represent the muscle lengths for an agonist-antagonist pair of oculomotor muscles.

24 Adaptive Gain Control and Error-Based Learning by Multiple Brain Regions

The AVITE model and its VAM generalization are part of a long history of biologically motivated models for error-based learning by neural networks. In their simplest form, these models function as mechanisms for feedforward adaptive gain control. The cerebellum has been one brain region that has attracted a long history of such models.

Grossberg (1964) and Brindley (1964) were among the first to suggest that learning occurs at the synapses between cerebellar parallel fibers and Purkinje cell dendritic spines, using the climbing fibers as a teaching signal. Grossberg (1969) further modelled this concept, as did Marr (1969), Albus (1971), and many subsequent authors. Marr (1969) suggested that these synapses increase in strength due to learning; Albus (1971) that they decrease in strength. Grossberg (1969) suggested that they may either increase or decrease in strength, depending upon the learning context. These models were followed by many subsequent cerebellar modelling contributions (e.g., Ito, 1974, 1984; Fujita, 1982a, 1982b; Grossberg, 1972b).

The hypothesis in Grossberg (1969) that adaptive gains may either increase or decrease due to learning was further developed into a model of *opponent learning* in Grossberg and Kuperstein (1986, 1989). These authors developed the view that one role of the cerebellum is to function as a universal feedforward adaptive gain controller, whose internal architecture may be used by many sensory-motor systems. They showed how error signals, computed by one or another form of mismatch, may be used to drive the opponent learning process. It was shown, for example, how error signals that compute (1) distance of a visual target from the fovea, (2) outflow-inflow mismatches, and (3) whole-field visual drifts, among others, could be used for control of the saccadic eye movement system. In Bullock and Grossberg (1990), it was shown how outflow-inflow mismatches may be detected by muscle spindles and used by the cerebellum as error signals to trigger learned compensation for errors in arm reaching movements.

The present results describe error-based learning of associative maps that may encode more general properties than adaptive gains. The AVITE model has, however, been interpreted in terms of brain regions other than the cerebellum; in particular, the parietal cortex, motor cortex, and the basal ganglia. In its full generality, the VAM model may be instantiated in yet other brain regions. The Passive Update of Position circuit (Figure 3; Bullock and Grossberg, 1988a) and the circuits for control of multi-joint arms in 3-D body-centered space with or without tools (Bullock, Greve, Grossberg, and Guenther, 1990) provide two other VAM-based systems where such brain interpretations must be sought.

In addition, guided by recent data suggesting that the predicted error-based signals in cerebellum may drive a learning process, Houk, Singh, Fischer, and Barto (1989) have described a cerebellar "model ... closely related to ... [the] limb control [model of] Bullock and Grossberg (1988)." However, these authors have interpreted the cerebellar data in terms of a model for control of arm trajectory generation, not merely adaptive gain control. Although Bullock and Grossberg (1990) have noted a number of formal problems of the Houk *et al.* model in its present form, the generality of the VAM concept suggests that VAM-type circuits may be instantiated in a variety of brain regions.

25 Physiological Modulators of Central Pattern Generators and Unsupervised Error-Based Learning

The complete ERG-AVITE model joins together two types of neural circuits in order to accomplish autonomous sampling of the workspace and unsupervised real-time error-based learning of associative maps.

The ERG (Sections 10 and 13) models a type of tonically active central pattern generator, or CPG, using a specialized gated dipole circuit (Grossberg, 1972, 1982, 1984). All gated dipole circuits share a small set of key design elements: A source of tonic arousal, phasic inputs, habituating transmitter gates, opponent interactions, and nonlinear (in particular, rectified) signals. Within this general design framework, specialized gated dipole circuits have by now been used to systematically model a wide variety of challenging behavioral and neural data. In some of these applications, gated dipoles do not persistently oscillate; for example, in applications to vision (Carpenter and Grossberg, 1981; Grossberg, 1982, 1987a, 1987b, 1990b; Grossberg and Mingolla, 1985; Grossberg and Rudd, 1990), reinforcement learning (Grossberg, 1987a; Grossberg and Schmajuk, 1987, 1989), cognitive information processing (Banquet and Grossberg, 1987; Carpenter and Grossberg, 1987; Grossberg, 1982; Grossberg and Gutowski, 1987), and the analysis of behavioral disorders (Grossberg, 1984, 1987a). An oscillatory gated dipole, distinct from the one modelled here, has also been used to quantitatively simulate a large body of data about the circadian rhythms generated by the suprachiasmatic nuclei of the hypothalamus (Carpenter and Grossberg, 1983, 1984, 1985; reprinted in Grossberg, 1987a).

These various phasically reactive and persistently oscillatory gated dipoles differ from one another only by modest changes of their anatomical connections or physiological mechanisms. The family of these models therefore illustrates how parametric changes in a relatively simple neural circuit module can generate a variety of qualitatively different dynamical properties. In all applications, the specialized models are tested against data by noting how multiple model properties covary as individual parameters are varied.

Selverston (1988) has discussed CPGs in the light of recent data demonstrating that parametric changes can alter a CPG's qualitative properties. He wrote (p.117) that: "The idea that neural networks in general are rigid 'hard-wired' circuits needs to be replaced in most cases with the notion of extremely flexible circuits which can be 'sculpted' out of anatomical networks by the actions of modulators. Circuits can adapt not only by changing synaptic strength but by altering virtually every physiological parameter available to it." Modulators play a key role in regulating the dynamics of the ERG-AVITE model, including the action of the habituating transmitter gate in (16) and (17), the action of the pauser gate in (11) and (18), and the action of the now print gate in (4), (7), (8), and (29).

Selverston (1988) also takes neural modellers to task because "usually only the ... I/O properties—the relationship between membrane potential and spike firing rate, generally a sigmoidal function ... is actually considered" (pp.110-111). In contrast to such oversimplifications, he lists seven basic cellular properties, and five synaptic properties, as a subset of forty-six neuron properties that have been reported in experiments. Selverston's critique arises from his impression that "a good deal of the impetus for new computational schemes comes from classical physics where the properties of the elements are quite simple" (p.109).

Actually, the main neural modelling ideas that Selverston's physicists are using represent only a subset of a greater neural modelling literature on which many of today's models are based. Essentially all the properties described by Selverston have been used to explain parametric sets of behavioral and neural data within this greater neural modelling literature. In particular, many qualitative features of Selverston's own data about the lobster stomatogastric ganglion (Miller and Selverston, 1982a, 1982b; Selverston and Moulins, 1987) are strikingly similar to those of the oscillator that has been used to model circadian rhythms of the suprachiasmatic nuclei (Carpenter and Grossberg, 1983, 1984, 1985).

An important new role for modulators, or gates, in regulating adaptive behavior is described in this article. Such gating actions enable the AVITE model, and more generally VAM models, to carry out autonomous learning in real-time using the same signal pathways for DV-based map learning as for DV-based map performance. As noted in Section 7, a VAM network needs to distinguish whether $DV \neq 0$ because the TPC and PPC represent different target positions, whence learning should not occur, or because the TPC→DV synapses are improperly calibrated, whence learning should occur. Gates that modulate complementary dynamical states also arise in other biologically derived neural models, such as Adaptive Resonance Theory, or ART (Carpenter and Grossberg, 1987a, 1987b, 1988, 1990). Here gates control switching between the complementary states of attention/learning and hypothesis testing/memory search.

In the remaining sections we show that the ART and VAM models themselves embody complementary properties on a more macroscopic level of brain design, and that together they may enable a complete autonomous system to be developed.

26 Towards a System-Level Synthesis of Complementary ART and VAM Designs

In learning and performance by a VAM, the matching event is *inhibitory*. For example, in an AVITE model, matching a TPC with a PPC zeroes the DV. This is the basis for saying that VAM learning is *mismatch* learning: Learning occurs only when DV$\neq 0$ and drives the DV mismatch to zero. In contrast, a complementary type of learning occurs in ART models, which are also capable of autonomous real-time learning. In ART, learning is *approximate-match* learning; that is, learning occurs only if the match between the learned top-down expectation (cf., the AVITE TPC→DV signals) and the bottom-up input pattern (cf., the AVITE PPC→DV signals) are sufficiently close that the orienting, or novelty, subsystem is inhibited, and matching by the 2/3 Rule causes a fusion event, or attentional focus, or resonant state to develop which drives the learning process.

Corresponding to these complementary learning rules are complementary rules for top-down priming. In a VAM model such as AVITE, the top-down TPC→DV signals prime a *motor expectation*. When this expectation is matched by a PPC, the limb has already moved to its target. No further movement is needed, and the DV is zeroed, or inhibited. In ART, by contrast, a top-down *sensory expectation* prepares the network for an anticipated bottom-up event that may or may not occur. If the event does occur, then matching causes resonant excitation, not inhibition.

Thus the two complementary learning rules coexist with two complementary rules for top-down priming, or intentionality.

Sensory-cognitive circuits seem to be designed according to ART-style processing whereas cognitive-motor circuits seem to be designed according to VAM-style processing. In particular, Carpenter and Grossberg (1988) and Grossberg (1988) have noted that ART-style learning is stable in response to an arbitrary sequence of sensory input patterns, for purposes of recognition learning and reinforcement learning. These authors contrasted the stability of ART learning with instabilities of mismatch learning, notably learning by perceptrons and back propagation, when they are used for recognition learning and reinforcement learning. Carpenter and Grossberg also analyzed why back propagation is not a real-time model; rather it needs to be run off-line under carefully controlled conditions, including a slow learning rate.

VAM models, in contrast to back propagation, are capable of real-time processing. They are designed to carry out both learning and performance within the same processing channel by using self-controlled real-time gating of complementary learning and performance modes. Such gating also enables VAM learning to be fast. Within an intramodal VAM, such as AVITE, fast learning is always stable because the "back propagation" from PPC to TPC automatically assures that correct (TPC,PPC) correlations are learned. In this sense, although AVITE learning is *mismatch* learning, it is based upon self-controlled *matches* of PPC and TPC. Within an intermodal VAM that takes its data partly from prior stages of sensory processing, fast learning is stable because ART mechanisms assure the stability of the sensory representations themselves.

Taken together, the ART and VAM models provide a framework for designing stable real-time fast-learning systems that exploit both approximate-match learning and mismatch learning. ART networks can achieve stable real-time fast-learning of recognition and reinforcement codes. VAM networks, fed by outputs from the stable ART networks, can be used to achieve stable real-time fast learning of sensory-motor maps. Thus, all the benefits of approximate-match learning and mismatch learning, and the corresponding benefits of both excitatory matching and inhibitory matching, including their respective modes of top-down priming, or intentionality, can be achieved by incorporating them both into an appropriately cascaded neural architecture wherein they may be understood as complementary aspects of a larger system design.

References

Albus, J.S. (1971). A theory of cerebellar function. *Mathematical Biosciences*, **10**, 25-61

Anderson, R.A., Essick, G.K., and Siegel, R.M. (1985). Encoding of spatial location by posterior parietal neurons. *Science*, **230**, 456-458.

Banquet, J.P. and Grossberg, S. (1987). Probing cognitive processes through the structure of event-related potentials during learning: An experimental and theoretical analysis. *Applied Optics*, **26**, 4931-4946.

Brindley, G.S. (1964). The use made by the cerebellum of the information that it receives from sense organs. *International Brain Research Organizational Bulletin*, **3**, 80.

Bullock, D. (1987). Socializing the theory of intellectual development. In M. Chapman and R.A. Dixon (Eds.), **Meaning and the growth of understanding: Wittengstein's significance for developmental psychology.** New York:Springer-Verlag, 187-218.

Bullock, D., Greve, D. Grossberg, S., and Guenther, F. (1990). Self-organizing neural networks for 3-D body-centered control of position- and size-invariant planned arm movement sequences and tool use. In preparation.

Bullock, D. and Grossberg, S. (1988a). Neural dynamics of planned arm movements: Emergent invariants and speed-accuracy properties during trajectory formation. *Psychological Review*, **95**, 49-90.

Bullock, D. and Grossberg, S. (1988b). The VITE model: A neural command circuit for generating arm and articulatory trajectories. In J.A.S. Kelso, A.J. Mandell, and M.F. Shlesinger (Eds.), **Dynamic patterns in complex systems.** Singapore: World Scientific Publishers.

Bullock, D. and Grossberg, S. (1989). VITE and FLETE: neural modules for trajectory formation and postural control. In W.A. Hershberger (Ed.), **Volitional Action.** Amsterdam: North-Holland-Elsevier.

Bullock, D. and Grossberg, S. (1990). Adaptive neural networks for control of movement trajectories invariant under speed and force rescaling. *Human Movement Science*, **9**, in press.

Bushnell, E.W. (1985). The decline of visually guided reaching during infancy. *Infant Behavior and Development*, **8**, 139-155.

Caminiti, R., Johnson, P.B., and Urbano, A. (1990). Making arm movements within different parts of space: Dynamic aspects in the primate motor cortex. *Journal of Neuroscience*, **10**, 2039-2058.

Carpenter, G.A. and Grossberg, S. (1981). Adaptation and trasnsmitter gating in vertebrate photoreceptors. *Journal of Theoretical Neurobiology*, **1**, 1-42.

Carpenter, G.A. and Grossberg, S. (1983). A neural theory of circadian rhythms: The gated pacemaker. *Biological Cybernetics*, **48**, 35-59.

Carpenter, G.A. and Grossberg, S. (1984). A neural theory of circadian rhythms: Aschoff's rule in diurnal and nocturnal mammals. *American Journal of Physiology (Regulatory, Integrative, and Comparative Physiology)*, **247**, R1067-R1082.

Carpenter, G.A. and Grossberg, S. (1985). A neural theory of circadian rhythms: Split rhythms, after-effects, and motivational interactions. *Journal of Theoretical Biology*, **113**, 163-223.

Carpenter, G.A. and Grossberg, S. (1987a). A massively parallel architecture for a self-organizing neural pattern recognition machine. *Computer Vision, Graphics, and Image Processing*, **37**, 54-115.

Carpenter, G.A. and Grossberg, S. (1987b). ART 2: Stable self-organization of pattern recognition codes for analog input patterns. *Applied Optics*, **26**, 4919-4930.

Carpenter, G.A. and Grossberg, S. (1988). The ART of adaptive pattern recognition by a self-organizing neural network. *Computer*, **21**, 77-88.

Carpenter, G.A. and Grossberg, S. (1990). ART 3: hierarchical search using chemical transmitters in self-organizing pattern recognition architectures. *Neural Networks*, **3**, 129-152.

Fry, D.B. (1966). The development of the phonological system in the normal and the deaf child. In F. Smith and G.A. Miller (Eds.), **The genesis of language: A psycholinguistics approach.** Cambridge, MA: MIT Press, pp.187-206.

Fujita, M. (1982a). Adaptive filter model of the cerebellum. *Biological Cybernetics*, **45**, 195-206.

Fujita, M. (1982b). Simulation of adaptive modification of the vestibulo-ocular reflex with an adaptive filter model of the cerebellum. *Biological Cybernetics*, **45**, 207-214.

Gaudiano, P. and Grossberg, S. (1990a). A Self-Regulating Endogenous Generator of Sample-and-Hold Random Training Vectors. In M. Caudill (Ed.) **International Joint Conference on Neural Networks. Vol. II** Hillsdale, NJ: Earlbaum. pp. 213-216.

Gaudiano, P. and Grossberg, S. (1990b). Adaptive Trajectory Control Using Vector Associative Maps. **Proceedings of the International Conference on Neural Networks for Automatic Target Recognition**. Tyngsboro, MA: Wang Institute of Boston University.

Georgopoulos, A.P., Kalaska, J.F., Caminiti, R., and Massey, J.T. (1982). On the relations between the direction of two-dimensional arm movements and cell discharge in primate motor cortex. *Journal of Neuroscience*, **2**, 1527-1537.

Georgopoulos, A.P., Kalaska, J.F., Crutcher, M.D., Caminiti, R., and Massey, J.T. (1984). The representation of movement direction in the motor cortex: Single cell and population studies. In G.M. Edelman, W.E. Goll, W.M. Cowan (Eds.), **Dynamic aspects of neurocortical function**. Neurosciences Research Foundation, 501-524.

Georgopoulos, A.P., Schwartz, A.B., and Kettner, R.E. (1986). Neural population coding of movement direction. *Science*, **233**, 1416-1419.

Gnadt, J.W. and Andersen, R.A. (1988). Memory related motor planning activity in posterior parietal cortex of macaque. *Experimental Brain Research*, **70**, 216-220.

Grossberg, S. (1964). **The theory of embedding fields with applications to psychology and neurophysiology**. New York: Rockefeller Institute for Medical Research.

Grossberg, S. (1969). On learning of spatiotemporal patterns by networks with ordered sensory and motor components, I: Excitatory components of the cerebellum. *Studies in Applied Mathematics*, **48**, 105-132.

Grossberg, S. (1972a). A neural theory of punishment and avoidance, II. Quantitative theory. *Mathematical Biosciences*, **15**, 39-67.

Grossberg, S. (1972b). Neural expectation: Cerebellar and retinal analogs of cells fired by learnable or unlearned pattern classes. *Kybernetik*, **10**, 49-57.

Grossberg, S. (1973). Contour enhancement, short-term memory, and constancies in reverberating neural networks. *Studies in Applied Mathematics*, **52**, 217-257.

Grossberg, S. (1976). Adaptive pattern classification and universal recoding, I: Parallel development and coding of neural feature detectors, *Biological Cybernetics*, **23**, 121-134.

Grossberg, S. (1978). A theory of human memory: Self-organization and performance of sensory-motor codes, maps, and plans. In R. Rosen and F. Snell (Eds.), **Progress in theoretical biology, Vol. 5**. New York: Academic Press, 233-374.

Grossberg, S. (1982). **Studies of mind and brain: Neural principles of learning, perception, development, cognition, and motor control.** Boston: Reidel Press.

Grossberg, S. (1984). Some normal and abnormal behavioral syndromes due to transmitter gating of opponent processes. *Biological Psychiatry*, **19**, 1075-1118.

Grossberg, S. (1987a). **The adaptive brain I: Cognition, learning, reinforcement, and rhythm.** Amsterdam: Elsevier/North-Holland.

Grossberg, S. (1987b). **The adaptive brain II: Vision, speech, language, and motor control** Amsterdam: Elsevier/North-Holland.

Grossberg, S. (1988). Nonlinear neural networks: Principles, mechanisms, and architectures. *Neural Networks*, **1**, 17-61.

Grossberg, S. (1990a). Self-Organizing Neural Architectures for Motion Perception, Adaptive Sensory-Motor Control, and Associative Mapping. In M. Caudill (Ed.) **International Joint Conference on Neural Networks. Vol. II** Hillsdale, NJ: Earlbaum. pp. 26-29.

Grossberg, S. (1990b). Why do parallel cortical systems exist for the processing of static form and moving form? *Perception and Psychophysics*, in press.

Grossberg, S. and Gutowski, W. (1987). Neural dynamics of decision making under risk: Affective balance and cognitive-emotional interactions. *Psychological Review*, **94**, 300-318.

Grossberg S., and Kuperstein, M. (1986). **Neural dynamics of adaptive sensory-motor control.** Amsterdam: Elsevier/North-Holland.

Grossberg S., and Kuperstein, M. (1989). **Neural dynamics of adaptive sensory-motor control: Expanded edition.** Elmsford, NY: Pergamon Press.

Grossberg, S. and Mingolla, E. (1985). Neural dynamics of perceptual grouping: Textures, boundaries, and emergent segmentations. *Perception and Psychophysics*, **38**, 141-171.

Grossberg, S. and Rudd, M.E. (1990). Cortical dynamics of visual motion perception: Short-range and long-range apparent motion. Submitted for publication.

Grossberg, S. and Schmajuk, N.A. (1987). Neural dynamics of attentionally-modulated Pavlovian conditioning: Conditioned reinforcement, inhibition, and opponent processing. *Psychobiology*, **15**, 195-240.

Grossberg, S. and Schmajuk, N.A. (1989). Neural dynamics of adaptive timing and temporal discrimination during associative learning. *Neural Networks*, **2**, 79-102.

Hindmarsh, A.C. (1983). Odepack, a systematized collection of ode solvers. In **Scientific computing**, R. S. Stepleman *et al.* (Eds.). Amsterdam:North-Holland, pp. 55-64.

Houk, J.C., Singh, S.P., Fischer, C., and Barto, A.G. (1989). In W.T. Miller, R.S. Sutton and P.J. Werbos (Eds.), **Neural networks for control**. Cambridge, MA: MIT Press.

Ito, M. (1974). The control mechanism of cerebellar motor systems. In F.O. Schmidt and F.G. Worden (Eds.), **The neurosciences third study program**. Cambridge, MA: MIT Press.

Ito, M. (1984). **The cerebellum and neural control**. New York: Raven Press.

Kalaska, J.F., Cohen, D.A.D., Hyde, M.L., and Prud'homme, M. (1990). A comparison of movement direction-related versus load direction-related activity in primate motor cortex, using a two-dimensional reaching task. *The Journal of Neuroscience*, **9**, 2080-2102.

Kandel, E.R. and Schwartz, J.H., Eds. (1985). **Principles of neural science**. Second Edition. New York:Elsevier.

Kohonen, T. (1983). Representation of information in spatial maps which are produced by self-organization. In E. Basar, H. Flohr, H. Haken, and A.J. Mandell (Eds.), **Synergetics of the brain**. New York: Springer-Verlag.

Kohonen, T. (1984). **Self-organization and associative memory**. New York: Springer-Verlag.

Lai, Y.Y. and Siegel, J.M. (1990). Muscle tone suppression and stepping produced by stimulation of Midbrain and Rostral Pontine Reticular Formation. *Journal of Neuroscience*, **10** (8), 2727-2734.

Marr, D. (1969). A theory of cerebellar cortex. *Journal of Physiology (London)*, **202**, 437-470.

Mays, L.E. and Sparks, D.L. (1980). Dissociation of visual and saccade-related responses in superior colliculus neurons. *Journal of Neurophysiology*, **43**, 207-232.

Miller, J.P. and Selverston, A.I. (1982a). Mechanisms underlying pattern generation in lobster stomatogastric ganglion as determined by selective inactivation of identified neurons. II. Oscillatory properties of pyloric neurons. *Journal of Neurophysiology*, **48**, 1378-1391.

Miller, J.P. and Selverston, A.I. (1982b). Mechanisms underlying pattern generation in lobster stomatogastric ganglion as determined by selective inactivation of identified neurons. IV. Network properties of the pyloric system. *Journal of Neurophysiology*, **48**, 1416-1432.

Petzold, L.R. (1983). Automatic selection of methods for solving stiff and and nonstiff systems of ordinary differential equations, *SIAM J. Sci. Stat. Comput.*, **4**, pp. 136-148.

Piaget, J. (1963). **The origins of intelligence in children.** New York: Norton. **95**, 49-90.

Robertson, S.S. (1985). Cyclic motor activity in the human fetus after midgestation. *Developmental Psychobiology*, **18**, 411-419.

Ryall, R.W. (1970). Renshaw cell mediated inhibition of Renshaw cells: Patterns of excitation and inhibition from impulses in motor axon collaterals. *Journal of Neurophysiology*, **33**, 257-270.

Selverston, A.I. (1988). A consideration of invertebrate central pattern generators as computational data bases. *Neural Networks*, **1**, 109-117.

Selverston, A.I. and Moulins, M., Editors (1987). **The crustacean stomatogastric system.** Berlin:Springer-Verlag.

Sigvardt, K.A., and Mulloney, B. (1982). Properties of synapses made by IVN command-interneurones in the stomatogastric ganglion of the spiny lobster *Panulirus Interruptus. Journal of Experimental Biology.* **97**, 153-168.

Simon, H.A. (1969). **The Sciences of the Artificial.** Cambridge, MA:MIT Press.

Singer, W. (1985). Central control of developmental plasticity in the mammalian visual cortex. *Vision Research*, **25**, 389-396.

Soechting, J.F. and Flanders, M. (1989). Errors in pointing are due to approximations in sensorimotor transformations. *Journal of Neurophysiology*, **62**, 595-608.

Wachtel, H. and Kandel, E.R. (1971). Conversion of synaptic excitation to inhibition at a dual chemical synapse. *Journal of Neurophysiology*, **34**, 56-68.

Appendix

The ERG presented here is a specialized gated dipole (Grossberg, 1972, 1982, 1984). In its simplest form, the gated dipole is a neural network that utilizes opponent processing between chemically-gated channels in such a way that sudden offset of an input signal to one channel causes a transient antagonistic rebound in the opponent channel (Figure 7).

The simplest feed-forward gated dipole obeys an equation identical to equation (12), but the transmitter depletion law is a linear function of the incoming signal X; that is,

$$\frac{dY^+}{dt} = \kappa(\lambda - Y^+) - h(X^+)Y^+, \tag{A1}$$

where $h(X) = \xi X$. The net signal through the gate (X^+Y^+) at steady state is a monotone increasing function of the input signal:

$$X^+Y^+ = X^+\frac{\kappa\lambda}{\kappa + \xi X^+}. \tag{A2}$$

In the present application, we require a circuit whose output oscillates between two opponent states. This cyclic behavior should be autonomous, i.e., it should not require an external "supervisor" to turn the differential input on and off. Hence the simple gated dipole is modified so that a constant differential input to the ON channel leads to a transient ON response, followed by an OFF response. This can be achieved if the net signal (A2) through the gate is an inverted-U function of the input signal. Neurons with inverted-U transfer functions have been found in a number of physiological preparations (e.g., Wachtel and Kandel, 1967), including some involving rhythm generators (Sigvardt and Mulloney, 1982). The mechanisms that give rise to such a nonmonotonic response can be pre- or post-synaptic.

In our application, we simulate an inverted-U transfer function through a pre-synaptic nonlinearity that affords a simple mathematical analysis. Let the transmitter gate obey equation (A1), but with

$$h(X) = \nu X^2 + \xi X. \tag{A3}$$

Let $\xi = 0$ for simplicity. Then equation (A2) can be vrewritten as:

$$X^+Y^+ = X^+\frac{\kappa\lambda}{\kappa + \nu(X^+)^2} \qquad (A4)$$

which is an inverted-U function of X^+. The ON channel output of the ERG equals the half-wave rectified difference of the signal through the two gates:

$$O^+ = \left[X^+Y^+ - X^-Y^-\right]^R, \qquad (A5)$$

which is positive at steady state if and only if:

$$\frac{\kappa\lambda X^+}{\kappa + \nu(X^+)^2} > \frac{\kappa\lambda X^-}{\kappa + \nu(X^-)^2}. \qquad (A6)$$

Let $X^+ = X^- + \Delta X$. Then equation (A6) can be factored and rewritten as:

$$O^+ = \frac{\kappa\lambda\Delta X(\kappa - \nu X^+X^-)}{(\kappa + \nu X^{+2})(\kappa + \nu X^{-2})}. \qquad (A7)$$

This equation shows that the ON channel will be active at equilibrium if $X^+X^- < \kappa/\nu$, and the OFF channel will be active otherwise. Parameter selection such that $X^+X^- > \kappa/\nu$ leads to a transient positive ON response while the transmitter Y^+ is being depleted, which habituates to a net response in the OFF channel.

The nonlinear law (A1) and (A3) does not affect other important properties of the gated dipole, such as the generation of a rebound in response to gated input offset. These results also hold for other faster-than-linear transmitter laws; equation (A3) was used only for its mathematical simplicity.

Figure Captions

Figure 1: A schematic diagram of the Adaptive VITE (AVITE) circuit. See Section 3 for details of TPC, DV, PPC, and GO populations. The Now Print (NP) gate copies the PPC into the TPC when the arm is stationary, and the plastic synapses (semicircles in the TPC→DV pathways) learn to transform target commands into correctly calibrated outflow signals at the PPC.

Figure 2: The VITE model, adapted from Bullock and Grossberg (1988a). TPC = Target Position Command, DV = Difference Vector, PPC = Present Position Command. The GO signal acts as a nonspecific multiplicative gate that can control the overall speed of a movement, or the will to move at all. Use of a single GO signal insures synchronous activation of all muscles in the synergies involved in a coordinated movement.

Figure 3: The Passive Update of Position (PUP) circuit, adapted from Bullock and Grossberg (1988a). DV and PPC are the same as in Figure 2. The adaptive pathway PPC→DV_p calibrates PPC outflow signals to match inflow signals during intervals of posture. DV output is gated to zero during passive arm movements, while the DV_p updates the PPC until it equals the new position. GO signal activation disables passive update to allow discrimination between voluntary movements and movements caused by external forces.

Figure 4: A diagrammatic illustration of a single babbling cycle in the AVITE. (a) The Endogenous Random Generator ON channel output (ERG ON) is integrated at the PPC, giving rise to random outflow signals that move the arm. (b) When the arm stops moving at ERG ON offset, a complementary ERG OFF signal opens the Now Print (NP) gate, copying the current PPC into the TPC through an arbitrary transformation. (c) The filtered TPC activation is compared to the PPC at the DV stage. DV activation would be zero in a properly calibrated AVITE. (d) The learning law changes TPC→DV synapses to

eliminate any nonzero DV activation, thus learning the reverse of the PPC→NP→TPC transformation.

Figure 5: Schematic diagram of the AVITE circuit showing the existence of opponent channels for control of agonist-antagonist muscle pairs, indicated by ($^+$) and ($^-$) superscripts, respectively. Push-pull interactions at the TPC and PPC layers insure that contraction in one channel will result in relaxation of the opponent channel, and vice versa.

Figure 6: Schematic diagram of the Endogenous Random Generator (ERG). PG = Pauser Gate; J^+ = phasic input to the ON channel; I = tonic input to both channels; X^+,X^- = input layer activation; Y^+,Y^- = available chemical transmitter (chemical gates represented by rectangular striped synapses); O^+ = ERG ON output to the PPC; O^- = ERG OFF output controls PG activation. See text for description of ERG dynamics.

Figure 7: Schematic representation of linear, feed-forward gated dipole. Plots indicate response of each dipole stage over time. A sudden increase in phasic input (J^+, bottom left of figure) leads to a transient overshoot in the ON channel (top left), followed by habituation to a positive plateau. Removal of the differential input leads to a transient rebound in the OFF channel (top right) due to the depleted chemical transmitter in the ON channel gate.

Figure 8: Response of various ERG levels to a continuous differential input J^+. The inverted-U transfer function through the chemical gates (rectangular synapses) leads to a transient ON response (O^+), followed by activation of the OFF channel (O^-). Sufficient OFF channel activation energizes the Pauser Gate (PG), which shuts off phasic input J^+ to the ON channel, causing a larger, transient rebound in the OFF channel. Removal of the phasic input allows ON channel transmitter Y^+ to replenish, eventually shutting off the PG and starting a new cycle. The ON channel output is choppy due to noisiness

of phasic input J^+. Dashed lines in upper right-hand plot represent PG activation (not drawn to scale).

Figure 9: Diagram of the complete ERG-AVITE system used for the two-joint simulations. Each AVITE agonist-antagonist module is driven by two ERG modules. AVITE outflow commands control movement of a simulated two-joint arm. The GO signal, NP gate, and PG are the same for all modules to ensure synchronous movement and learning for both synergies.

Figure 10: Pictorial representation of ERG-AVITE simulations. Each grid represents the configuration of the simulated arm during a quiet phase (ERG OFF is active). Note the diversity of attained positions.

Figure 11: Simulation results under the standard ERG parameters: $I = 0.05$, $\mu_J = 0.05$, $\sigma_J = 1.0$, $\pi_J = 1$, $\zeta = 0.1$, $\eta = 1.0$, $\kappa = 0.1$, $\lambda = 7.5$, $\nu = 0.5$, $\xi = 0.0$, and $\theta_P = 0.08$. GO signal is off during all babbling runs ($G = 0.0$). **(a)** the time course behavior of four state variables in the ON (left) and OFF (right) ERG channels during 2,000 steps of the simulation. The range of each plot is indicated in parentheses under the abscissa. From top to bottom: ERG outputs (O^+,O^-), available transmitter (Y^+, Y^-), input layer activation (X^+, X^-), and total input signal ($I + J^+, I$). Note that bottom three plots for OFF channel (right) are always constant. This is due to lack of phasic input to OFF channel. However, baseline activation is necessary to energize OFF channel rebounds (top right plot). **(b)** Distribution of joint angles (between $-\pi$ and π radians) attained during about 400 babbled movements (100,000 steps of the simulation). Left: each dot in the scatterplot represents the angle of the two joints (θ_1, θ_2) during each quiet phase. Center point represents resting position. Right: histograms of the distribution of joint angles around resting position. Magnitude histogram represents the number of dots falling within each of 16 evenly spaced concentric rings about the center; the unimodal distribution toward the left side of the histogram indicates a tendency for less extreme

joint angles. Phase histogram represents the number of dots at each of sixteen evenly spaced quadrants about the resting position; a flat phase histogram indicates a uniform distribution of joint angle combinations. (c) Representative sample of uninterrupted total input $I + J^+$ for 500 steps with the standard parameters. The PG threshold θ_P was raised ($\theta_P = 10.0$) to disable phasic input gating. The tonic input I causes the "shift" above zero.

Figure 12: This figure should be compared to Figure 11. The average noise level is raised to $\mu_J = 0.15$. The resulting ERG dynamics and overall distribution are virtually unchanged from those obtained with standard parameters.

Figure 13: This figure should be compared to Figure 11. The range of the phasic input J^+ was raised to $\sigma_J = 1.6$. Again, overall dynamics and joint angle distribution are virtually unchanged.

Figure 14: This figure should be compared to Figure 11. Here the average period of the noise was raised to $\pi_J = 4$ (see text). As a result, the phasic input J^+ is much more sparse, and the overall ERG dynamics are significantly affected. In spite of this, the overall distribution of joint angles is similar to that obtained with the standard parameters.

Figure 15: This figure should be compared to Figure 11. The tonic arousal level was raised to $I = 0.15$. As a result, the dynamics of the input layer X are dominated by the tonic input I, and the differential input J^+ becomes less effective. The ERG ON output bursts (O^+) are much smaller, resulting in much smaller joint angles during babbling. In contrast to the profound effect of changes in the arousal level I, a similar change in phasic input J^+ (Figure 12) has an insignificant effect on the overall joint angle distribution.

Figure 16: (a) and (b) should be compared to Figure 11. The input layer parameters ζ (decay rate) and η (integration rate) are both increased ($\zeta = 0.2, \eta = 1.5$). The steady-

state activation level given by equation (19) is approximately unchanged, but the faster response yields larger ON bursts (note that the ERG output O^+ is plotted in the range [0,2] instead of the usual [0,1]) that more closely follow input fluctuations, resulting in a slightly broader distribution of joint angles.

Figure 17: (a) and (b) should be compared to Figure 11. The maximum transmitter level was reduced to $\lambda = 5.0$, resulting in ERG ON bursts of smaller amplitude, and a correspondingly narrower distribution of joint angles.

Figure 18: (a) and (b) should be compared to Figure 11. The PG threshold θ_P is lowered by one order of magnitude ($\theta_P = 0.008$). The resulting ERG ON bursts are of the same amplitude and overall shape, but the length of the quiet phases has increased, giving rise to only six ERG ON bursts instead of the standard eight in 2,000 steps. (c) Plot of θ_P vs. number of ERG ON bursts (babbled movements) during 10,000 steps, showing dependence of average ERG periodicity on PG threshold θ_P.

Figure 19: Absolute value of the error in the agonist and antagonist DV, and total error $(|V^+| + |V^-|)$, measured shortly after onset of quiet phases. Note approximately exponential decay. Learning rate was slowed down to $\gamma = 0.001$ to illustrate smooth, slow error decay over 50,000 steps (approximately 200 babbled movements).

Figure 20: Each grid shows a visualization of two PPC agonist-antagonist pairs based on the transformation outlined in Section 14. In each part, the arm is started at rest ($P+ = P^- = 0.5$), two pairs of agonist-antagonist TPC values are selected (mapped as a black triangle on each grid), the GO signal is turned on ($G = 1.0$), and the PPC populations are allowed to integrate until they have equilibrated. Each part shows reaching performance after a certain number of babbling phases: (a) after about 40 babbled movements; (b) after about 80 movements; (c) after about 120 movements; (d) after about 160 movements; (e) after about 200 movements. Part (4) shows reaching after

about 200 movements (same as part (e)), but for a different target. The learning rate was set artificially slow ($\gamma = 0.001$) to illustrate gradual improvement in performance, and for direct comparison with Figures 19 and 27.

Figure 21: Diagram of the AVITE model with spatially-organized TPC. Different (P^+, P^-) pairs are mapped to activation of a distinct TPC node through a hard-wired DODOG transform (see text). Active TPC node samples current (V^+, V^-) pair, while learning to drive it to zero.

Figure 22: Numerical simulations of the DODOG transform. (a) Each curve represents the distribution of activations T_j (in the range [0.0,0.5]) for a particular PPC activation pair (P^+, P^-). (b) The ordinate shows the location j of maximal activation at the spatial TPC as P^+ is increased from 0 to 1. Location here is plotted as a smooth curve in the range [0,10], but can be adjusted to fit any size population. (c) Net activation level T_j at location of peak as P^+ is increased from 0 to 1, plotted in the range [0.0,0.5]. Parameters for the two DOGs are: $\phi = 2.0$, $\psi = 1.7$, $\chi = 4.5$, $\omega = 6.0$. Quasi-linear shift (dashed lines, Figure 22) is obtained with $j_0 = 4$, sigmoidal shift (solid lines) with $j_0 = 1$. To extend DODOG shift to 40 cells, all parameters would be multiplied by 4.

Figure 23: Synaptic strengths from each of 40 TPC nodes to the agonist (solid line, marked by '*') and antagonist (dashed line, marked by 'x') DV. Equal amplitude increments are transformed into equal spatial shifts (linear shift). The synapses have learned the correct reverse (linear) transformation. Synapses near the sides of the plot are zero (or near zero) because they correspond to unsampled extreme positions. Learning rate is $\gamma = 0.05$, and LTM decay is $\beta = 0.0001$.

Figure 24: (a) Plot of the sigmoidal transformation given by equation (28). (b) Synaptic strengths from each of 40 TPC nodes to the agonist (solid line, marked by '*') and antagonist (dashed line, marked by 'x'). Equal amplitude increments are trans-

formed into *unequal* spatial shifts, with a denser sampling of more central TPC positions (sigmoidal shift). The synapses can be seen to have learned the correct inverse sigmoid transformation. Learning rate is $\gamma = 0.05$, and LTM decay is $\beta = 0.0001$.

Figure 25: Same as Figure 24, but several TPC nodes are simultaneously activated. We let $f(T_j) = T_j$. Activation decays away from peak node T_{j^*} according to $T_j = 1.0/(\tau|j^* - j| + 1.0)$, where j^* is obtained from equation (27). This implies $T_{j^*} = 1.0$, and T_j decays geometrically with distance on either side of T_{j^*} at a rate dependent on τ. For this simulation we let $\tau = 1.0$, and allowed activation to spread to five nodes on either side of the peak. Asymptotic learning is almost identical to winner-take-all TPC simulation of Figure 24.

Figure 26: The effect of distributed TPC coding after 20,000 simulation steps. (a) winner-take-all TPC dynamics only allow learning for nodes that have been actively sampled, leaving a number of synapses at or near zero. (b) Activation is allowed to spread to two nodes on either side of the TPC peak ($\tau = 2.0$, see Figure 25), causing some learning at nearly all TPC positions. (c) Activation is allowed to spread to five nodes on either side of the TPC peak ($\tau = 1.0$), leading to a smoother approximation of the asymptotic reverse transformation (sigmoidal).

Figure 27: Absolute value of the error in the agonist and antagonist DV, and total error ($|V^+| + |V^-|$), measured shortly after onset of quiet phases. Error convergence rate is slightly faster than in the gated simulations of Figure 19, even though the same learning rate and LTM decay are used.

Figure 28: The Intermodal VAM is able to learn the transformation from a spatial TPC (TPC_s) to the motor TPC (TPC_m). Intramodal learning in the AVITE still relies on internal feedback through the NP gate. Intermodal VAM activation relies on visual feedback of arm position. Learning takes place during babbling as the visual system

faithfully tracks the moving hand.

Figure 29: The Intermodal VAM has learned the correct linear relationship between arm position (P^+, P^-) and its visual representation. The spatial population contains $N = 40$ nodes, and all learning and LTM decay rates are the same as in Figure 23. Intramodal AVITE learns much faster because intermodal learning requires sampling of many different positions.

Figure 30: The Multimodal VAM. Activation of the upper left map represents eye position, and that of the upper right map represents target position on the retina. Activation from these two maps contribute at the Multimodal VAM. A given shift in eye position can be canceled by an equal and opposite shift in retinal target position.

Figure 31: The LTM traces from each of the two spatial maps $(N = M = 40)$ to the Multimodal VAM. During each quite phase, the value of H was determined from equation (31), and a pair of cells i_E and j_R that satisfied equation (30) were allowed to sample the intermodal DV activations. Because of cooperation between the two maps, the correct linear transformation is learned, but each synaptic weight becomes half as large as the ones shown in Figure 29, even though all parameters are the same. Note that because of the fast learning rate, the LTM traces from each sampled (i_E, j_R) pair could reach equilibrium within the first few simulation steps of each quiet phase. Hence, to expedite the simulation, we allowed a different random (i_E, j_R) pair to be selected at every time step during each quiet phase, although the same results can be obtained by allowing a smaller number of samples—in particular, one sample—in each quiet phase.

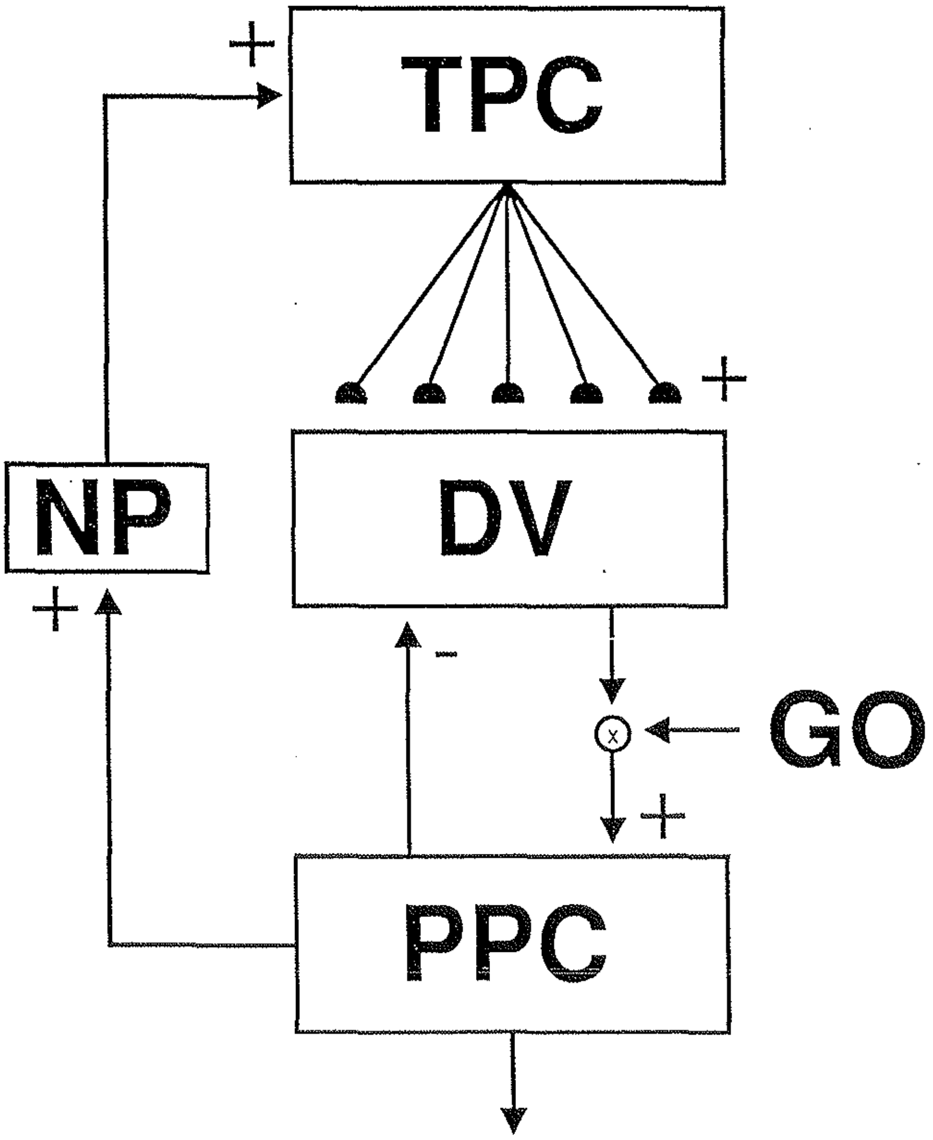

Figure 1

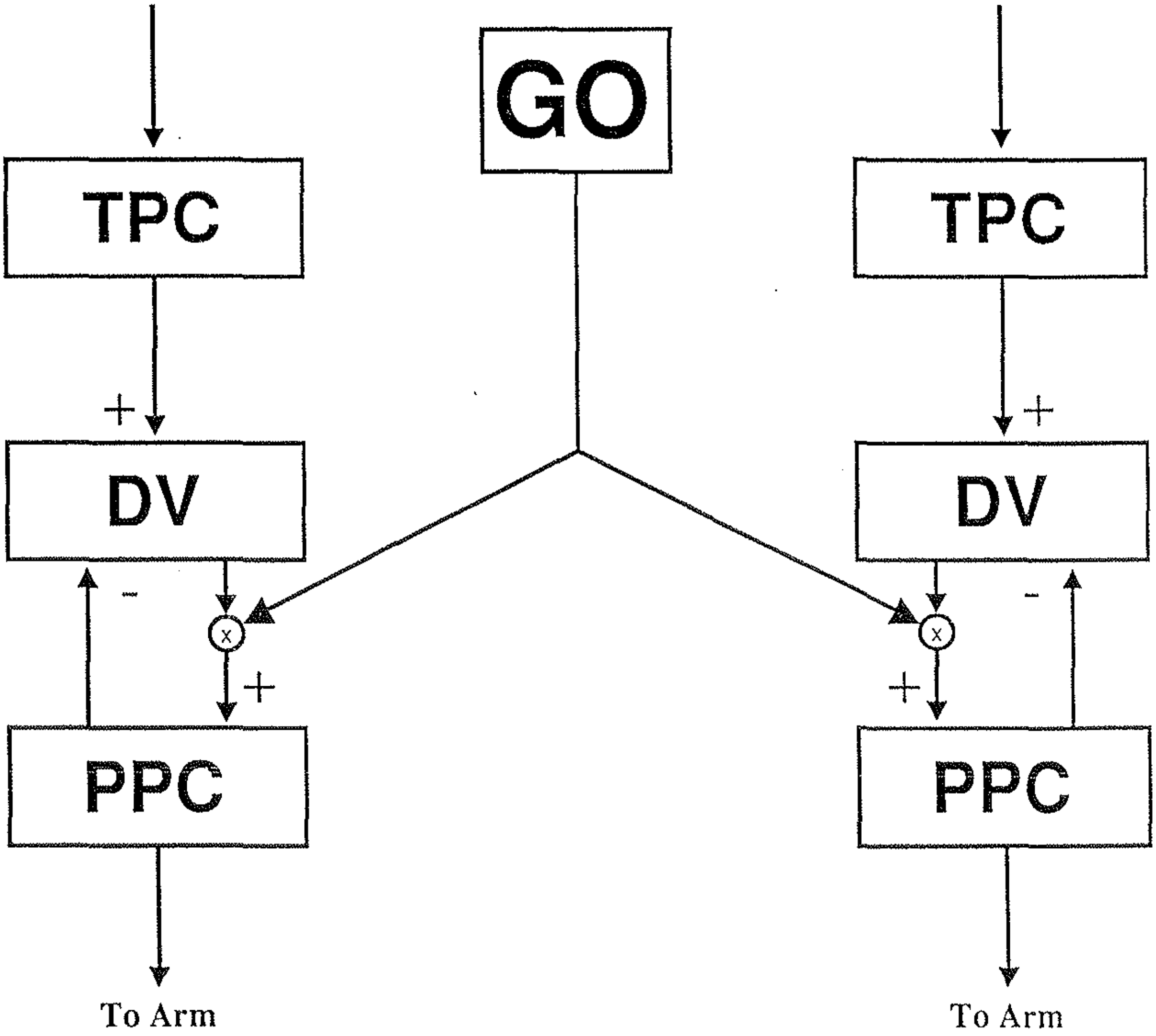

Figure 2

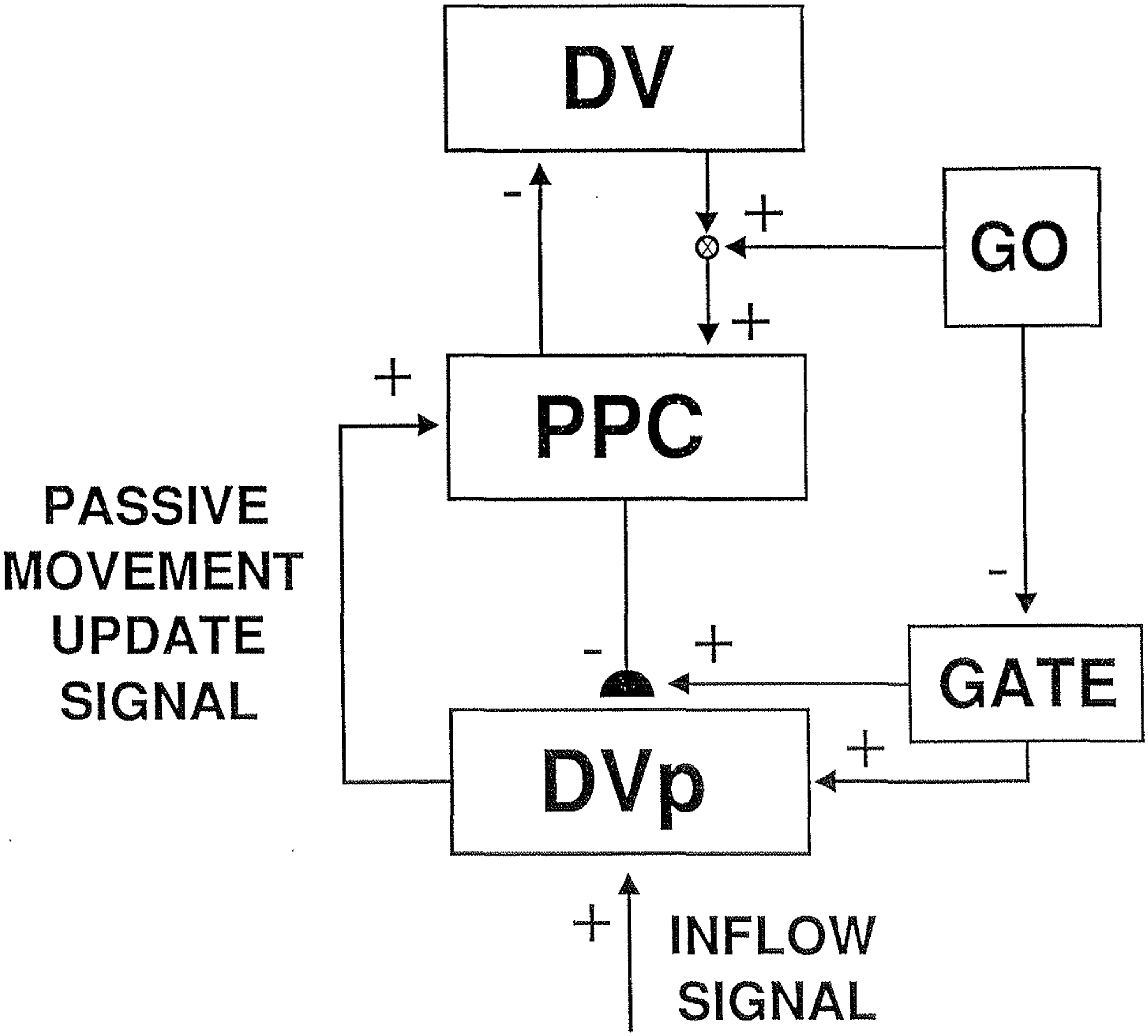
DV
GO
PPC
GATE
DVp
PASSIVE MOVEMENT UPDATE SIGNAL
INFLOW SIGNAL
+
-

Figure 3

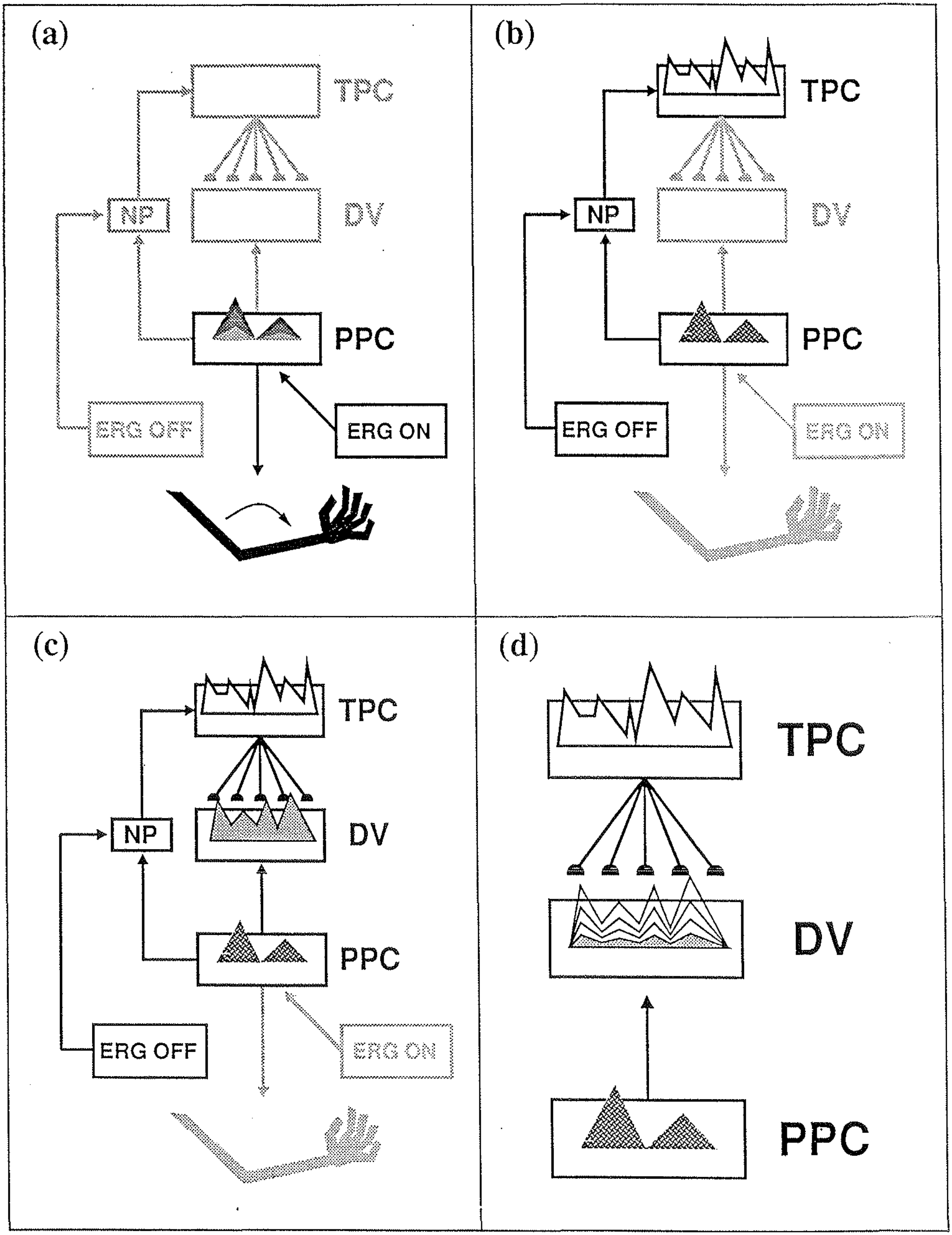
(a)
TPC
NP
DV
PPC
ERG OFF
ERG ON
(b)
TPC
NP
DV
PPC
ERG OFF
ERG ON
(c)
TPC
NP
DV
PPC
ERG OFF
ERG ON
(d)
TPC
DV
PPC

Figure 4

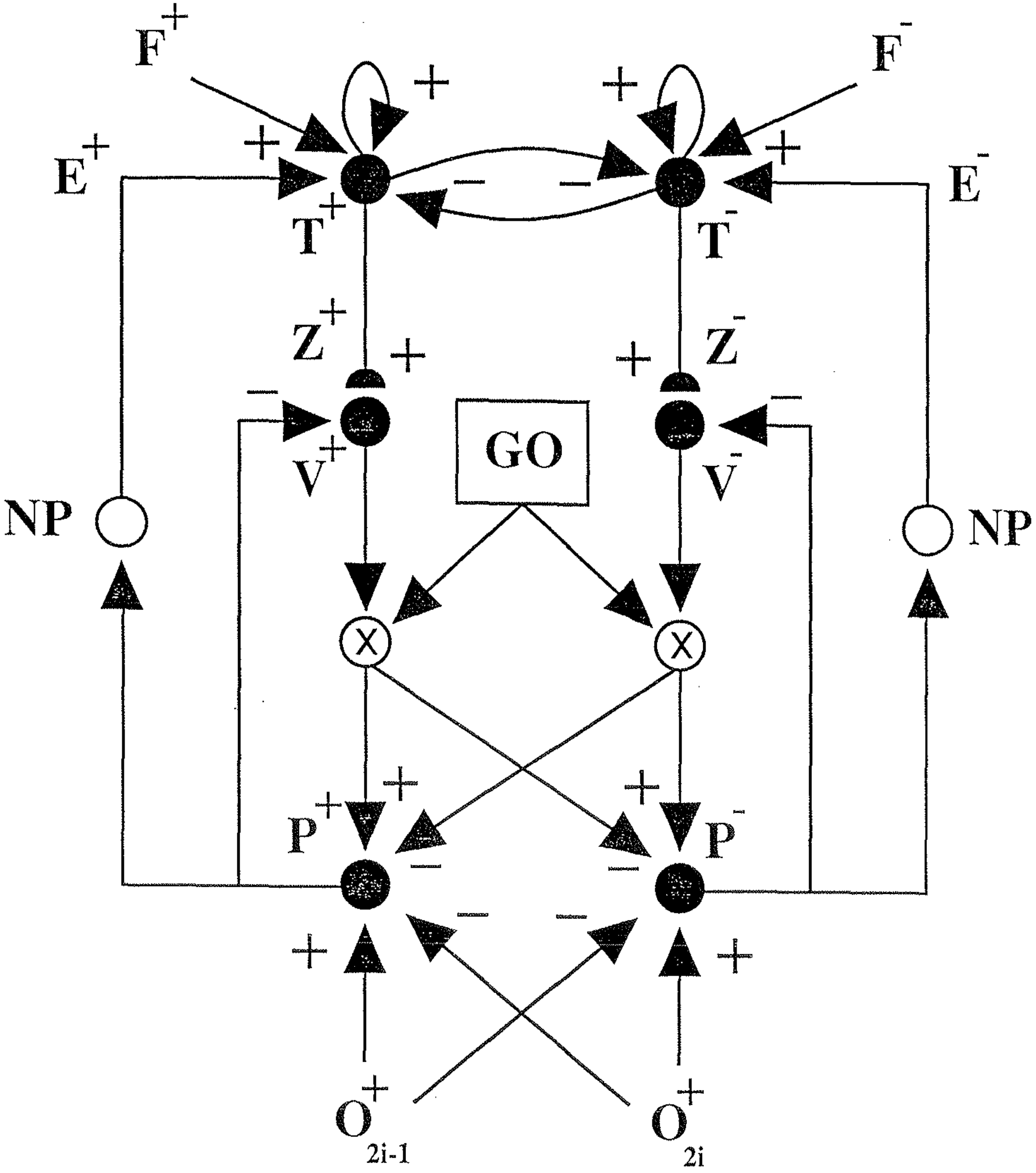

Figure 5

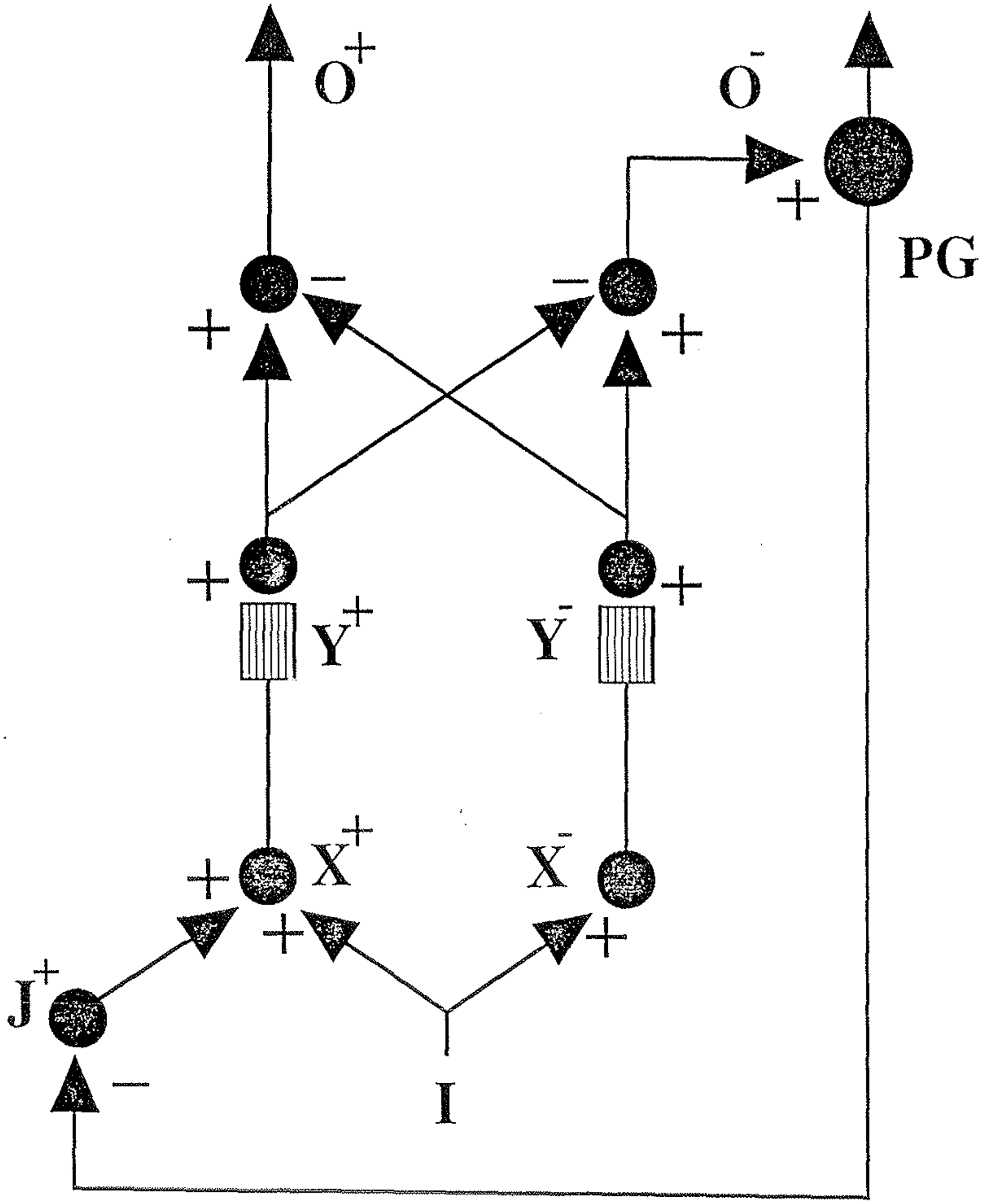

Figure 6

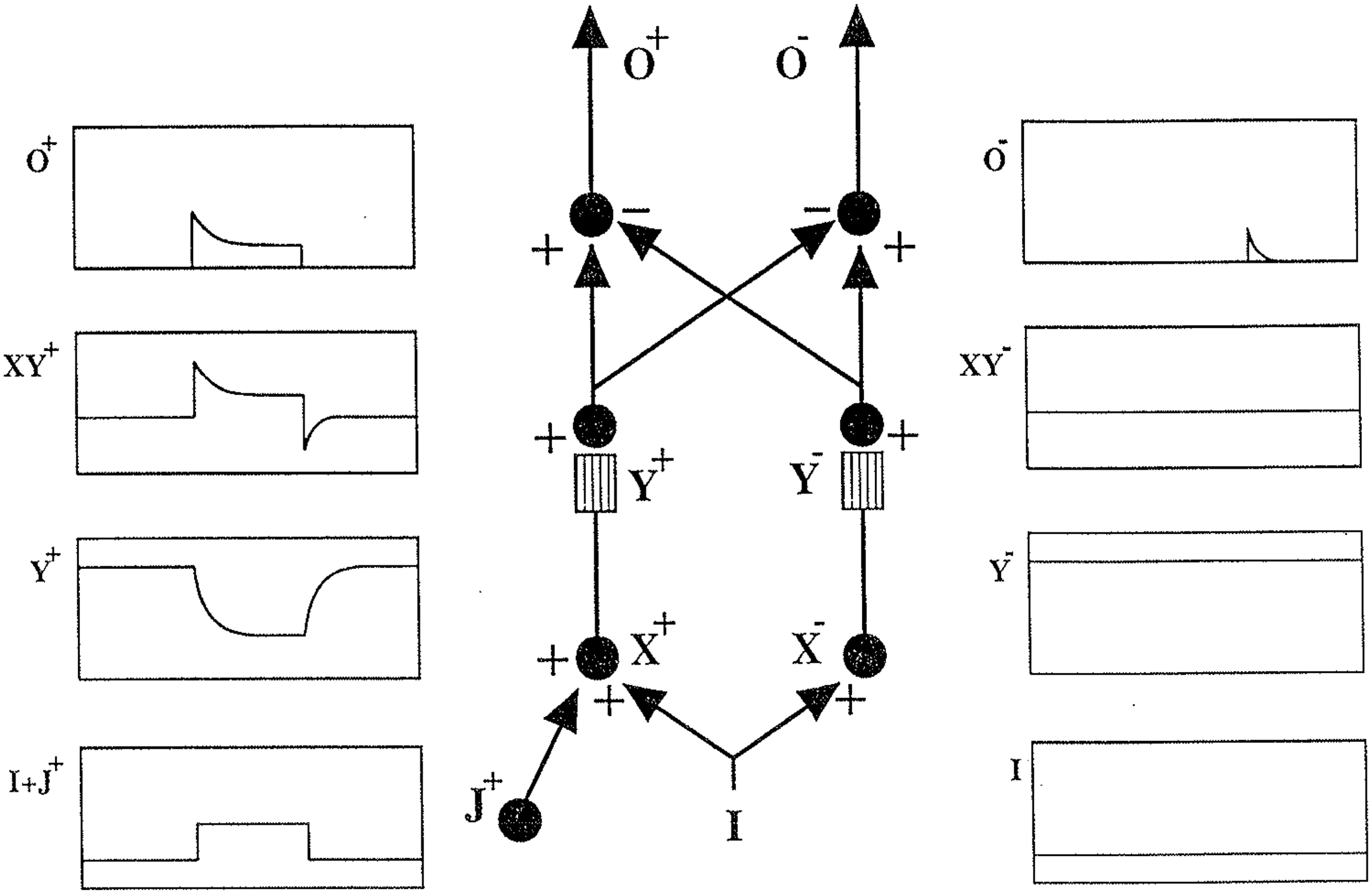

Figure 7

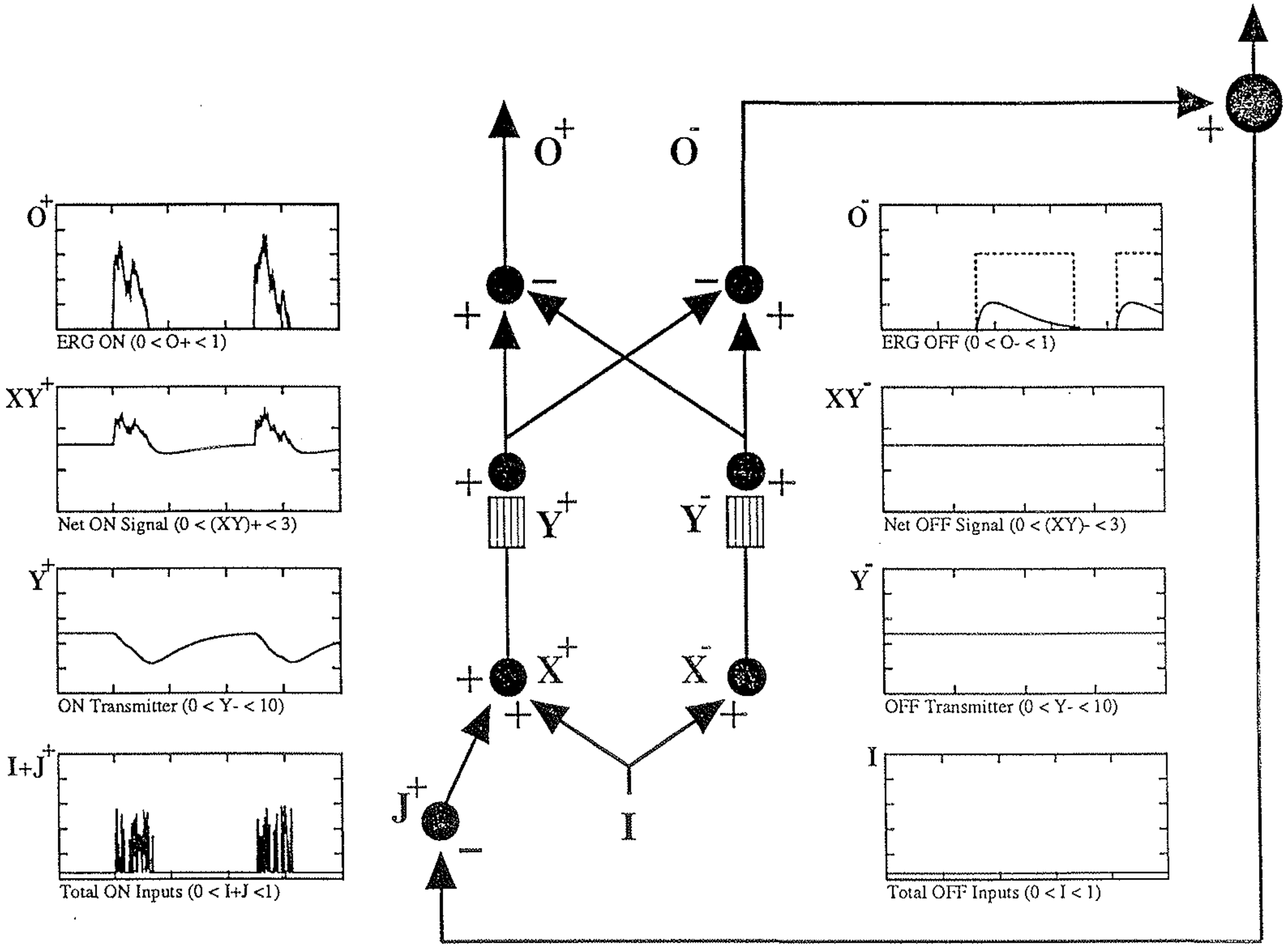
O+
O−
+
−
Y+
Y−
X+
X−
J+
I
O+
ERG ON (0 < O+ < 1)
XY+
Net ON Signal (0 < (XY)+ < 3)
Y+
ON Transmitter (0 < Y- < 10)
I+J+
Total ON Inputs (0 < I+J <1)
O−
ERG OFF (0 < O- < 1)
XY−
Net OFF Signal (0 < (XY)- < 3)
Y−
OFF Transmitter (0 < Y- < 10)
I
Total OFF Inputs (0 < I < 1)

Figure 8

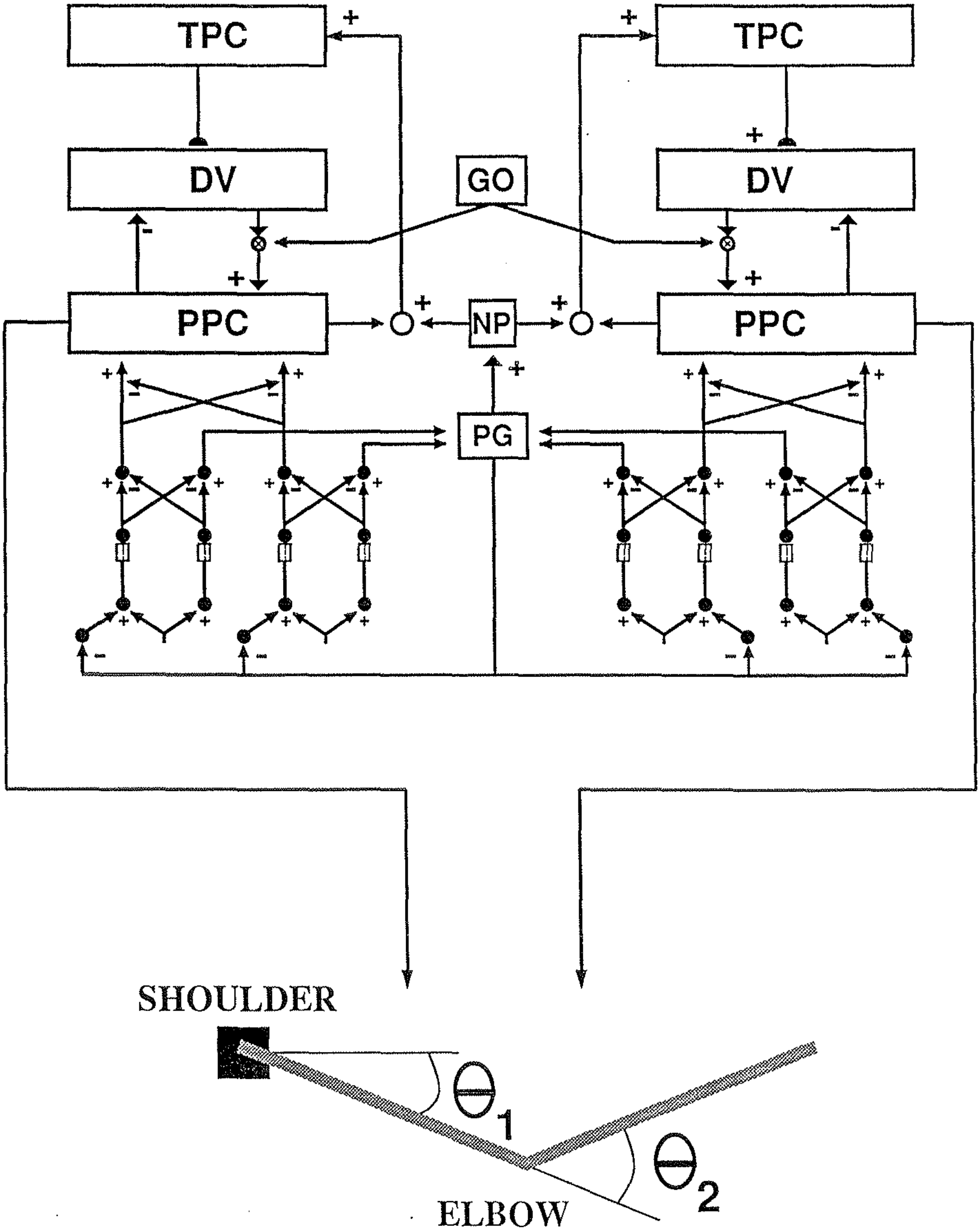

Figure 9

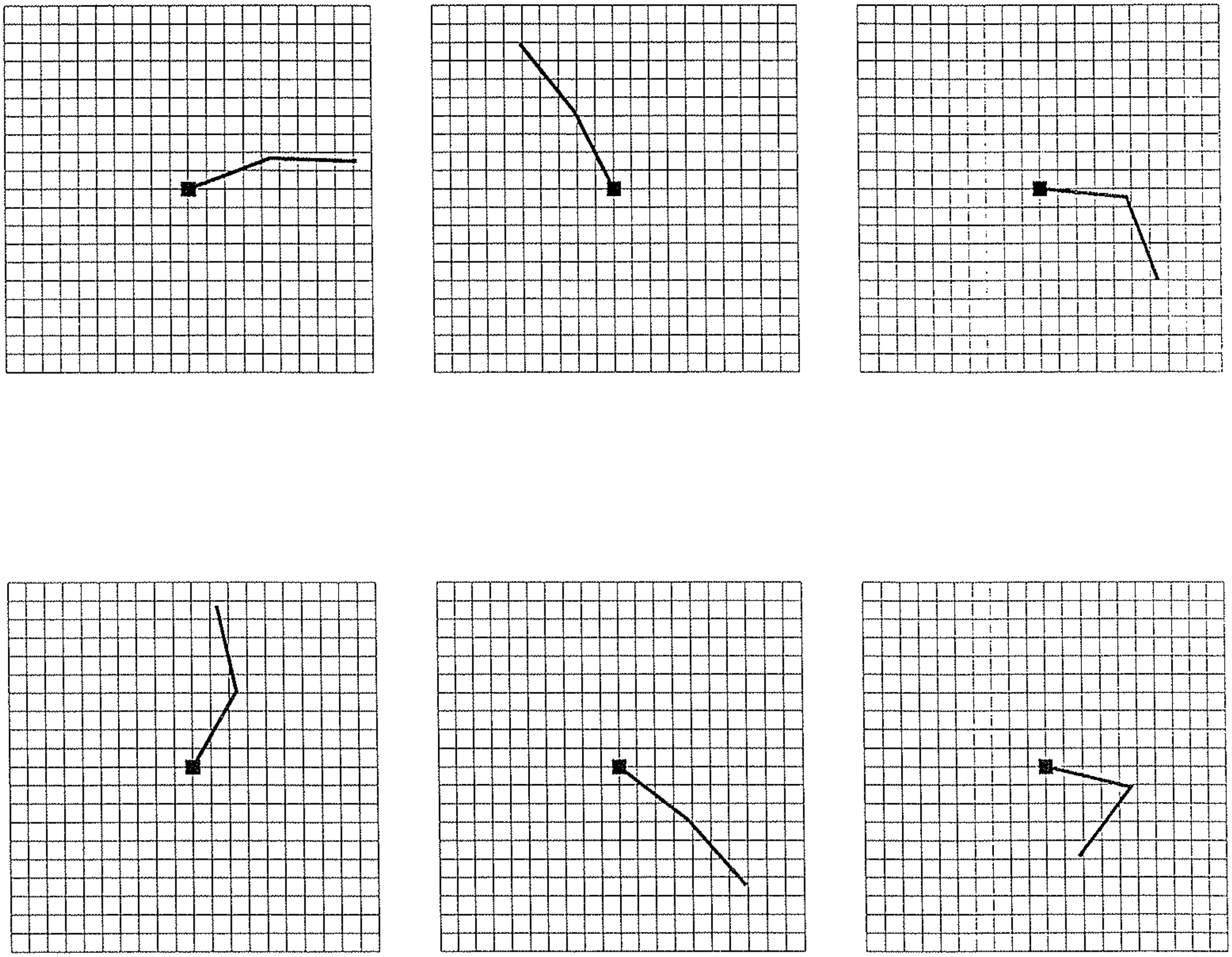

Figure 10

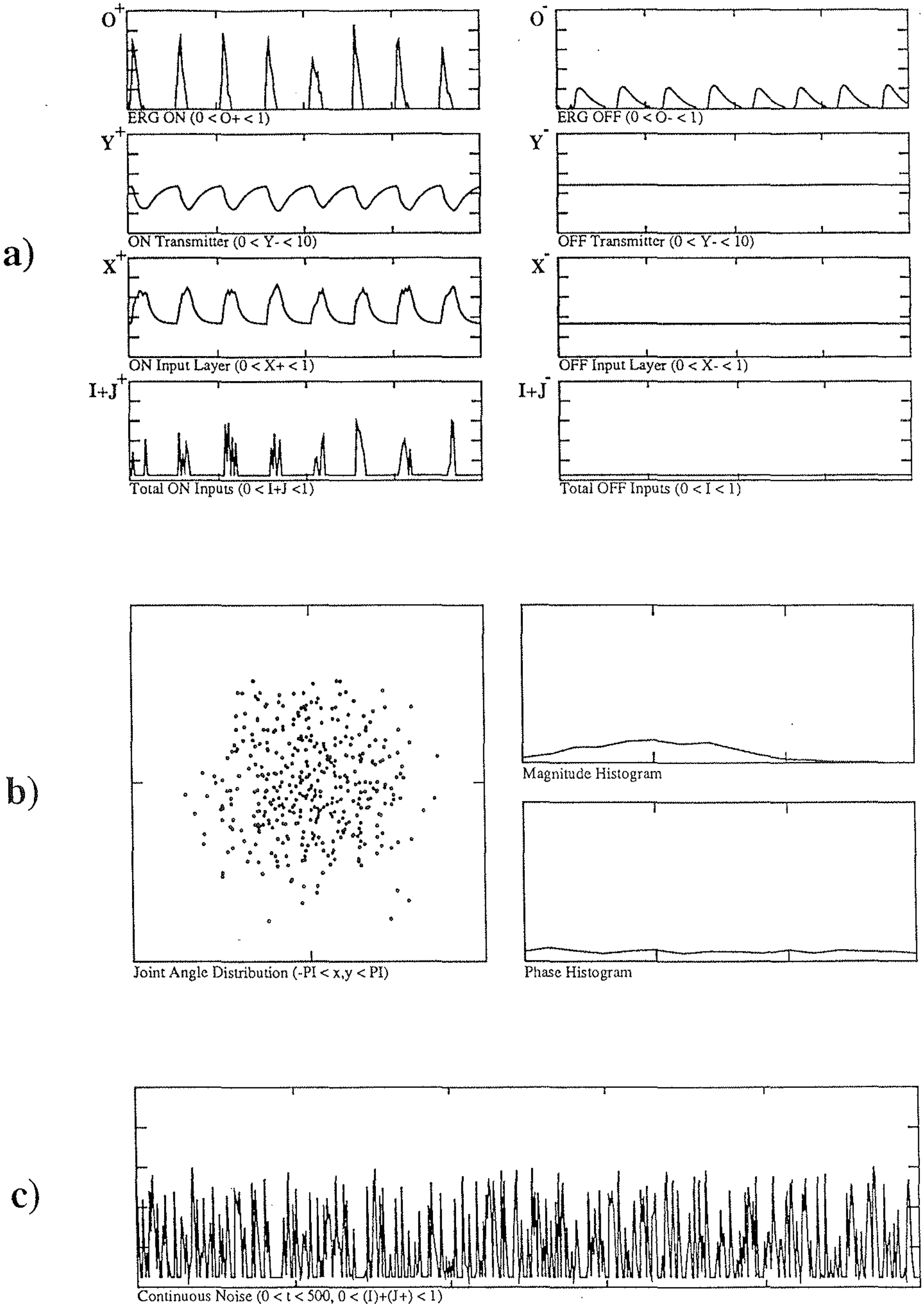
a)
O+
ERG ON (0 < O+ < 1)
O-
ERG OFF (0 < O- < 1)
Y+
ON Transmitter (0 < Y- < 10)
Y-
OFF Transmitter (0 < Y- < 10)
X+
ON Input Layer (0 < X+ < 1)
X-
OFF Input Layer (0 < X- < 1)
I+J+
Total ON Inputs (0 < I+J <1)
I+J-
Total OFF Inputs (0 < I < 1)
b)
Joint Angle Distribution (-PI < x,y < PI)
Magnitude Histogram
Phase Histogram
c)
Continuous Noise (0 < t < 500, 0 < (I)+(J+) < 1)

Figure 11

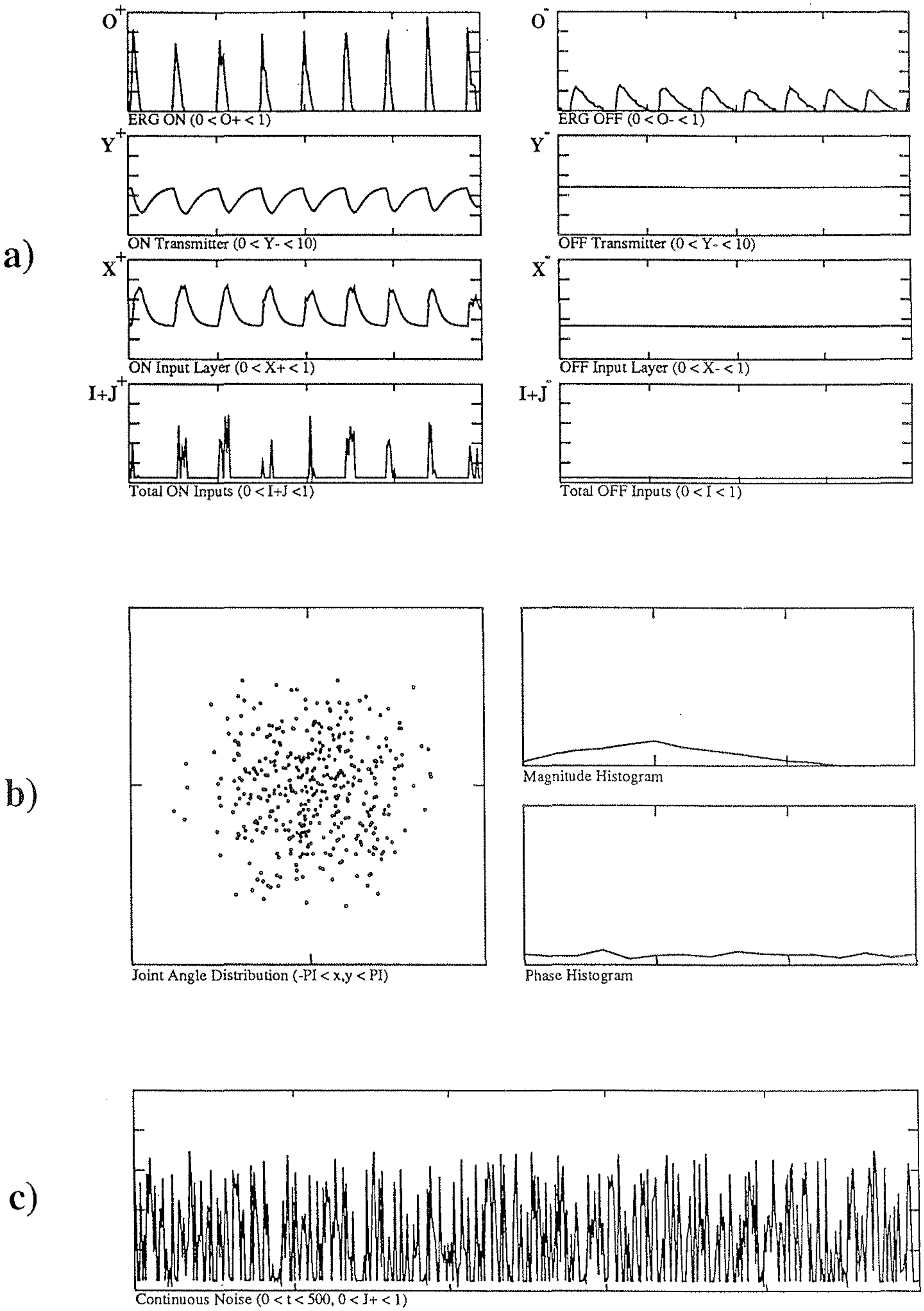
a)
O+
ERG ON (0 < O+ < 1)
O-
ERG OFF (0 < O- < 1)
Y+
ON Transmitter (0 < Y- < 10)
Y-
OFF Transmitter (0 < Y- < 10)
X+
ON Input Layer (0 < X+ < 1)
X-
OFF Input Layer (0 < X- < 1)
I+J+
Total ON Inputs (0 < I+J <1)
I+J-
Total OFF Inputs (0 < I < 1)
b)
Joint Angle Distribution (-PI < x,y < PI)
Magnitude Histogram
Phase Histogram
c)
Continuous Noise (0 < t < 500, 0 < J+ < 1)

Figure 12

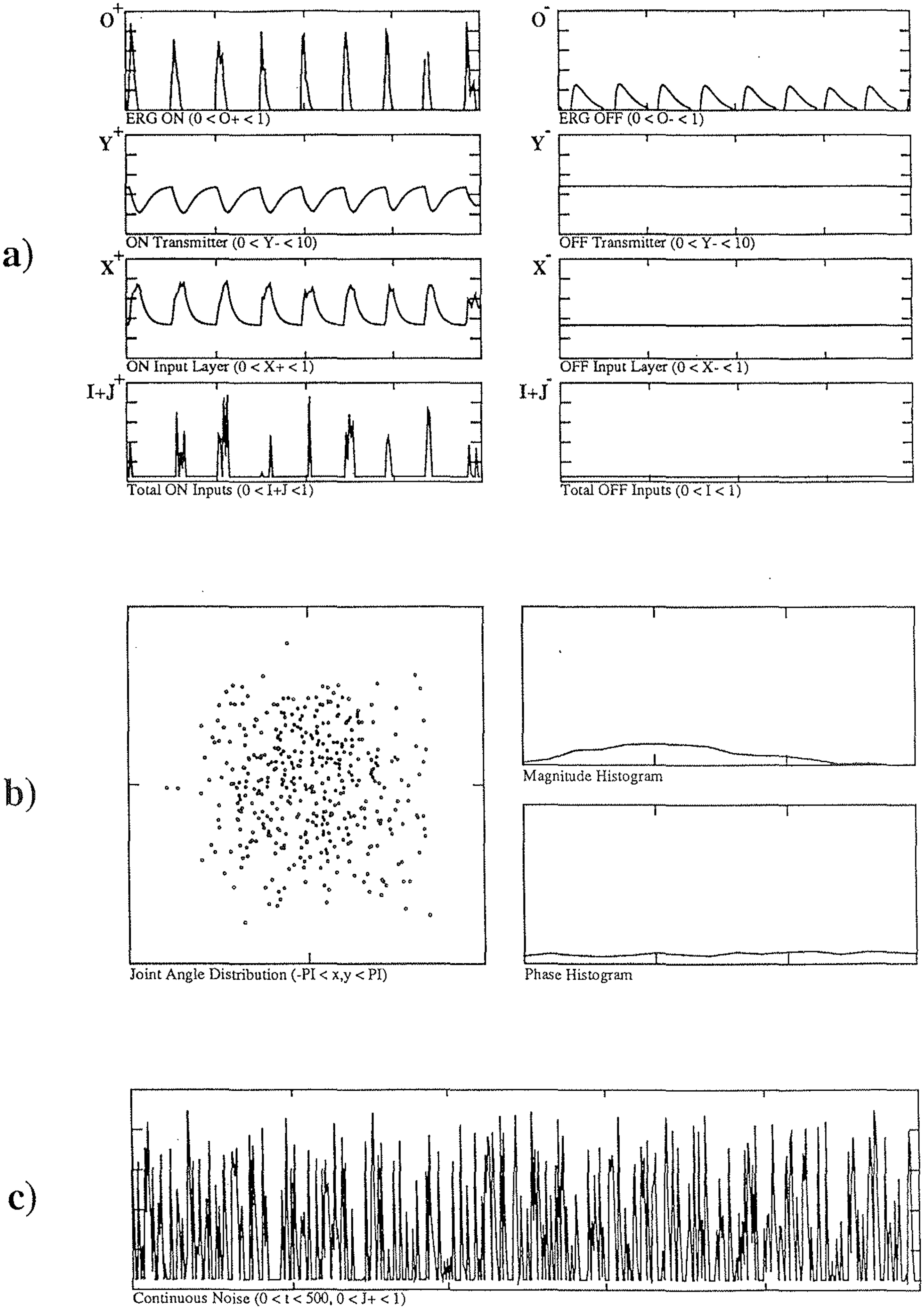
a)
O^+
ERG ON (0 < O+ < 1)
O^-
ERG OFF (0 < O- < 1)
Y^+
ON Transmitter (0 < Y- < 10)
Y^-
OFF Transmitter (0 < Y- < 10)
X^+
ON Input Layer (0 < X+ < 1)
X^-
OFF Input Layer (0 < X- < 1)
$I+J^+$
Total ON Inputs (0 < I+J <1)
$I+J^-$
Total OFF Inputs (0 < I < 1)
b)
Joint Angle Distribution (-PI < x,y < PI)
Magnitude Histogram
Phase Histogram
c)
Continuous Noise (0 < t < 500, 0 < J+ < 1)

Figure 13

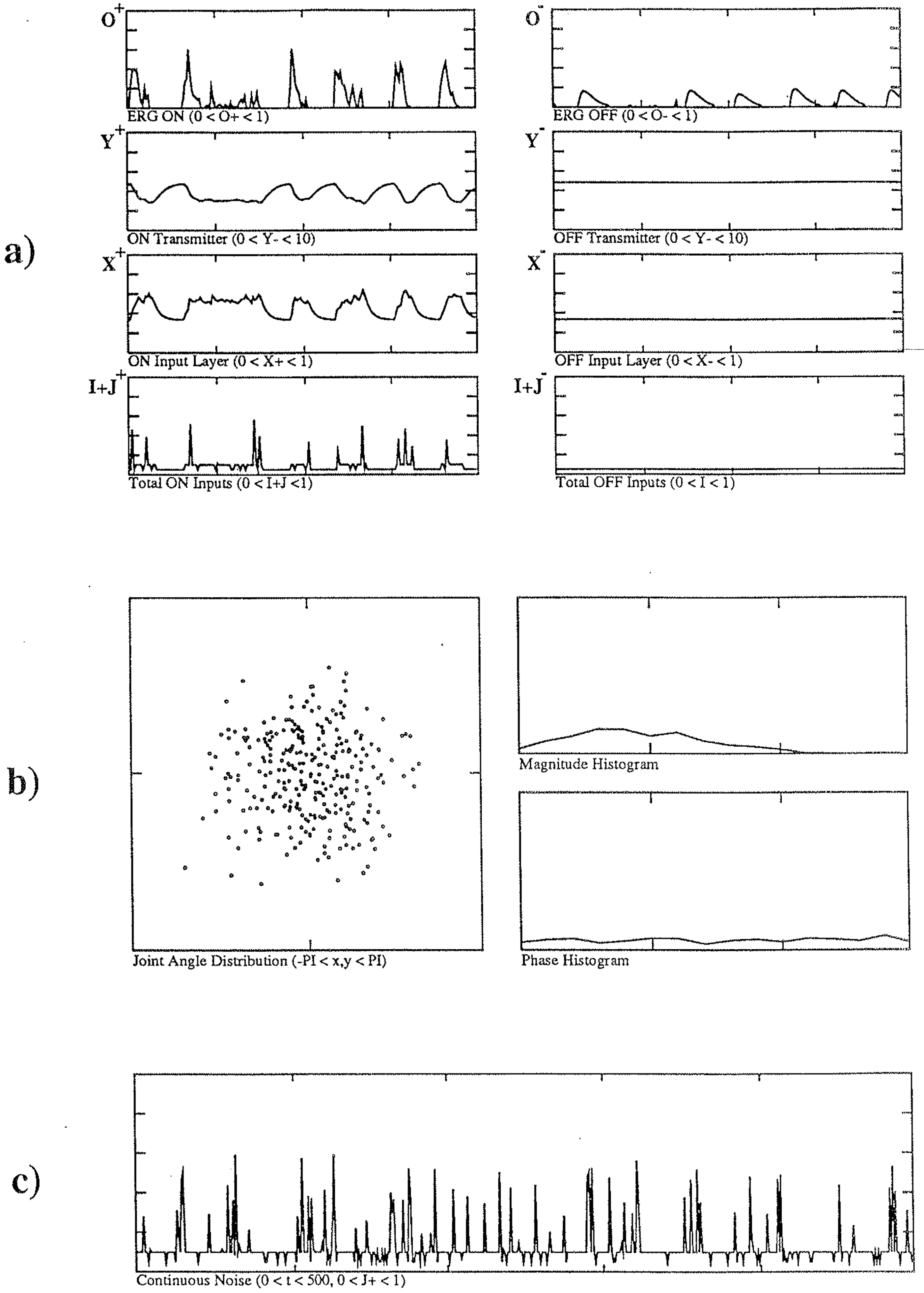
a)
O+
ERG ON (0 < O+ < 1)
O-
ERG OFF (0 < O- < 1)
Y+
ON Transmitter (0 < Y- < 10)
Y-
OFF Transmitter (0 < Y- < 10)
X+
ON Input Layer (0 < X+ < 1)
X-
OFF Input Layer (0 < X- < 1)
I+J+
Total ON Inputs (0 < I+J <1)
I+J-
Total OFF Inputs (0 < I < 1)
b)
Joint Angle Distribution (-PI < x,y < PI)
Magnitude Histogram
Phase Histogram
c)
Continuous Noise (0 < t < 500, 0 < J+ < 1)

Figure 14

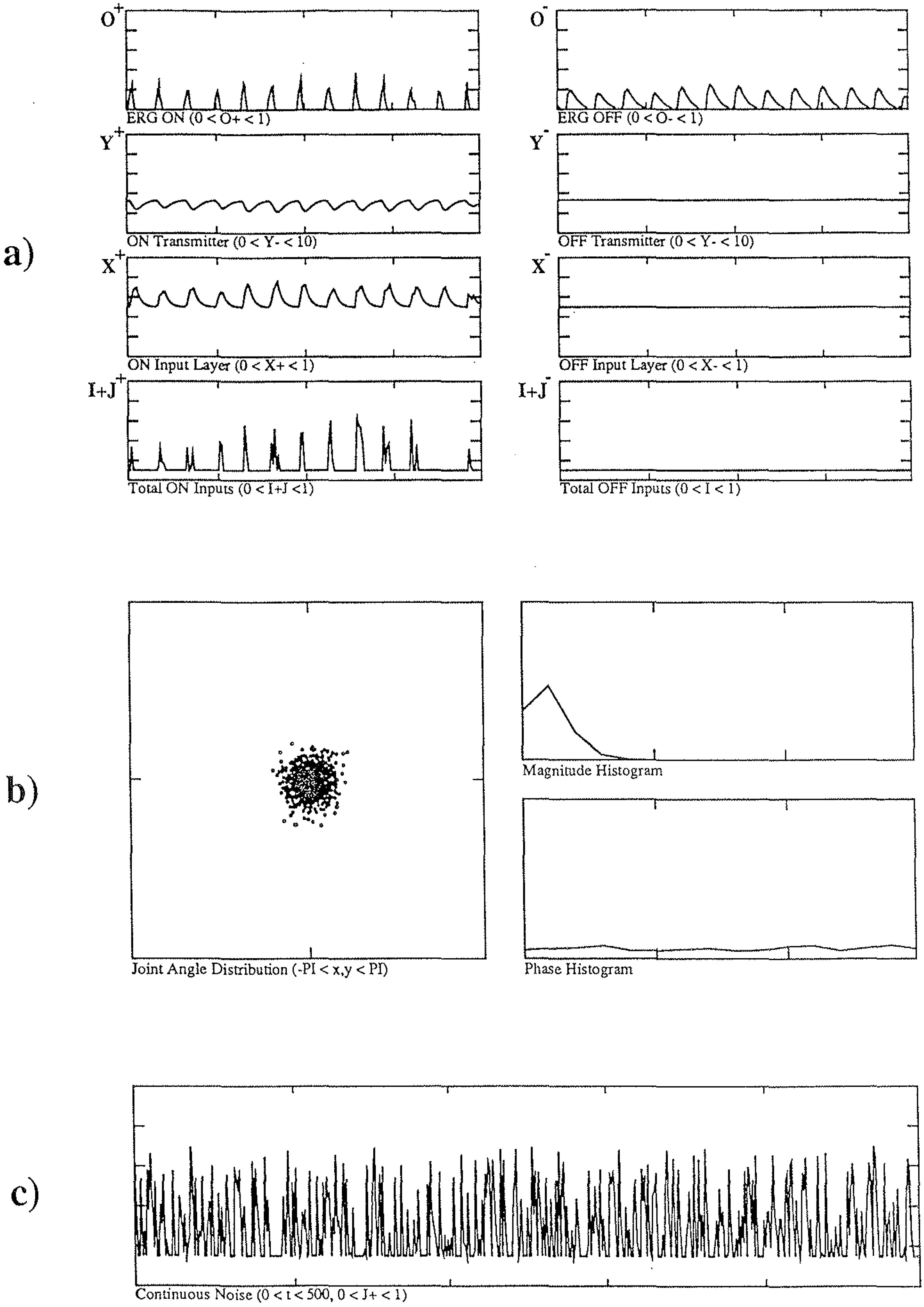
a)
O^+
ERG ON (0 < O+ < 1)
O^-
ERG OFF (0 < O- < 1)
Y^+
ON Transmitter (0 < Y- < 10)
Y^-
OFF Transmitter (0 < Y- < 10)
X^+
ON Input Layer (0 < X+ < 1)
X^-
OFF Input Layer (0 < X- < 1)
$I+J^+$
Total ON Inputs (0 < I+J <1)
$I+J^-$
Total OFF Inputs (0 < I < 1)
b)
Joint Angle Distribution (-PI < x,y < PI)
Magnitude Histogram
Phase Histogram
c)
Continuous Noise (0 < t < 500, 0 < J+ < 1)

Figure 15

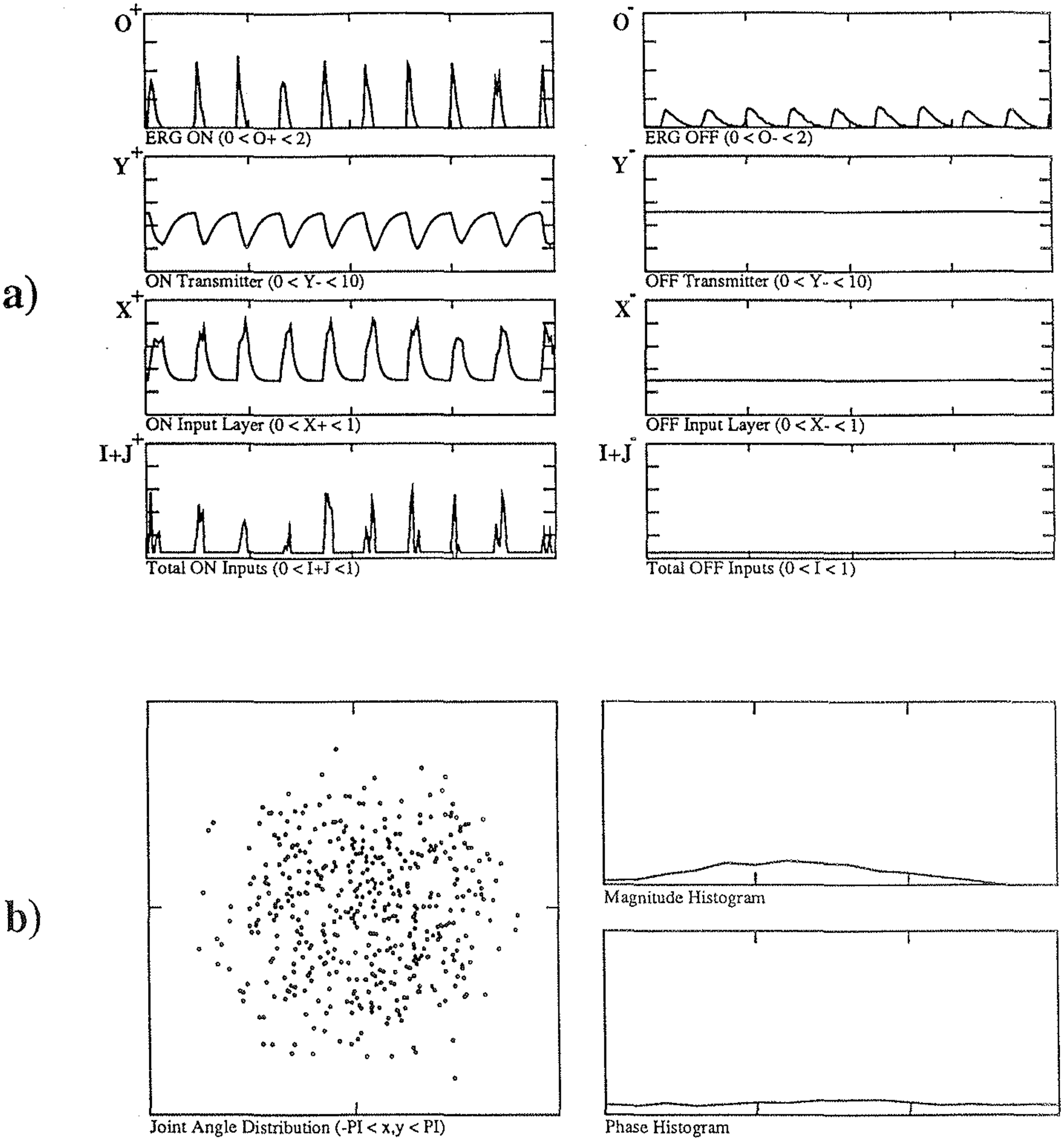
a)
O^+
ERG ON (0 < O+ < 2)
O^-
ERG OFF (0 < O- < 2)
Y^+
ON Transmitter (0 < Y- < 10)
Y^-
OFF Transmitter (0 < Y- < 10)
X^+
ON Input Layer (0 < X+ < 1)
X^-
OFF Input Layer (0 < X- < 1)
$I+J^+$
Total ON Inputs (0 < I+J <1)
$I+J^-$
Total OFF Inputs (0 < I < 1)
b)
Joint Angle Distribution (-PI < x,y < PI)
Magnitude Histogram
Phase Histogram

Figure 16

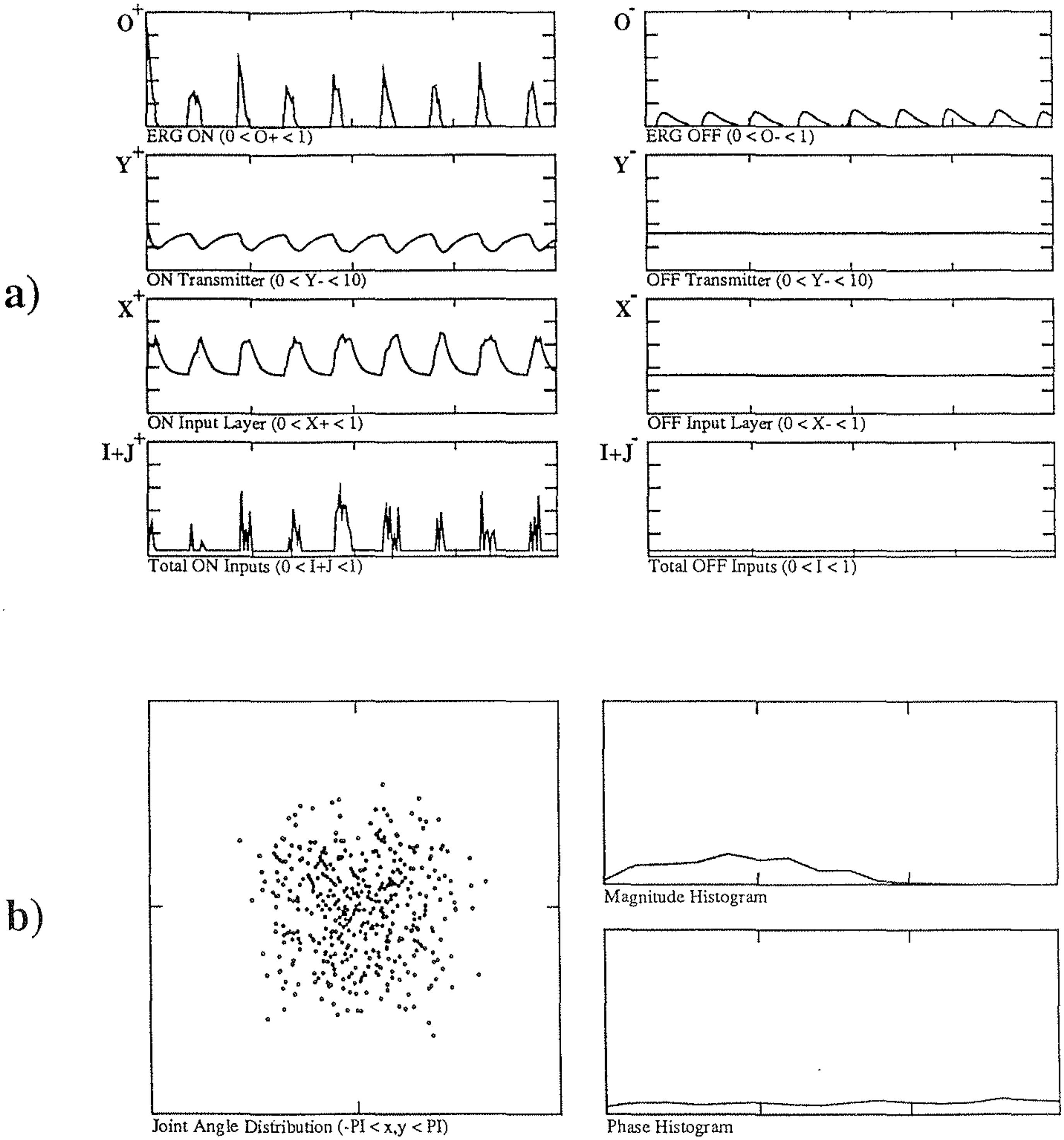
a)
O^+
ERG ON (0 < O+ < 1)
O^-
ERG OFF (0 < O- < 1)
Y^+
ON Transmitter (0 < Y- < 10)
Y^-
OFF Transmitter (0 < Y- < 10)
X^+
ON Input Layer (0 < X+ < 1)
X^-
OFF Input Layer (0 < X- < 1)
$I+J^+$
Total ON Inputs (0 < I+J <1)
$I+J^-$
Total OFF Inputs (0 < I < 1)
b)
Joint Angle Distribution (-PI < x,y < PI)
Magnitude Histogram
Phase Histogram

Figure 17

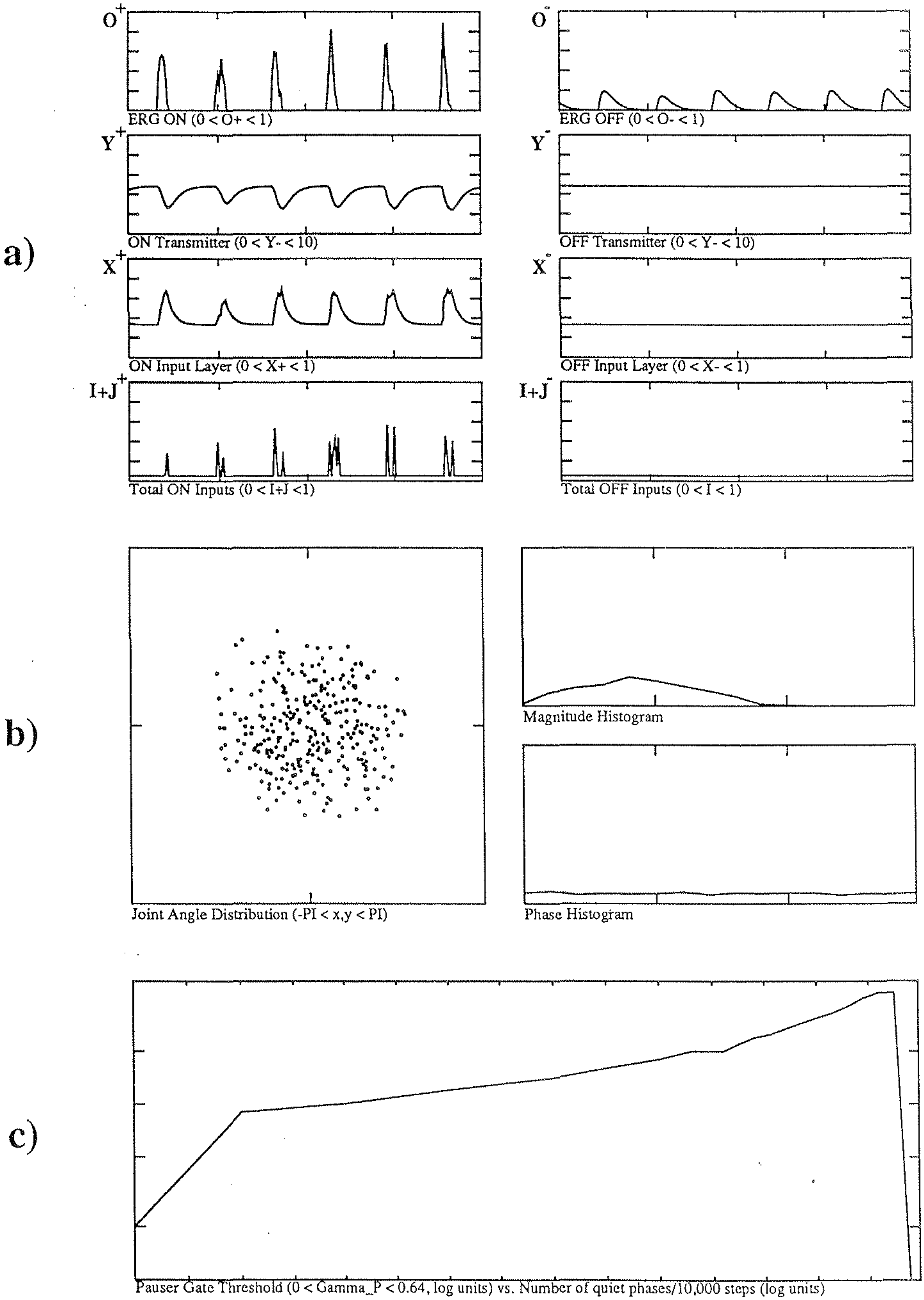
a)
O^+
ERG ON (0 < O+ < 1)
O^-
ERG OFF (0 < O- < 1)
Y^+
ON Transmitter (0 < Y- < 10)
Y^-
OFF Transmitter (0 < Y- < 10)
X^+
ON Input Layer (0 < X+ < 1)
X^-
OFF Input Layer (0 < X- < 1)
$I+J^+$
Total ON Inputs (0 < I+J <1)
$I+J^-$
Total OFF Inputs (0 < I < 1)
b)
Joint Angle Distribution (-PI < x,y < PI)
Magnitude Histogram
Phase Histogram
c)
Pauser Gate Threshold (0 < Gamma_P < 0.64, log units) vs. Number of quiet phases/10,000 steps (log units)

Figure 18

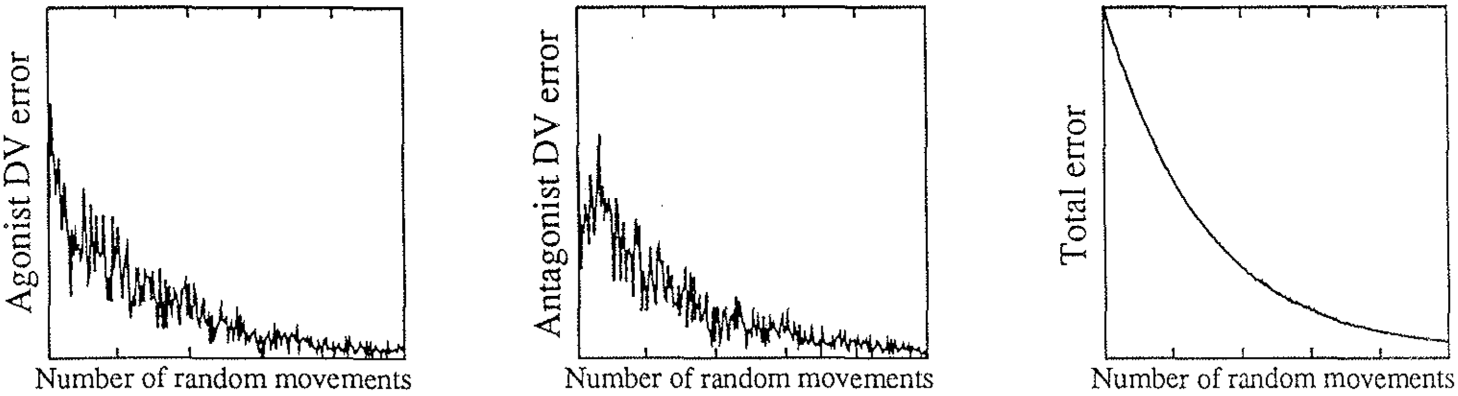
Agonist DV error
Number of random movements
Antagonist DV error
Number of random movements
Total error
Number of random movements

Figure 19

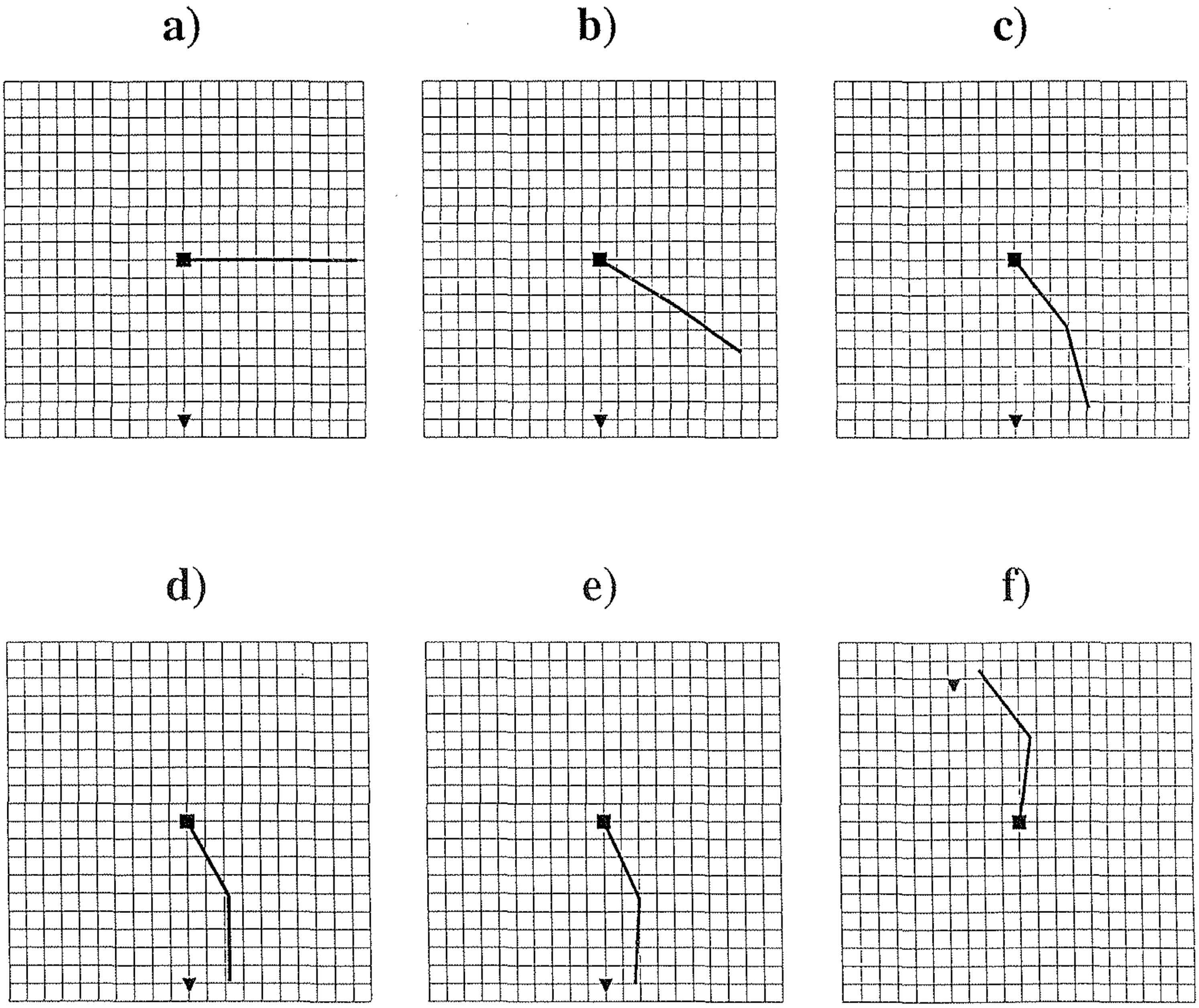

Figure 20

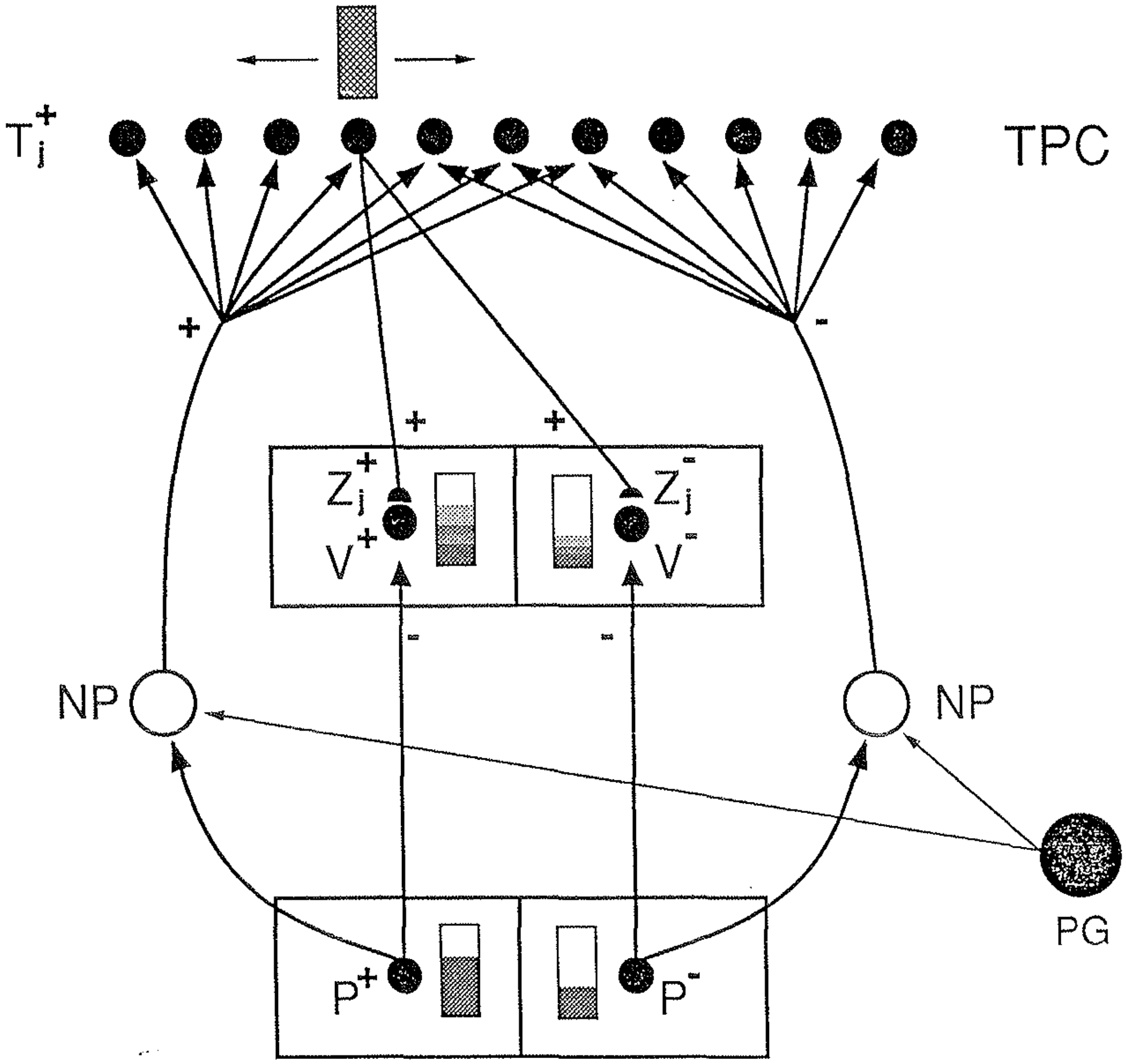

Figure 21

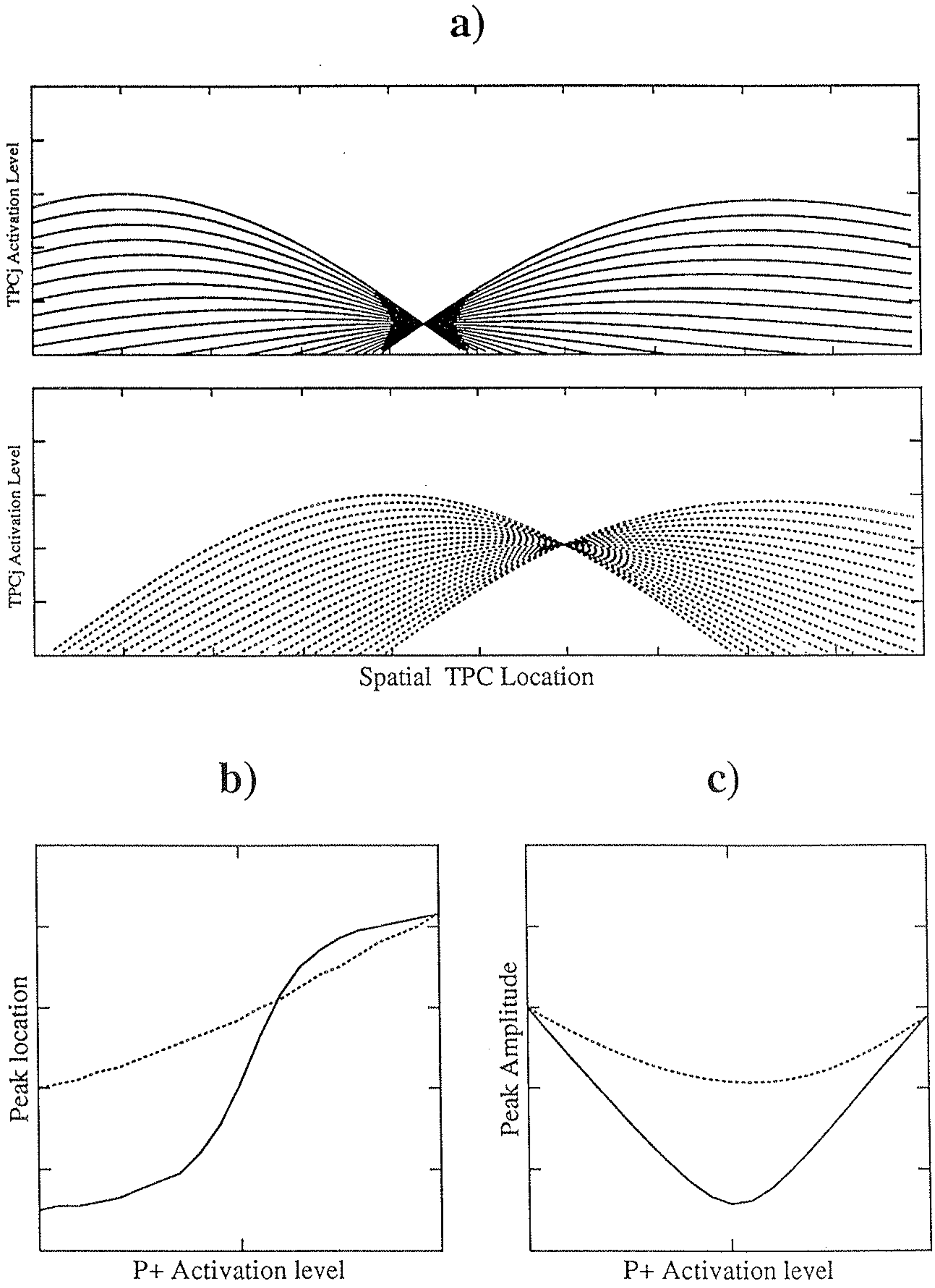
a)
TPCj Activation Level
TPCj Activation Level
Spatial TPC Location
b)
c)
Peak location
P+ Activation level
Peak Amplitude
P+ Activation level

Figure 22

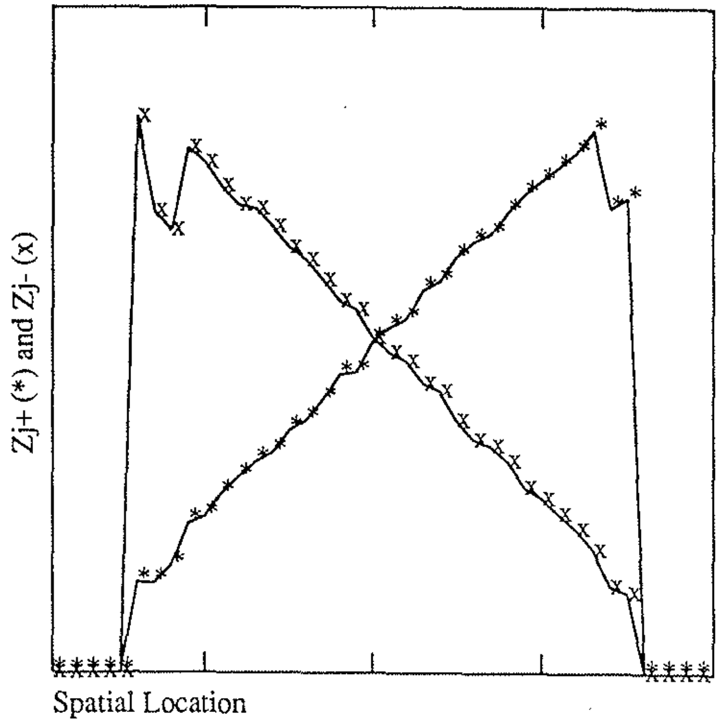

Figure 23

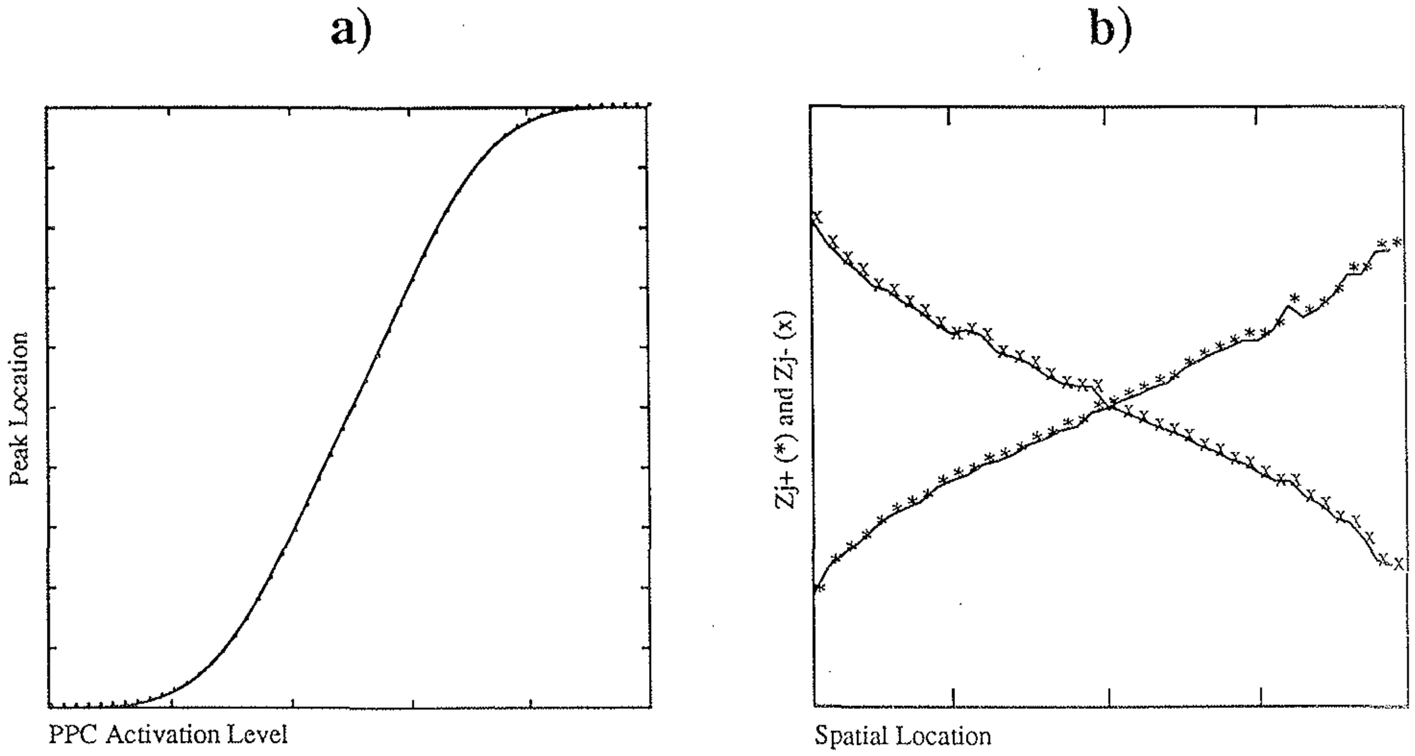
a)
Peak Location
PPC Activation Level
b)
Zj+ (*) and Zj- (x)
Spatial Location

Figure 24

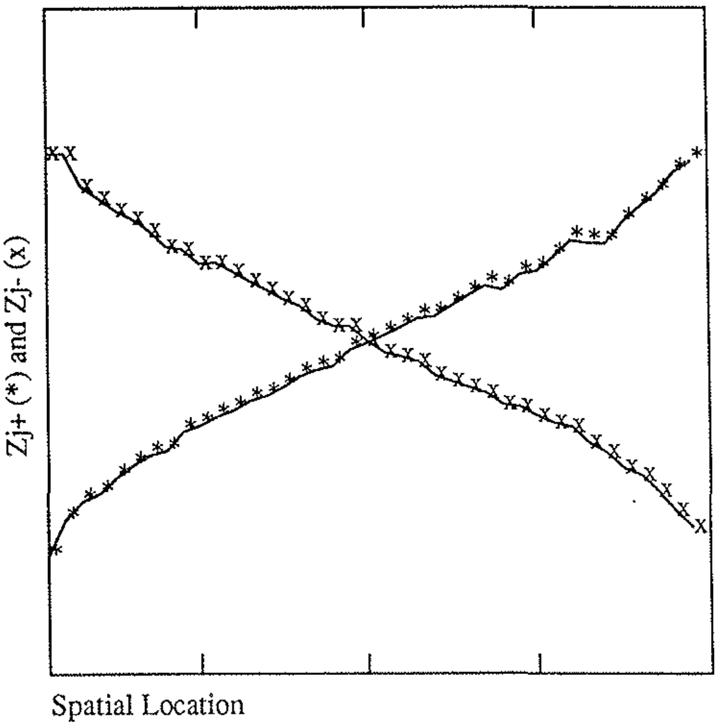

Figure 25

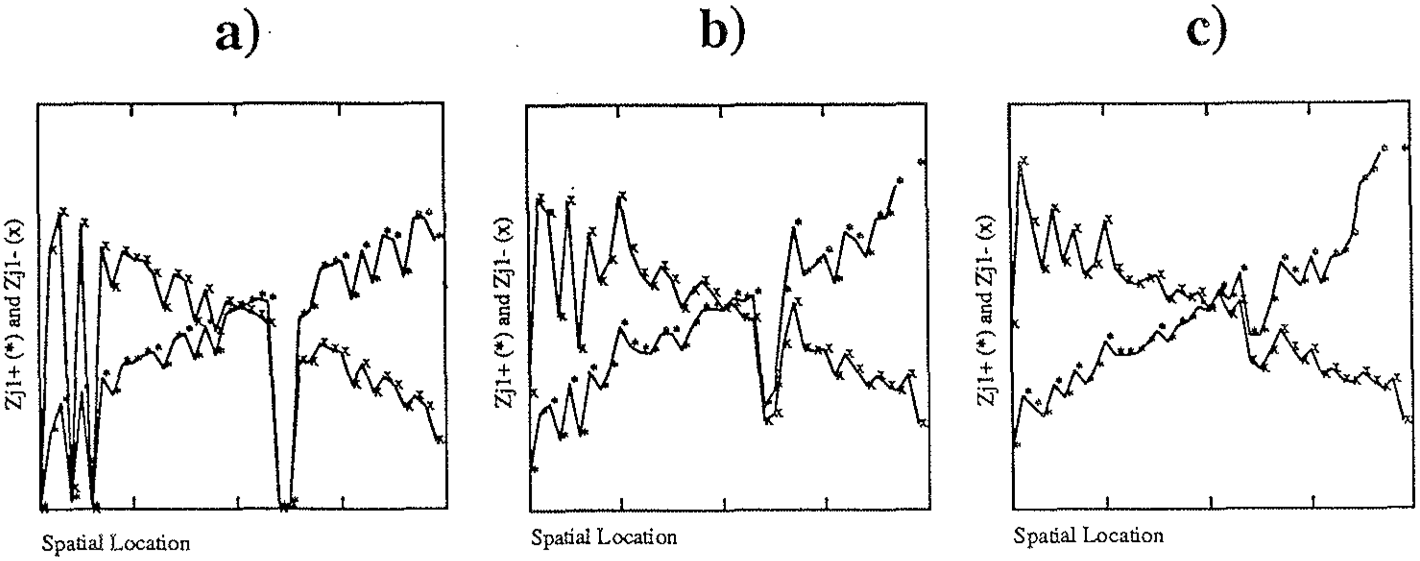
a)
b)
c)
Zj1+ (*) and Zj1- (x)
Zj1+ (*) and Zj1- (x)
Zj1+ (*) and Zj1- (x)
Spatial Location
Spatial Location
Spatial Location

Figure 26

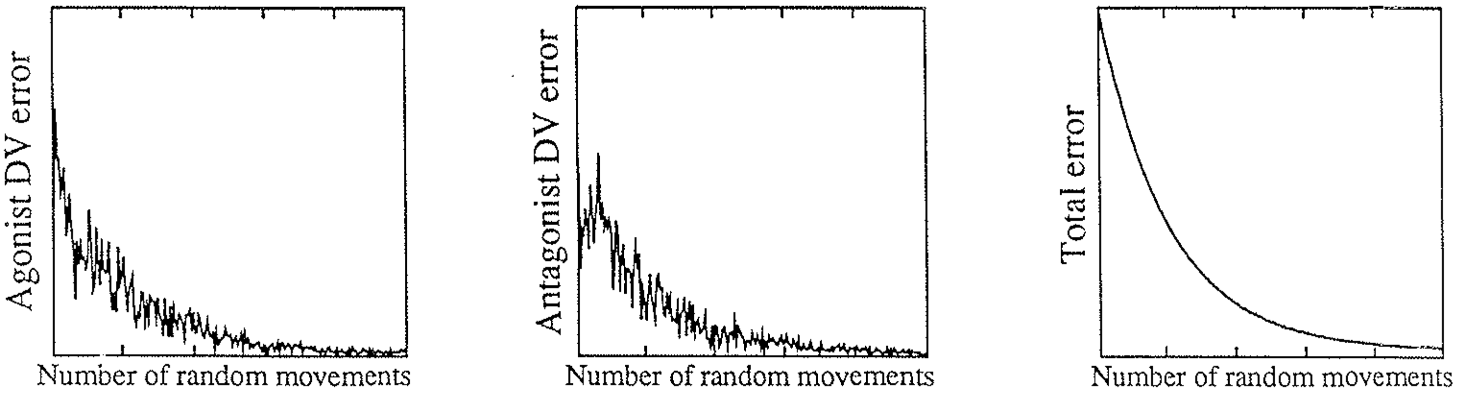
Agonist DV error
Number of random movements
Antagonist DV error
Number of random movements
Total error
Number of random movements

Figure 27

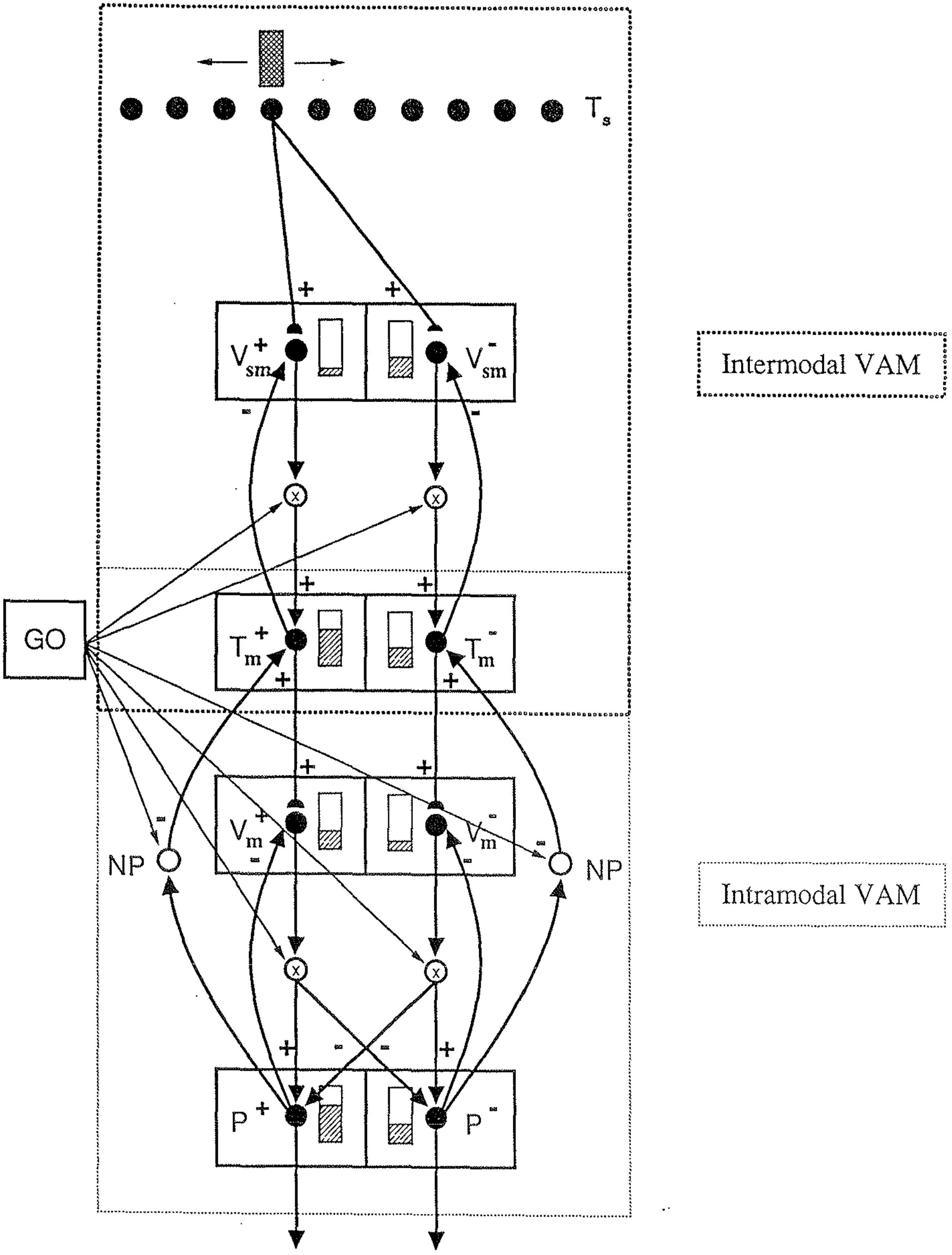

T_s
+
+
V_{sm}^+
V_{sm}^-
-
-
Intermodal VAM
x
x
GO
+
+
T_m^+
T_m^-
+
+
+
+
V_m^+
V_m^-
-
-
-
-
NP
NP
Intramodal VAM
x
x
+
-
-
+
P^+
P^-

Figure 28

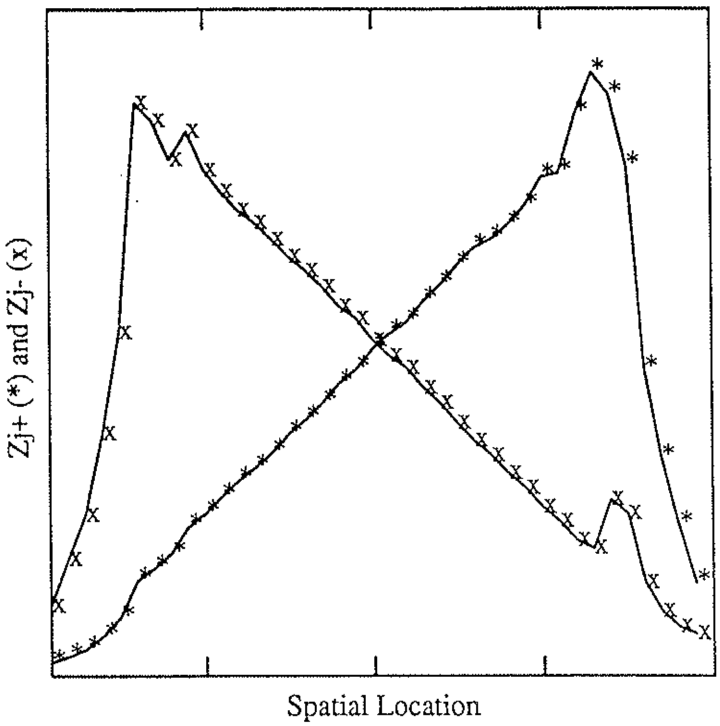

Figure 29

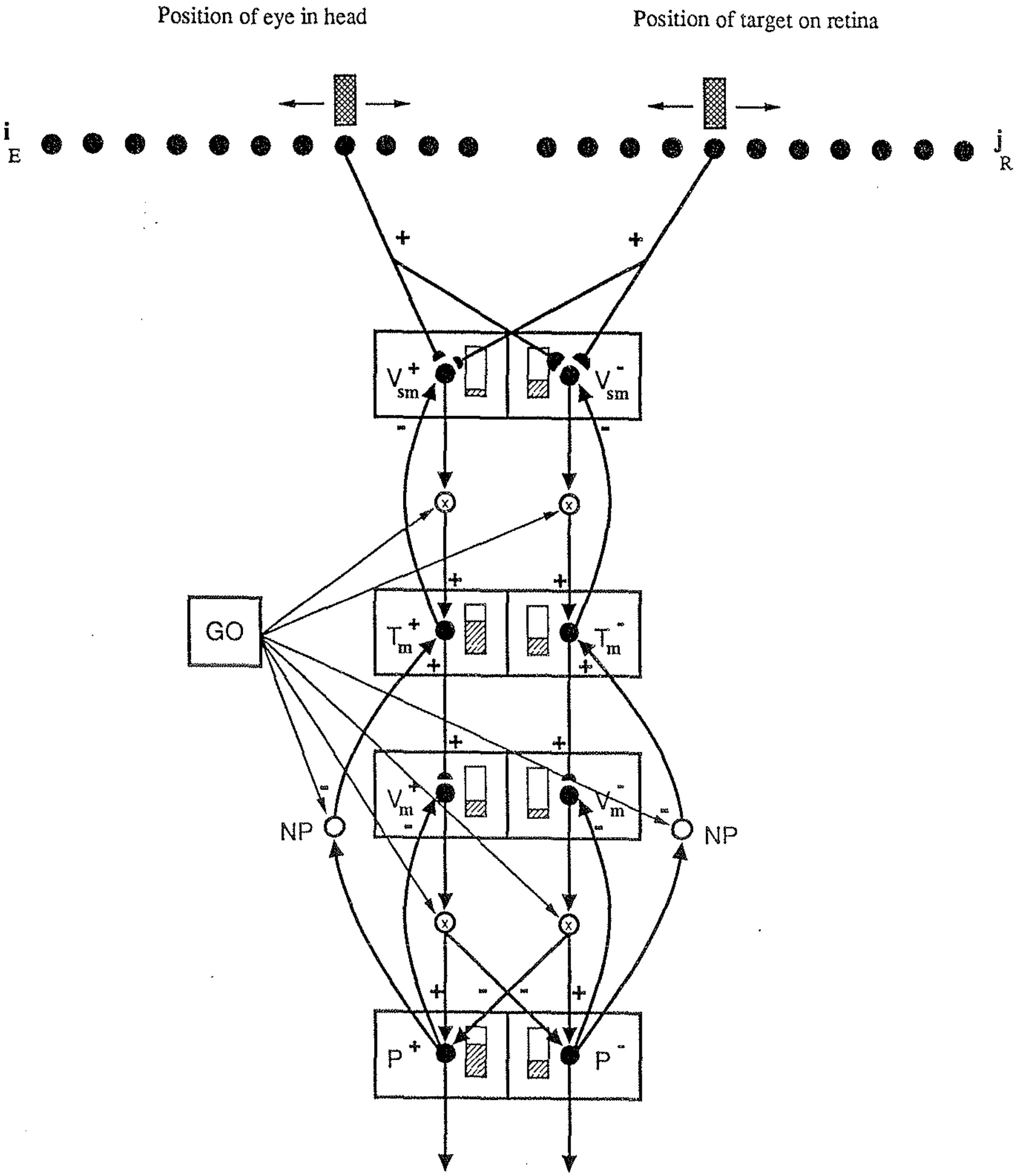
Position of eye in head
Position of target on retina
i_E
j_R
+
+
V_{sm}^+
V_{sm}^-
-
-
GO
+
+
T_m^+
T_m^-
+
+
+
+
V_m^+
V_m^-
NP
NP
-
-
+
-
-
+
P^+
P^-

Figure 30

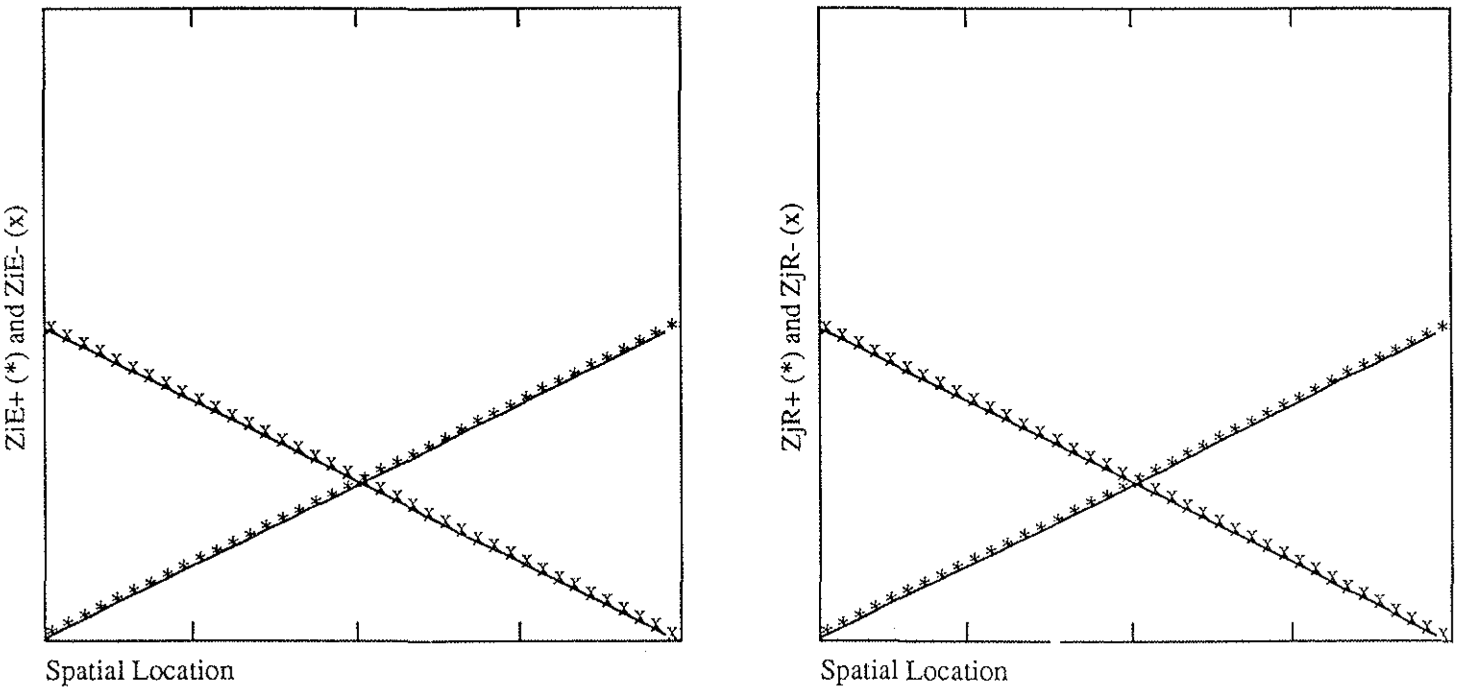
ZiE+ (*) and ZiE- (x)
Spatial Location
ZjR+ (*) and ZjR- (x)
Spatial Location

Figure 31